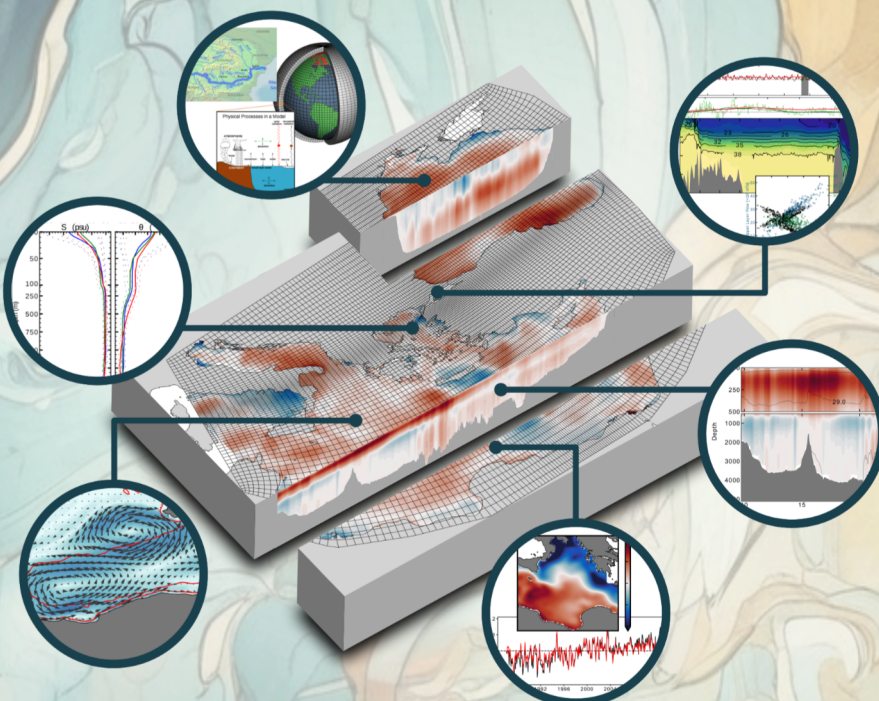




Stamatos Petalas

# Development of a Hydrodynamic Simulation for the Study of Climate Change and Variability in the Aegean Sea

Doctoral Dissertation





DEVELOPMENT OF A HYDRODYNAMIC  
SIMULATION FOR THE STUDY OF  
CLIMATE CHANGE AND VARIABILITY IN  
THE AEGEAN SEA

Stamatis Petalas



*A dissertation submitted in partial fulfillment  
of the requirements for the degree of  
Doctor of Philosophy*

*to the*

Department of Marine Sciences  
School of Environment



University of the Aegean  
Mytilene, Greece

February 2023



Copyright © 2023 Stamatos Petalas  
This work is licensed under a [CC BY 4.0 license](#).

This is the final version of the document, after the inclusion of corrections and suggestions made by the examination committee.

**Cite as:**

Petalas, S., (2023). *"Development of a Hydrodynamic Simulation for the study of Climate Change and Variability in the Aegean Sea "*. Doctoral dissertation, University of the Aegean, Mytilene. <https://dx.doi.org/10.12681/eadd/54808>

## ADVISORY COMMITTEE

---

### SUPERVISOR:

**Elina Tragou**

*Associate Professor, University of the Aegean, Mytilene*

### MEMBERS:

**Vassilis Zervakis**

*Professor, University of the Aegean, Mytilene*

**Elena Xoplaki**

*Associate Professor, Justus-Liebig University, Giessen*

## EXAMINATION COMMITTEE

---

**Elina Tragou**

*Associate Professor, University of the Aegean, Mytilene*

**Vassilis Zervakis**

*Professor, University of the Aegean, Mytilene*

**Elena Xoplaki**

*Associate Professor, Justus-Liebig University, Giessen*

**Adonis Velegrakis**

*Professor, University of the Aegean, Mytilene*

**Evangelia Krasakopoulou**

*Professor, University of the Aegean, Mytilene*

**Georgios Sylaios**

*Professor, Democritus University of Thrace, Xanthi*

**Dimitrios Velaoras**

*Principal Researcher, Hellenic Center for Marine Research, Athens*



στην *Μαρίλια*  
στον *Γιάννο*  
και στην *Σταυρούλα*

για την έμπνευση, τις αγκαλιές,  
και την μαγευτική μουσική  
σε ένα ταξίδι που συνεχίζεται . . .



## DECLARATION

---

I declare that this thesis has been composed by myself and that it has not been submitted, in whole or in part, in any previous application for a degree. Except where stated otherwise by reference or acknowledgment, the work presented is entirely my own.

Parts of this work have been published or are currently under publication in cooperation with other contributing authors, as can be found in some of the entries of the section "Publications".

*Mytilene, February 2023*

---

Stamatis Petalas



# PUBLICATIONS

---

Following is a list of all publications that have either been published during the course of this PhD research, or are currently under the preparation/submission process:

## IN JOURNALS:

1. **Petalas, S.**; Tragou, E.; Mamoutos, G.I.; Zervakis, V. "Simulating the Interconnected Eastern Mediterranean - Black Sea System on Climatic Timescales: A 30-year realistic hindcast". *J. Mar. Sci. Eng.* 2022, 10, 1786. <https://doi.org/10.3390/jmse10111786>
2. Bourma, E.; Perivoliotis, L.; Petihakis, G.; Korres, G.; Frangoulis, C.; Ballas, D.; Zervakis, V.; Tragou, E.; Katsafados, P.; Spyrou, C.; [... **Petalas, S.**; ...] et al. "The Hellenic Marine Observing, Forecasting and Technology System - An Integrated Infrastructure for Marine Research". *J. Mar. Sci. Eng.* 2022, 10, 329. <https://doi.org/10.3390/jmse10030329>
3. Mamoutos, I.G.; Potiris, E.; Tragou, E.; Zervakis, V.; **Petalas, S.** "A High-Resolution Numerical Model of the North Aegean Sea Aimed at Climatological Studies". *J. Mar. Sci. Eng.* 2021, 9, 1463. <https://doi.org/10.3390/jmse9121463>
4. **Petalas, S.**, Mamoutos, I., Dimitrakopoulos, A.-A., Sampatakaki, A., and Zervakis, V., 2020. "Developing a Pilot Operational Oceanography System for an Enclosed Basin", *J. Mar. Sci. Eng.* 2020, 8, 336. <http://dx.doi.org/10.3390/jmse8050336>
5. **Petalas, S.**; Luther, N.; Behr, L.; Xoplaki, E.; Tragou, E.; Gogou, A.; Zervakis, V.; et al. "Atmosphere-Ocean Concurrent Heatwave Events and Interactions in the Eastern Mediterranean Sea". [In preparation]
6. Behr, L.; Luther, N.; **Petalas, S.**; Xoplaki, E.; Tragou, E.; Gogou, A.; Zervakis, V.; et al. "Linking Atmospheric and Marine Heatwaves: A First Definition of Co-occurring Atmospheric and Marine Heatwaves". [In preparation]
7. **Petalas, S.**; Tragou, E.; Zervakis, V.; et al. "On the role of Black Sea Waters in controlling the North Aegean buoyancy fluxes". [In preparation]

## IN BOOKS:

1. Tragou, E., **Petalas, S.**, Mamoutos, I., 2022. "Air sea interaction - Heat and fresh water fluxes in the Aegean Sea". In: The Handbook of Environmental Chemistry. Springer, Berlin, Heidelberg. [https://doi.org/10.1007/698\\_2021\\_841](https://doi.org/10.1007/698_2021_841)

## IN CONFERENCES:

1. Mazioti, A.A., Kolovoyiannis, V., **Petalas, S.**, Mamoutos, I., Potiris, E., Krasakopoulou, E., Tragou, E., Zervakis, V.: "Simulating The Fate Of Selected PAHs In Saronikos Gulf, Eastern Mediterranean, Using A Far Field Water-Quality Model", Proceedings of 18th International Conference on Environmental Science and Technology (CEST), Athens, Greece, 30 August - 2 September 2023, pp 218. <https://cest.gnest.org/e/cest-2023>
2. **Petalas, S.**, Tragou, E., Mamoutos, I., and Zervakis, V. "On the role of black sea waters in controlling the north aegean buoyancy fluxes" EGU General Assembly 2023, EGU23-15973, Vienna, Austria. <https://doi.org/10.5194/egusphere-egu23-15973>
3. Kolovoyiannis, V., Mazioti, A. A., Krasakopoulou, E., Zervakis, V., Tragou, E. A., Mamoutos, I., Potiris, E., **Petalas, S.**, Chatzilaou, C., Mosiou, K., Kontoyiannis, H., Paraskevopoulou, V., and Athinotis, A., "Implementation of a modelling system for the investigation of the Saronikos Gulf marine ecosystem (Eastern mediterranean)" EGU General Assembly 2023, EGU23-12514, Vienna, Austria. <https://doi.org/10.5194/egusphere-egu23-12514>
4. Zervakis, V., Krasakopoulou, E., Tragou, E., Kolovoyiannis, V., Mamoutos, I., Potiris, M., Androulidakis, I., Mosiou, K., Kalatzi, M. I., Mazioti, A. A., Chatzilaou, C., Kougioumtzoglou, R. F., and **Petalas, S.** "Development of a coastal oceanographic observatory for the north aegean sea: The AEGIS projects". EGU General Assembly 2023, EGU23-13065, Vienna, Austria. <https://doi.org/10.5194/egusphere-egu23-13065>
5. Behr, L., Luther, N., Xoplaki, E., **Petalas, S.**, Tragou, E., and Zervakis, V. "A global approach to defining concurrent atmospheric and marine heatwaves" EGU General Assembly 2023, EGU23-6094, Vienna, Austria. <https://doi.org/10.5194/egusphere-egu23-6094>
6. Zervakis, V., Krasakopoulou, E., Tragou, E., Mamoutos, I., Potiris, E., **Petalas, S.**, Kolovoyiannis, V., Dimitrakopoulos, A., Sampatakaki, A. and Tsabarlis Ch., "AEGIS - A pilot coastal observatory for semi-enclosed basins", Proceedings of Marine and Inland Waters Research Symposium, Porto Heli, Argolida, Greece, 16-19 September 2022, pp 37-41. [https://symposia.gr/wp-content/uploads/2022/10/Proceedings\\_5.10.22.pdf](https://symposia.gr/wp-content/uploads/2022/10/Proceedings_5.10.22.pdf)
7. Zervakis, V., Ntziachristos, L., Moustaka, M., Gondikas, A., Kukkonen, J., Genitsaris, S., Barmpas, F., Chatzilaou, Ch., Kalatzi, I., Kolovoyiannis, V., Kourkoutmani, P., Krasakopoulou, E., Kougioumtzoglou, F., Mamoutos, I., Mazioti, A., **Petalas, S.**, Potiris, E., Stefanidou, N., Tragou, E., Tsegas, G. and Vagi, M., "Assessing the marine scrubbers' impact on the Saronikos Gulf marine ecosystem through the project EMERGE", Proceedings of Marine and Inland Waters Research Symposium, Porto Heli, Argolida, Greece, 16-19 September 2022, pp 693-700. [https://symposia.gr/wp-content/uploads/2022/10/Proceedings\\_5.10.22.pdf](https://symposia.gr/wp-content/uploads/2022/10/Proceedings_5.10.22.pdf)
8. Xoplaki, E., Tragou, E., Gogou, A., Zervakis, V., Koutsoubas, D., Behr, L., **Petalas, S.**, and Sini, M. "EM-MHeatWaves: Eastern Mediterranean marine heatwaves - Ocean responses to atmospheric forcing and impacts on marine ecosystems", EGU General Assembly 2021, 19-30 Apr 2021, EGU21-9907, 2021. <https://doi.org/10.5194/egusphere-egu21-9907>

9. Behr, L., **Petalas, S.**, Jaeger, M., Xoplaki, E., Tragou, E., Gogou, A., and Zervakis, V.: "Atmosphere-Ocean compound heat wave events in the Eastern Mediterranean" (Oral), EGU General Assembly 2021, online, 19–30 Apr 2021, EGU21-9583, 2021. <https://doi.org/10.5194/egusphere-egu21-9583>
10. **Petalas, S.**, Dimitrakopoulos, A.A., Mamoutos, I., Sampatakaki, A., Zervakis, V., "Prototype Oceanographic Monitoring System development for the Kalloni Bay, Lesvos, Greece" (Oral), in proceedings of CHEERS 2019, Global Changes In Estuarine and Coastal Systems Functioning: Innovative Approaches and Assessment Tools, Bordeaux, France. <https://cheers2019.sciencesconf.org/resource/page/id/3.html>
11. **Petalas, S.**, Mamoutos, I., Tragou E., Zervakis, V., "A 30-year hindcast of the interconnected Eastern Mediterranean - Black Sea system: A first step towards climate projections for the Aegean Sea" (Oral), EGU General Assembly 2019, EGU2019-13821, Vienna, Austria. <https://meetingorganizer.copernicus.org/EGU2019/EGU2019-13821.pdf>
12. Mamoutos, I., **Petalas, S.**, Sampatakaki, A., Dimitrakopoulos, A.A., Zervakis, V., 2018. "A high resolution hydrodynamic simulation of Lesvos semi-enclosed embayment Kalloni Gulf: Preliminary results", 3rd Hydromedit Conference, Volos, Greece.
13. **Petalas, S.**, Tragou, E., Zervakis, V., 2016. "Evaluation of future Black Sea river inflow using hydrological model data and Artificial Neural Networks", in proceedings of MedClivar 2016 conference (Poster), University of Athens, Athens, Greece.



*"I can't think like you, you can't think like me,  
but if we can't meet each other in the middle,  
what's the point of playing hide and seek? "*

— Million Hollers *Explanation Below*

## ACKNOWLEDGMENTS

---

The journey of carrying out a doctoral dissertation is usually long, rough and undulating with tedious uphill sections and brief downhills. Nevertheless, overcoming these difficulties makes the journey worthwhile, and the relations you form with people that help you along the way, make it a very rewarding process which expands your horizons and propels you forward. The closest of these people are usually found in the immediate work environment and constitute members of the broader academic family.

Starting there, I express my gratitude to the members of my advisory committee, namely, my supervisor *Elina Tragou*, for her patience and guidance throughout this research work, and for the academic opportunities she created for me; my co-supervisor *Vassilis Zervakis* for his guidance, his constant fundraising efforts to support my research and the numerous opportunities he gave me to leave my computer and gain valuable experience in the field; and my co-supervisor *Elena Xoplaki* for her guidance, enthusiasm and the opportunity she gave me to work in such an inspiring environment alongside her radiant team at the University of Giessen.

Additionally, I express my gratitude to the members of the examining committee *Evangelia Krasakopoulou*, *Adonis Velegrakis*, *Georgios Sylaios* and *Dimitrios Velaoras* for their comments, corrections and valuable suggestions on improving the original manuscript, as well as on the insightful discussions they initiated during the defense process.

I express my heartfelt appreciation to my colleagues in the Laboratory of Physical and Chemical Oceanography, and dear friends *Giannis Mamoutos*, *Alexandros Dimitrakopoulos*, *Dimitra Marmara*, *Aggeliki Sampatakaki*, *Manos Potiris*, and *Vassilis Kolovoyiannis*, for their help with research-related, code-related, administration-related as well as life-related subjects. Their assistance made this work possible, and their sparkling company and witty discussions either in the laboratory (a.k.a. "the cave"), a local bar, or in one of our numerous field campaigns, made the whole endeavor joyful and wholesome.

As part of the IKYDA bilateral agreement program for academic exchange, I had the fortune to collaborate with my colleagues from the University of Giessen *Lorine Behr*, *Niklas Luther*, *Mingyue Zhang* and *Eva Hartmann*. Our lengthy discussions, brainstorming sessions and data crunching/analysis assemblies, expanded my knowledge and technical skills, taught me to think outside the box, and helped me grow further by experiencing a high level of academic cooperation, which eventually fostered the chapter on marine heatwaves. I thank them all for their kindness, help and friendship.

My longtime friend and colleague throughout our academic journeys *Stratos Bourtsoukidis*, played a special role in this dissertation. Although our scientific interests diverged slightly, we could still find common ground to talk about each-other's work. Our exciting discussions when we met (either in an EGU conference in Vienna, a park in Frankfurt or the waterfront in Thessaloniki) triggered the formulation of new approaches, some of which materialized in this dissertation. I thank him for his friendship, suggestions and help in this ongoing journey.

I heartily thank my brother *Apostolos* who has always been the go-to person whenever I wanted to share something about my work, either new and exciting or dull and monotonous. His brilliant and unique approach to problem solving, paired with his proficiency in numerical methods, helped me in a multitude of ways throughout my research. The contribution of my parents *Giannis* and *Maria* has been constant and invaluable on many levels since the very start of my studies. I can only offer them my love and deep appreciation, for all their efforts to support me throughout these years.

During the time I spent on the beautiful and welcoming island of Lesvos, I was fortunate to enjoy the company and help of many people, some of which were good friends from the past and some of which became good friends in the process. Starting with my arrival at the island, the "three graces" *Gogo Dimopoulou*, *Despoina Stamatakis* and *Anastasia Anagnostopoulou* apart from allowing me to stay in a room of their house for the first period, they introduced me to the pluralistic island life and their immediate social cycle, and in general made me feel at home. The entire doctoral experience would have been greatly reduced if it wasn't for them. In addition, throughout my stay in Mytilene and work at the University of the Aegean, a large group of friends helped me out in a million different ways, by giving me either a good suggestion, a dreamy getaway, philosophical nutrition, the means to unwind through music, a place to stay during a travel, or simply a helping hand with everyday issues. I am grateful to all of them and consider them members of this effort: *Thodoris Aggelelis*, *Kostas Rossos*, *Chris Corbett*, *Karina Mpratou*, *Titos Mpratou*, *Fanis Mpoumpouloudis*, *Lenio Vounisiou*, *Giorgos Evangelopoulos*, *Antreas Sotiriadis*, *Maria Papadopoulou*, *Dafni Montesantou*, *Aristea Vogri*, *Grigoris Efstatiou*, *Haris Sarafidis*, *Olga Kaouki*, *Giannis Gkoutzamanis*, *Christina Zoupi*, *Michalis Filios*, *Mariliz Karakonti-Diolantzi*, *Theano Mpampertsi*, *Kuriakos Galanis*, *Korina Mossiou*, *Thodoris Ntoulias*, *Manolis Dougramatzis*, *Vasilis Siafakas*, *Kostantinos Zafeiris*, *Haris Zachariadis*, *Francesco Puglierin*, *Anna Zografou*, *Thanasis Parasakis*, *Paris Bourtsoukidis*, *Kostas Rigopoulos*, *Giannis Tsotras*, *Viki Antonopoulou*, *Vassiliki Mpaka*, *Apostolos Mpaliatsos*, *Chryssa Vamvakaki*, *Thymios Kalomoiris*, *Thomi Kotzamani*.

Finally, I would never have done this without the care, companionship and love of my wife *Stavroula*, who actively participated in this endeavor in her own special way, as always. I dedicate this work to her and to our two sweet children, *Marilia* and *Giannos*.

## ABSTRACT

---

Inter-basin water exchanges can be quite important in climatic-scale numerical studies simulating the circulation and hydrographic characteristics of neighboring oceanic basins connected through narrow straits. The crucial role of the interaction between the Mediterranean and the Black Seas is often overseen in simulations of the Aegean Sea, which rely mostly on parameterizations to describe the exchange, essentially decoupling the two basins. In this study, the fully interconnected Eastern Mediterranean–Black Sea system is simulated for the historical period (1985–2015), with an emphasis on the Aegean Sea, using realistic boundary conditions (lateral, atmospheric and hydrological), and a hydrodynamic fully three-dimensional ocean modeling system. The setup of such a configuration is thoroughly described and the performance of the 30-year hindcast product is validated exhaustively against observations and model results, by evaluating the representation of surface fields, circulation, three-dimensional hydrographic characteristics, volumetric water exchanges, and the spatio-temporal variability of the above. The comparison shows a substantial improvement compared to modeling studies that do not include the interaction, and a reliable reproduction of the system’s variability in temporal scales ranging from days to inter-annual and decadal-long, and a fairly accurate reproduction of the mean linear trends of change of the basin’s characteristics, for this 30-year period. Moreover, due to the free-run configuration of the simulation (i.e., absence of data assimilation schemes) no additional input is required other than the respective boundary conditions, making it possible to reliably extend the same setup for scenarios where observational data are not available, such as in future projections. Simulation results are further examined with respect to physical processes. Analysis of water, heat and buoyancy fluxes over the Aegean Sea, demonstrates the large influence of the Dardanelles inflow to the basin’s thermohaline functioning, and the particular behaviour of the basin as the region of highest buoyancy flux variability in the Eastern Mediterranean. Finally, the appearance of marine and atmospheric heatwaves over the region is examined in an effort to deduce a possible reinforcing mechanism between the two domains during co-occurring events, with the first results supporting such a mechanism.



# CONTENTS

---

Publications	xi
Acknowledgments	xv
Abstract	xvii
List of Figures	xxi
List of Tables	xxvii
<b>1 Introduction</b>	<b>1</b>
1.1 The Area of Study . . . . .	1
1.2 Description of the Topic . . . . .	3
1.3 Initial Approach and Preliminary Work . . . . .	4
1.4 Finalizing the Research Strategy . . . . .	8
<b>2 Methodology</b>	<b>13</b>
2.1 Numerical Simulation . . . . .	13
2.1.1 Model Configuration . . . . .	13
2.1.2 Output & Resources Management . . . . .	19
2.1.3 Realistic Forcing . . . . .	21
2.2 Definitions & Dataset Preparation . . . . .	22
2.2.1 Validation Datasets . . . . .	22
2.2.2 Hydrodynamic Properties at the Straits . . . . .	25
2.2.3 Surface Field Preparation . . . . .	27
2.2.4 Definitions on Heatwave Events . . . . .	28
2.2.5 Atmospheric Model . . . . .	32
<b>3 Results &amp; Applications</b>	<b>35</b>
3.1 Evaluation of Simulation Performance . . . . .	35
3.1.1 Sea Surface Temperature . . . . .	36
3.1.2 Sea Surface Elevation . . . . .	38
3.1.3 Water exchange – properties at the straits . . . . .	40
3.1.4 General Circulation . . . . .	46
3.1.5 Column Structure – Profiles . . . . .	50
3.1.6 Dense Water Formation . . . . .	52

3.2	Air-Sea Interactions . . . . .	54
3.2.1	Heat Fluxes . . . . .	55
3.2.2	Fresh-water Fluxes . . . . .	58
3.2.3	Buoyancy Fluxes . . . . .	58
3.2.4	Principal Component Analysis . . . . .	63
3.3	Marine Heatwaves . . . . .	68
3.3.1	Detection & Metrics . . . . .	68
3.3.2	Concurrent Events . . . . .	73
4	Discussion	79
4.1	Simulation Performance . . . . .	79
4.2	Applications . . . . .	84
5	Conclusions	87
Α' ΕΚΤΕΝΗΣ ΠΕΡΙΛΗΨΗ ΣΤΑ ΕΛΛΗΝΙΚΑ (Extensive Summary in Greek)		95
Bibliography		109

## LIST OF FIGURES

---

Figure 1.1	Bathymetry of the Mediterranean Sea in meters. The largest sub-basins, seas and gulfs are indicated, as well as all the straits that divide large masses of water. Areas known as dense water producers are indicated with <b>red</b> ellipses. The locations of major river outflows which are mentioned in this study, are indicated with <b>green</b> circles. . . . .	2
Figure 1.2	River shape files for the Black Sea catchment area ( <b>left</b> ). Water travel times from each point in that area to the corresponding river outflow point is calculated using the river shape distances and a mean water velocity of $1 \text{ m s}^{-1}$ ( <b>right</b> ). . . . .	6
Figure 1.3	Combined validation index for each Artificial Neural Network ( <b>ANN</b> ) configuration with different number of hidden neurons in the first and second layer. Larger values signify better performance. . . . .	7
Figure 1.4	(a) River outflow as calculated by the output of a single <b>ANN (red)</b> , with 10 neurons in the first layer and 3 in the second, compared to the hydrologic model data ( <b>black</b> ). (b) Outflow for the ensemble of the 5% best performing <b>ANNs</b> (including the one in (a)), plotted together with their average ( <b>red</b> ), and the hydrological model outflow ( <b>black</b> ). The vertical blue line in all plots, signifies the separation between the training dataset (on the left) and the testing one (on the right), while outflow in all plots is in normalized units. . . . .	8
Figure 2.1	Spatial coverage of the individual sub-basins in the Eastern Mediterranean-Black Sea system, as defined within this study. Azov Sea (AZV), Black Sea (BLK), Marmara Sea (MAR), Aegean Sea (comprised by North Aegean, NAG and South Aegean, SAG), Levantine Sea (LEV), Ionian Sea (ION), Adriatic Sea (ADR), and Tyrrhenian Sea (TYR). Dashed lines indicate the mid-sections upon which potential density is calculated. . . . .	15
Figure 2.2	Grid geometry of the simulation. The equivalent square area grid size of the simulation is shown in color-scale. The final grid is composed of $512 \times 1024$ horizontal points, with 30 vertical sigma levels. . . . .	16

Figure 2.3	Examples of $\sigma$ -surface vertical allocation using <code>Vtransform=2</code> and <code>Vstretching=2</code> , for 30 (left) and 20 (right) layers. This stretching of surfaces allocates more layers closer to the surface and the bottom where the dynamics are more intense [Adapted from <a href="https://www.myroms.org/wiki/Vertical_S-coordinate">https://www.myroms.org/wiki/Vertical_S-coordinate</a> ]. . . . .	18
Figure 2.4	Geographic coverage of the two numerical grids. For the atmospheric COSMO Climate Limited-area Modelling ( <b>CCLM</b> ) simulation with <b>black</b> , and for the ocean Eastern Mediterranean Black Sea System ( <b>EMBS</b> ) simulation with <b>blue</b> . . . . .	32
Figure 3.1	Time-averaged <b>SST</b> for the whole simulation period (1985–2014). <b>(a)</b> simulated, <b>(b)</b> bias from satellite ( <b>EMBS–AVHRR</b> ), <b>(c)</b> <b>RMSE</b> , and <b>(d)</b> Pearson's R-coefficient for the deseasoned timeseries. All values in degrees Celsius. . . . .	36
Figure 3.2	Basin-averaged monthly <b>SST</b> for the whole Eastern Mediterranean–Black Sea system. <b>(a)</b> <b>SST</b> timeseries, <b>(b)</b> deseasoned signal (monthly anomalies), and <b>(c)</b> seasonal <b>SST</b> cycle. All values in degrees Celsius, for satellite reanalysis (black) and <b>EMBS</b> simulation (red). . . . .	37
Figure 3.3	Sub-basin temporal-averages of zero-centered <b>ADT</b> for the period 1985 – 2014, for the <b>EMBS</b> simulation and <b>AVISO</b> satellite reanalysis, with Bias ( <b>EMBS–AVISO</b> ) and <b>RMSE</b> . All values are in centimeters (cm). . . . .	38
Figure 3.4	Horizontal gradient of surface elevation in $cm\ km^{-1}$ , and barotropic component of geostrophic currents (red arrows), for the period 1985 – 2014. <b>(a)</b> <b>EMBS</b> simulation, and <b>(b)</b> <b>AVISO</b> satellite reanalysis. . . . .	39
Figure 3.5	At the left column, time-series of spatially-averaged, zero-centered <b>ADT</b> in different sub-basins, for <b>AVISO</b> satellite reanalysis (black) and <b>EMBS</b> simulation (red). At the right column, as above with the seasonal cycle removed (deseasoned). All values in meters (m). . . . .	40
Figure 3.6	<b>(a)</b> Mean composite Froude number distribution in the Bosphorus strait, for the 1985–2015 period. <b>(b)</b> Percentage of days with supercritical flow ( $G^2 > 1$ ) for the same period. <b>(c)</b> Timeseries of composite Froude number, as calculated along the midsection of the strait. Horizontal lines correspond to the position of black dots in (a) and (b). Point B2 corresponds to the southern Bosphorus sill. . . . .	41
Figure 3.7	As in Fig. 3.6, for the Dardanelles strait. Point D4 corresponds to the Nara passage. . . . .	42

Figure 3.8	Volumetric water exchange at Dardanelles ( <b>left</b> ) and Bosphorus ( <b>right</b> ), for the two-layers flow. The upper and lower layer flows ( <i>y</i> -axes) are compared to the net exchange ( <i>x</i> -axes). Results of <b>EMBS</b> simulation are shown with circles, while results from the model of Maderich et al. described in Section 2.2.1, are shown with triangles, for the whole period in monthly-averaged values. . . . .	43
Figure 3.9	Time-series of net volumetric flow: <b>(a)</b> at Dardanelles, <b>(b)</b> at Dardanelles for the period denoted with the gray box, and <b>(c)</b> at Bosphorus. Comparison between the <b>EMBS</b> simulation, the model of Maderich et al., and 1-year-long observations at Dardanelles strait from Jarosz et al. described in Section 2.2.1, using daily values and monthly averages. . . . .	44
Figure 3.10	Seasonally-averaged vertical cross section of potential temperature, along a transect in the Dardanelles-Marmara Sea-Bosphorus line. Horizontal axis spanning from the Dardanelles exit at the Aegean to the Bosphorus exit at the Black Sea. <b>(a)</b> Winter JFM, <b>(b)</b> spring AMJ, <b>(c)</b> summer JAS, and <b>(d)</b> autumn OND. Nara passage in the Dardanelles is located around the 50 km mark, and the southern Bosphorus sill at the 400km mark. . . . .	44
Figure 3.11	Same as in Figure 3.10, for salinity. <b>(a)</b> Winter JFM, <b>(b)</b> spring AMJ, <b>(c)</b> summer JAS, and <b>(d)</b> autumn OND. . . . .	45
Figure 3.12	Currents and potential density for the period 1985–2014, vertically weight-averaged between <b>(a)</b> 0–50 m, <b>(b)</b> 50–400 m and <b>(c)</b> 400 m to maximum depth. Potential density is indicated with red contour lines. In <b>(a,b)</b> , increments of $1 \text{ kg m}^{-3}$ are used for solid lines, and $0.5 \text{ kg m}^{-3}$ for dashed lines, while in <b>(c)</b> , $0.2 \text{ kg m}^{-3}$ for solid lines, and $0.05 \text{ kg m}^{-3}$ for dashed lines. . . . .	47
Figure 3.13	Zonal and meridional overturning streamfunctions for the period 1985–2014. Black contours indicate potential density along the midsection of the domain, which is depicted with dashed lines in Figure 2.1. . . . .	49
Figure 3.14	North Aegean Sea $\partial/\text{S}$ diagram containing all profiles (casts) for the period 1985–2014, and average vertical profiles of S, $\partial$ and $\sigma_0$ in the North Aegean Sea. Observations (blue), <b>MFS</b> simulation (green) and <b>EMBS</b> simulation (red) both calculated using profiles at the same place and time as the observations. The range of one standard deviation is shown with dashed lines as a measure of overall variability. Additional metrics for the averaged profiles (Bias, <b>RMSE</b> and R-coefficient) are shown for the two simulations compared to observations, with all correlations being statistically significant ( <i>p</i> -value < 0.01). . . . .	50

Figure 3.15	Same as in Figure 3.14, for different basins. . . . .	51
Figure 3.16	Hovmöller diagrams of potential density with depth for the 1987 – 2014 period at Skyros basin, central-north Aegean Sea (~39° N, 25° E), as simulated by the two modeling systems ( <b>EMBS</b> and <b>MFS</b> ). Color-scale contours have a spacing of 0.05 kg m <sup>-3</sup> , while black contours are shown every 0.5 kg m <sup>-3</sup> . . . . .	53
Figure 3.17	Time-series of daily surface salinity (upper 10 meters) in the western Marmara Sea. (a) Individual grid cells ( <b>black</b> ), and spatially averaged over the whole area ( <b>red</b> ). (b) Salinity anomaly of spatial averages ( <b>blue</b> ). . . . .	55
Figure 3.18	Mean heat flux over the eastern Mediterranean and the Black Seas over the 1985–2015 period. The negative sign signifies heat loss, positive signifies heat gain by the sea. . . . .	56
Figure 3.19	Mean heat-flux components over the Eastern Mediterranean and Black Seas over the 1985–2015 period. . . . .	56
Figure 3.20	Seasonal cycle of the four heat-flux components over the Aegean Sea, in daily values for the 1985–2015 period. . . . .	57
Figure 3.21	Mean water fluxes in equivalent meters per year at the surface, for the period 1985–2015. Evaporation (top left), Precipitation (top right), and the Net ( $E - P$ ) water flux (bottom) are indicated with positive values upward and negative values downward. . . . .	59
Figure 3.22	Seasonal cycle of Evaporation, Precipitation and Net water flux ( $E - P$ ) over the Aegean Sea, in daily values for the 1985–2015 period. . . . .	60
Figure 3.23	Buoyancy flux in the Aegean Sea due to the thermal component (see Eq. 2.5). Climatological mean (left panel), and seasonal (smaller panels to the right), for the 1985–2015 period. . . . .	60
Figure 3.24	Buoyancy flux in the Aegean Sea due to the haline component (see Eq. 2.5). Climatological mean (left panel), and seasonal (smaller panels to the right), for the 1985–2015 period. . . . .	61
Figure 3.25	Mean net buoyancy flux in the Aegean Sea due to both the thermal and the haline components (see Eq. 2.5), for the 1985–2015 period. . . . .	62
Figure 3.26	Temporal evolution of weighted-mean potential density averaged over the entire Aegean basin. Monthly time-series ( <b>blue</b> ), de-seasoned signal (i.e. monthly – climatology) of interannual variability ( <b>green</b> ), and a low-pass filtering of the de-seasoned with a Butterworth filter and a cutoff frequency of 1 year ( <b>red</b> ). . . . .	62

Figure 3.27	Temporal variability of buoyancy fluxes, as described in Eqs. 2.5 and 2.6: surface thermal component (a), surface haline component (b), surface buoyancy flux (c), lateral buoyancy flux from Dardanelles (d). Finally all the fluxes are added to calculate the total buoyancy flux at the surface of the Aegean Sea (e) . . . . .	63
Figure 3.28	The first three EOF modes (1 to 3) for surface buoyancy flux, and the associated Principal Component (PC) time-series. In parentheses, the percentage of the total variability that each mode explains. See text for an explanation on units. . . . .	66
Figure 3.29	Same as in Figure 3.28, for EOF modes 4 to 6. . . . .	67
Figure 3.30	Detection metrics for marine heat waves (MHWs) in the Aegean Sea, after applying the Hobday et al., 2016 definition on EMBS simulation Sea Surface Temperature (SST) data (1985–2015). Total MHW number (top left), mean duration (top right), mean intensity (bottom left) and ecosystem stress index -as expressed in Eq. 2.7 using proportional weighing of factors (bottom right). The black rectangle designates the area over which the timeseries of Fig. 3.31 is calculated. . . . .	69
Figure 3.31	Daily SST timeseries for the 30-year simulation (in blue), spatially-averaged over the north Aegean Sea (black rectangle in Fig. 3.30). The equivalent climatology (black) and local threshold (red) are also shown. The resulting MHW periods are designated with gray bands. . . . .	70
Figure 3.32	Mean anomalies for the atmospheric (top) and sea surface temperatures (bottom), during three distinct heatwaves (autumn 1994, summer 2007 and winter 2010–2011). The averaging windows for these three periods, coincide with extensive MHWs that took place in the Aegean Sea (see also Fig. 3.31). . . . .	72
Figure 3.33	Timeseries of daily SST anomalies, averaged over the Aegean Sea (blue) and globally (orange). Linear fits of the global and local warming trends for the 30-year period are also shown (tested for statistical significance with MK-test). . . . .	73
Figure 3.34	Relation between local and global warming-trends, for temperature data of (a) the atmospheric model and (b) the ocean model, for the period 1985–2015. A warming-trend ratio larger than (smaller than) one, means that the local trend is greater than (less than) the global trend. Black crosses designate statistical significance. . . . .	74
Figure 3.35	Surface heatflux anomaly during days with co-occurring marine-atmospheric heatwaves, as simulated by the EMBS model for the 1985–2015 period. Positive values designate excess heat flowing into the ocean; black crosses designate statistical significance. . . . .	75

Figure 3.36	Conceptual schematic of heatwave flux direction at the atmosphere-ocean interface during winter and summer heatwaves (not to scale). The fields of Fig. 3.37 represent what is portrayed here as <i>Anomaly</i> . . . . .	76
Figure 3.37	Comparison of seasonal surface heatfluxes during standalone atmoshperic, standalone marine and concurrent marine-atmospheric heatwaves, in the Aegean Sea. <b>Top row:</b> Anomaly of surface heatflux during days of <i>concurrent</i> events ( $Q_{conc.}$ ), with respect to days of only <i>atmospheric</i> heatwaves ( $Q_{atm.}$ ). <b>Middle row:</b> Anomaly of surface heatflux during days of <i>concurrent</i> events ( $Q_{conc.}$ ), with respect to days of only <i>marine</i> heatwaves ( $Q_{ocean}$ ). <b>Bottom row:</b> Anomaly of surface heatflux during days of <i>concurrent</i> events ( $Q_{conc.}$ ), with respect to days of either <i>marine</i> or <i>atmoshpetic</i> heatwaves( $Q_{[atm. OR ocean]}$ ). Positive values (red) designate heatflux into the ocean: ( <i>atmosphere</i> → <i>ocean</i> ), and vise versa (for a thorough interpretation see text). . . . .	77
Figure 4.1	Known surface circulation patterns of the Eastern Mediterranean, as reproduced by the assimilated Mediterranean Forecasting System ( <b>MFS</b> ) simulation for the 1987–2007 period (Adopted from Pinardi et al., 2015). Names of these circulation features are provided in the legend, along with a designation of whether they are also represented by the <b>EMBS</b> simulation properly (green), or partially (yellow), as demonstrated by the surface circulation of Fig. 3.12. . . . .	81
Figure 5.1	Comparison of a true-color satellite picture taken on June 25 2003, with the surface field from <b>EMBS</b> simulation for the same day. In the satellite picture, high concentrations of a natural tracer (e.g. coccolithophores) that changes the color of the surface waters within the Sea of Marmara, is dispersing and diffusing into the Aegean Sea. In the <b>EMBS</b> simulation figure, the meticulous calibration of the color-map for the surface salinity field, reveals a similar pattern. . . . .	92
Figure A.1	An artist's impression of the talk during the doctoral defense in Mytilene. The drawing was a sweet surprise by my friend <i>Maria</i> as a gift after the process. . . . .	120

## LIST OF TABLES

---

Table 2.1	Minimum, maximum and average grid size in km, for each individual basin (side of equivalent square area). . . . .	17
Table 2.2	List of 2-dimensional and 3-dimensional variables that are retained in the output of the simulation, in the form of daily averages. . . . .	20
Table 3.1	Mean <b>SST</b> from the <b>EMBS</b> -simulation along with metrics of the comparison with satellite reanalysis, for different basins. The Pearson's R-coeff. is only shown for the deseasoned signal while being statistically significant for all individual grid points in the domain ( $p$ -value $< 0.01$ ). . . . .	37
Table 3.2	Metrics of <b>ADT</b> (zero-centered) time-series comparison between <b>EMBS</b> simulation and <b>AVISO</b> satellite reanalysis data, for each sub-basin. Correlations are statistically significant for the whole domain ( $p$ -value $< 0.01$ ). . . . .	40
Table 3.3	Average two-layer (upper/lower) and net volumetric flow and standard deviation of flow at the Dardanelles and Bosphorus straits for the <b>EMBS</b> simulation and the box-model of Maderich et al. Comparison for the common period is first shown, while the additional comparison with observations at Dardanelles from Jarosz et al. is included for the period 2008–2009. <i>Positive (negative)</i> values denote direction towards the Aegean Sea ( <i>Black Sea</i> ). . . . .	45
Table 3.4	Climatological means and standard deviations of the various heat-flux components over the Eastern Mediterranean and Black Seas. . . . .	57

## ACRONYMS

---

- BMD **Bosphorus Marmara Dardanelles**
- BSW **Black Sea Waters**
- EMT **Eastern Mediterranean Transient**
- LOICZ **Land-Ocean Interactions in the Coastal Zone**
- MLD **Mixed-Layer Depth**
- GCM **General Circulation Model**
- EMBS **Eastern Mediterranean Black Sea System**
- SSH **Sea Surface Height**
- ROMS **Regional Ocean Modeling System**
- GFD **Geophysical Fluid Dynamics**
- CFL **Courant–Friedrichs–Lowy**
- MPI **Message-Passing Interface**
- GBCO **General Bathymetric Chart of the Oceans**
- MPDATA **Multidimensional Positive Definite Advection Transport Algorithm**
- ECMWF **European Centre for Medium-range Weather Forecasts**
- ERA **ECMWF Re-Analysis**
- HYPE **Hydrological Predictions for the Environment**
- SMHI **Swedish Meteorological and Hydrological Institute**
- ANN **Artificial Neural Network**
- SST **Sea Surface Temperature**
- CMEMS **Copernicus Marine Environment Monitoring Service**
- SSALTO **Segment Sol Multi-mission Altimetry and Orbitography**
- DUACS **Data Unification and Altimeter Combination System**
- AVISO **Archiving Validation and Interpretation of Satellite Oceanographic Data**
- ADT **Absolute Dynamic Topography**
- SLA **Sea Level Anomaly**
- MDT **Mean Dynamic Topography**
- CTD **Conductivity Temperature and Depth**
- MFS **Mediterranean Forecasting System**
- BSMFC **Black Sea Monitoring Forecasting Center**
- NEMO **Nucleus for European Modeling of the Ocean**
- AVHRR **Advanced Very High Resolution Radiometer**
- RMSE **Root Mean Squared Error**

- EMDW Eastern Mediterranean Deep Waters  
LIW Levantine Intermediate Waters  
ALERMO Aegean and Levantine Eddy Resolving Model  
BIOS Adriatic-Ionian Bimodal Oscillating System  
HW heat wave  
AHW atmospheric heat wave  
MHW marine heat wave  
CCLM COSMO Climate Limited-area Modelling  
NCEP National Centers for Environmental Prediction  
OISSTV2 Optimum Interpolation Sea Surface Temperature version 2  
GRNET Greek Research and Technology Network  
MODIS Moderate Resolution Imaging Spectroradiometer



# INTRODUCTION

---

*"Though I'm past one hundred thousand miles  
I'm feeling very still  
And I think my spaceship knows which way to go..."*

— David Robert Jones, *Space Oddity*

IN THIS CHAPTER: An introduction to the main concepts of this dissertation. The background information is presented together with a description of relevant literature and the scientific questions at hand. The initial -not so self-evident- approach to the problem is described and some preliminary results that occurred from it are shown. Finally, the research goals are formulated and the research strategy is presented.

## 1.1 THE AREA OF STUDY

The Mediterranean and the Black Seas constitute two neighboring and communicating marine basins which correspond to two contrasting textbook examples of a concentration and a dilution basin, respectively, regarding their thermohaline functioning and overturning circulation (Sverdrup et al., 1942). Thus, the Mediterranean exports dense water to its neighboring basins, while the Black Sea exports light, brackish water to the Mediterranean. The strongest signature of this contrasting behavior is recorded in the water exchange between the two basins through the system of the Bosphorus Strait, Marmara Sea and Dardanelles Strait (referred hereafter as **BMD** System, see Fig. 1.1), where the impressive intensity, stability and contrast between the surface and subsurface currents provided the stimulus to Count Luigi Ferdinando Marsigli in 1685 to found modern physical oceanography by attributing the exchange flow to the contrasting salinity of the two basins (Pinardi et al., 2018).

The important role of connecting straits in determining the oceanographic characteristics of the Mediterranean has been described in the past through several works (e.g., Astraldi et al., 1999; Dietrich et al., 2008; Sannino et al., 2009). The Gibraltar exchange is almost two orders of magnitude higher than the exchange through the **BMD** system, thus at first glance it appears that the latter can be ignored in either long-term hindcasts or climatic projections of the Mediterranean cir-

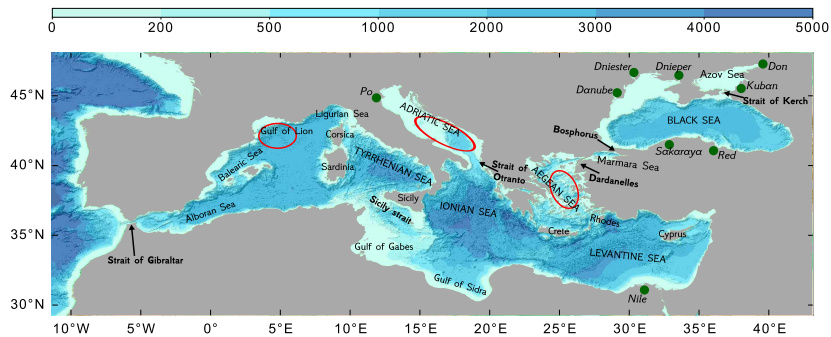


Figure 1.1: Bathymetry of the Mediterranean Sea in meters. The largest sub-basins, seas and gulfs are indicated, as well as all the straits that divide large masses of water. Areas known as dense water producers are indicated with red ellipses. The locations of major river outflows which are mentioned in this study, are indicated with green circles.

culation. And indeed, this would be the case if the Aegean Sea, first receptor of the Black Sea waters into the Mediterranean, would not also be an alternative (to the Adriatic) source of Eastern Mediterranean Dense Waters (Malanotte-Rizzoli et al., 1999; Roether et al., 2007). The inflow of Black Sea Waters (**BSW**) in the north Aegean tends to hinder dense-water formation in the following ways: (a) the lateral buoyancy inflow (in the form of light **BSW**) locally reduces surface density and increases upper water-column stratification and (b) the much lower temperature of **BSW** relative to the underlying Aegean/Levantine water masses drastically reduces heat losses from the sea to the atmosphere in the winter (Tragou et al., 2022). The North Aegean Sea (despite being a continuous buoyancy importer from the Black Sea) has been reported as the triggering region for the massive Eastern Mediterranean Transient (**EMT**) event (Gertman et al., 2006; Zervakis et al., 2000). Therefore, the exchange through the straits is considered a regulating factor of the Aegean Sea buoyancy budget and, consequently, of the overturning circulation of the Eastern Mediterranean Sea (Zervakis et al., 2000). Moreover, several processes can be connected to dense water formation in the Aegean Sea, characterized either as a precursor, an indirect effect, or a result of these events. As one example of such processes, positive salinity anomalies have been observed at the near-surface / upper-layer waters of Marmara Sea in early 1987 as described in (Beşiktepe et al., 1994), with a major formation event following shortly after in the Aegean. The increased salinity (thus density) of these waters out-flowing and mixing into the North Aegean Sea, is a factor that could either occasionally amplify the basin's potential for dense water formation, or even constitute part of a preconditioning mechanism.

## 1.2 DESCRIPTION OF THE TOPIC

Although the relative importance of the role of the reduced buoyancy inflow through the Dardanelles in initiating the EMT has been challenged (Vervatis et al., 2014), it is clear that a good representation of the exchange through the BMD system is required for the successful reproduction both of the vertical structure of the water column in the North and Central Aegean Seas, as well as the buoyancy budget (and thus the overturning processes) of the region. As the interannual variability of the exchange was gradually realized, more recent simulations of the North Aegean circulation have evolved from using parameterizations of the seasonal cycle of the exchange (Kourafalou & Barbopoulos, 2003; Kourafalou & Tsiaras, 2007) to exploiting the water budget of the Black Sea (Androulidakis et al., 2012; Maderich et al., 2015).

The existing literature on numerical studies simulating the interconnected Eastern Mediterranean – Black Sea basins as a fully-coupled three-dimensional hydrodynamic system may be categorized into two broad categories based on spatio-temporal extent and resolution. In one category, studies that mainly focus on simulating the exchange and hydrodynamics at the straits (e.g., Aydoğdu et al., 2018; Ilicak et al., 2021; Kanarska and Maderich, 2008; Sannino et al., 2017; Sözer and Özsoy, 2017, to mention a few). These studies usually feature high-resolution, structured or unstructured mesh grids, implementing either hydrostatic or non-hydrostatic modeling systems with various vertical discretization schemes. Many of these implementations resolve the flow with impressive accuracy and realism, nevertheless, their high computational demands lead to restrictions in either the simulation period (i.e., few months to a few years), the extent of the integration domain (i.e., regional to the straits), or both. The second category comprises of studies that simulate part of the system in climatic scales (i.e., decades of years) either as a hindcast, a future projection or both (e.g., (Mavropoulou et al., 2022; Sannino et al., 2009; Somot et al., 2008), and most simulations in Soto-Navarro et al., 2020 except one (namely, Sein et al., 2015 – see below). These studies simulate the Mediterranean Sea for longer periods of time, and use parameterizations for the exchanges at the Dardanelles and Bosphorus straits instead of numerically solving the flow. This is accomplished through various methods, some of which include imposing a seasonal cycle (deduced either from short-term observations, or short-term simulations), treating the straits as an open boundary source/sink of water, using the basins' water budget to calculate flow rates (i.e., LOICZ method), etc. This second category also includes studies that simulate the fully interconnected domain, but do so only in a two-dimensional or barotropic sense, for example surface wave or tidal dynamics simulations (e.g., Ferrarin et al., 2018). Very few studies fall outside of these two categories, namely, the recent

study by Napolitano et al., 2022, which resolves the whole system at a short-term (5 days forecast – 14 days overall) operational level while not providing validation results for the Black Sea, (Sein et al., 2015) which resolves the whole system, but in very low resolution, especially in the Eastern Mediterranean/Black Sea (almost similar to that of a GCM), thus considered of low accuracy, and the recent study by Sannino et al., 2022, which is the only equivalent to the present study (temporally and spatially), includes the whole Mediterranean and Black Seas and resolves the whole system in climatic scales. However, the validation of model performance in this recent study focuses mostly on surface fields (namely, Surface Height, Surface Temperature and Surface Salinity) and no validation results are provided for the Black Sea.

The majority of the above approaches fails to replicate the climatic behavior of the basin in a holistic fashion; in the first category of studies because of limits in coverage, temporal extent and boundary conditions, and in the second category because of the reduced variability of water characteristics in the exchange. This is expected to have a greater impact on model skill at regions closer to the exchange location (i.e., the Aegean Sea, the straits system and the benthic portion of the Black Sea), and becomes conspicuous when examining the temporal evolution of these water characteristics. Moreover, any climate-change-related signal that may exist in either basin is not conveyable to the other, limiting the ability of such setups as future projection tools. As an example of such a chain of events, which would not be adequately simulated by a simplistic parameterization of the exchange, a projected future precipitation anomaly over the Black Sea catchment area would affect the long term volumetric inflow of fresh water in the basin, changing the water characteristics of surface water inflow in the Aegean Sea, which would in turn affect the air-sea interaction through energy fluxes, and the thermohaline composition and functioning in a local sense as well as in the wider eastern-Mediterranean region.

*One way of measuring model skill in numerical models of the ocean, is quantifying the ability of the model to accurately and consistently predict or replicate observed conditions and behaviors of the oceanic system under examination. For example, the final verification of the model skill within this work can be seen in the validation section (3.1).*

### 1.3 INITIAL APPROACH AND PRELIMINARY WORK

This section describes an initial approach to the aforementioned problem that was finally not adapted into the main part of this study, but nevertheless constituted a large part of the preliminary work. For this reason, a short description is provided here with the most important results.

One of the limitations of using water budget methods for producing accurate estimates of Black Sea water outflow into the Aegean and especially the corresponding variability, is the quality and resolution of their input (i.e. precipitation, evaporation, river runoff etc.). Although the quality and high resolution of the available atmospheric variables was known already in the beginning of this research from past reanalysis

as well as future projection studies, the hydrological counterpart of the input (i.e. river runoff) was lacking at the time in either accuracy, temporal resolution and extent, or both. So, the initial planning was to use the well established water budget method, by incorporating all available atmospheric datasets as inputs for the Black Sea, and additionally produce a more accurate timeseries of river runoff for the basin. The volumetric Black Sea water outflow would be initially calculated for the past period, in order to evaluate the method, and if needed, it could also be extended to future projections<sup>1</sup>. This in combination with estimations of the outflow water characteristics (i.e. temperature and salinity) would provide a dataset of high temporal resolution, that could be used as the basis for calculating air-sea interactions in the Aegean Sea in terms of energy and buoyancy fluxes, and assessing the effect of this water outflow on local climate in the past as well as in the future.

At that time, the only known continuous dataset for river runoff was the one produced by the Swedish Meteorological and Hydrological Institute (**SMHI**) (Lindström et al., 2010), however, the dataset was only covering the period 1981–2010 in daily values, and did not include any future projections. Although an extension of the dataset was intended by the development team, the exact release time could not be determined at that point.

Because configuring and running a hydrological model for simulating the Black Sea river runoff would be a time-consuming endeavour out of the scope of this study, a different approach was decided. The available model output of river runoff, would be used in combination with precipitation data over the catchment area as input, in order to train a machine-learning algorithm that could extend the available time-series. The basic idea and underlying mechanism was that the total amount of river runoff from a specific catchment area is linked to the amount of precipitation over that area. However, there is a lag between the time of precipitation and the final runoff as well as several additional mechanisms (usually solved or parameterized in hydrological models) which add to the non-linearity of the problem, making a simple transfer function inadequate to model the relation. So, a more elaborate form of a prediction model could be accomplished by training an Artificial Neural Network (**ANN**) to reproduce their non-linear relationship.

Daily precipitation data from 1981 to 2006 at 0.5° resolution over the whole catchment area of the Black Sea was used by the WFDEI meteorological reanalysis dataset (Weedon et al., 2014). Then river shape-files for the Black Sea catchment area from the Catchment Characterisation and Modelling (CCM) activity of the European Commissions Joint Research Centre (JRC), were used to calculate the distance of each point in the

*The process of working on a long project involves decision-making which is based on the available resources at the time of conduct of the research.*

*This decision-making is often subject to change as new data or resources emerge. In the mean time however, large chunks of the research might be concluded with methods that later become superfluous, but are nevertheless interesting to share; like the ANN method in this case (see also Section 1.4).*

<sup>1</sup> Although future projections were not performed in the context of this study, it is considered good practice to develop tools that can be extended further into the past or the future than the initial planning.

precipitation data grid following the closest river route to the corresponding outflow position. Then distances were converted to equivalent water travel time for each gridpoint, using an arbitrary mean velocity of  $1 \text{ m s}^{-1}$  for the flow in the river<sup>2</sup> (Figure 1.2). This procedure provided a measure

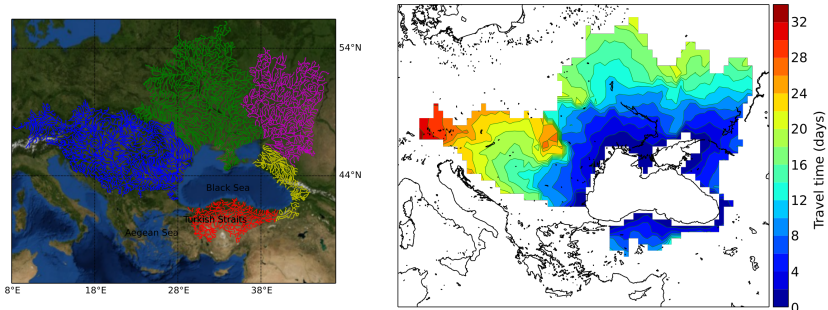


Figure 1.2: River shape files for the Black Sea catchment area (**left**). Water travel times from each point in that area to the corresponding river outflow point is calculated using the river shape distances and a mean water velocity of  $1 \text{ m s}^{-1}$  (**right**).

of the lag in days, between the precipitation in each gridpoint and the corresponding change in outflow at the river mouth. In addition, daily total river outflow in the Black Sea was calculated on a watershed level from the Hydrological Predictions for the Environment (HYPE) model, for the period 1981–2006. The daily precipitation was transformed into a one-dimensional dataset that contained for each day, the accumulated past precipitation of each gridbox that preceded that day by the number corresponding to the mapping of Fig. 1.2. All datasets were normalized for use with the neural network algorithm.

A multilayer perceptron with a feed-forward training algorithm was constructed, having as only output the total daily outflow in the Black Sea, and as inputs the precipitation for that day (as calculated above) as well as the precipitation and outflow for the last 10 days preceding that. The latter was included in order to incorporate a "memory effect" for any strain already existing in the system from past precipitation. In total, 21 inputs and one output, with two hidden layers of neurons in between.

The exact number of neurons in each layer was not fixed, instead all combinations of neural networks having 6 to 45 neurons in the

<sup>2</sup> This value was based on a collection of resources (from models, observations etc.) of river flow velocities that varied around  $1\text{ms}^{-1}$  for the rivers in this study, depending on the upstream position. However, since this was more of a statistical approach than a hydrological-modelling approach,  $1\text{ms}^{-1}$  was used as an approximate mean velocity over the whole basin. Arguably, it would be more accurate to relate this river flow velocity to terrain slope along the river course. This velocity will define the lag in days from the point of precipitation to the outflow in the Black Sea. However, not only that, but several days after that lag value are also included as inputs in the ANN, which allows for some flexibility making the selection of the exact velocity less critical.

first hidden layer, and 0 to 20 neurons in the second hidden layer were trained, and validated for their performance. The criterion for this validation, as seen in Figure 1.3, is derived using a linear combination of residual error from the ANN training process and the correlation coefficient of the derived time-series with respect to the control one. It

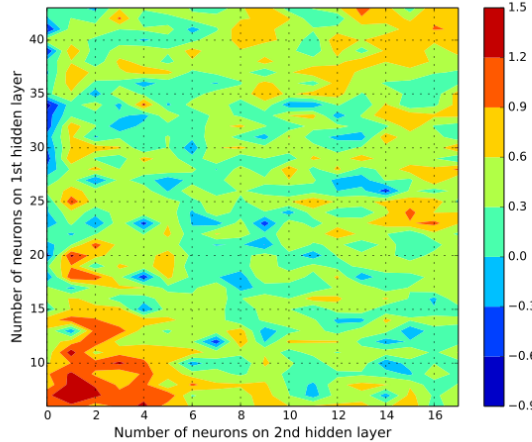


Figure 1.3: Combined validation index for each ANN configuration with different number of hidden neurons in the first and second layer. Larger values signify better performance.

should be noted that only a subset of the time-series is included in the training process while a much smaller subset is used for testing of the trained network.

It is clear that some combinations of neuron numbers in the first and second layers perform better than others. An example of this can be seen in Figure 1.4a, where the outflow as calculated by a specific combination of neurons (10 and 3 respectively) is compared to the outflow of the hydrological model. The error for this combination is exceptionally low, and the variability of the outflow is adequately reproduced by the neural network, even for the testing data which the ANN had no information on (as can be seen in both the error plot and the scatter plot). Using this index, the best 5% of the produced neural networks were selected and averaged into an ANN ensemble (Fig. 1.4b), which is the final product of this process.

Concluding the description of this method, projected precipitation datasets from a multitude of numerical models (e.g. CMIP5, SMHI, European Centre for Medium-range Weather Forecasts (ECMWF), etc.) can be used as input for this trained and tested ensemble of ANNs, in order to infer river runoff into the Black Sea for different future climate scenarios (e.g. RCP 2.6, RCP 4.5, RCP 8.5 etc.). However, as mentioned in

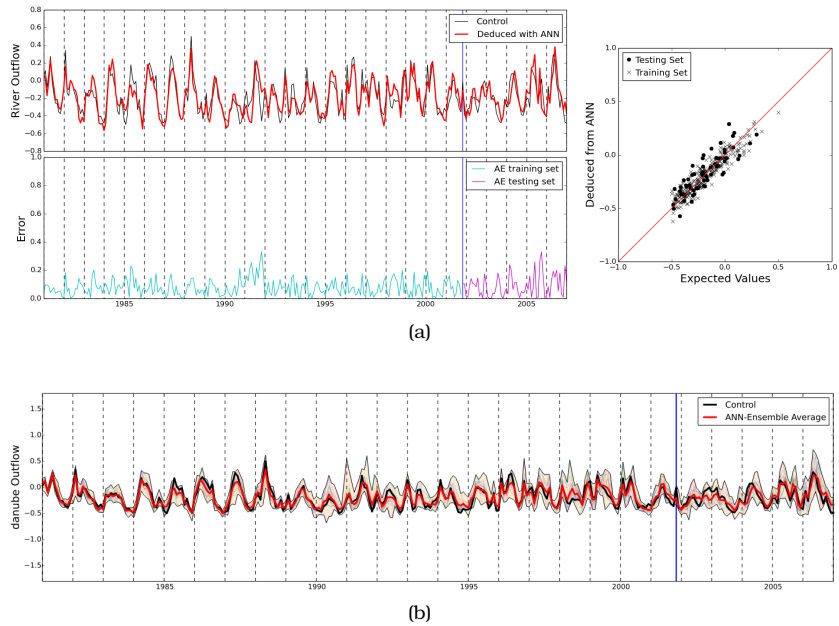


Figure 1.4: (a) River outflow as calculated by the output of a single ANN (red), with 10 neurons in the first layer and 3 in the second, compared to the hydrologic model data (black). (b) Outflow for the ensemble of the 5% best performing ANNs (including the one in (a)), plotted together with their average (red), and the hydrological model outflow (black). The vertical blue line in all plots, signifies the separation between the training dataset (on the left) and the testing one (on the right), while outflow in all plots is in normalized units.

the beginning of this section, this approach was not further investigated as new datasets were released (see next section), but is included in this introductory section as a description of the method itself.

#### 1.4 FINALIZING THE RESEARCH STRATEGY

The procedure that was described in Section 1.3 produced a valuable tool which could be used to improve the calculations of the Black Sea water budget, especially for future projections. However, shortly after concluding the analysis, daily riverine runoff data from the HYPE model were released for the whole European continent and the Black Sea, including future projections for three Representative Concentration Pathway (RCP) scenarios until the year 2100; namely RCP 2.6, RCP 4.5 and RCP 8.5. This, in combination with the better variability of the HYPE dataset and the use of land-use-changes within that model, rendered the ANN method redundant. Nevertheless, this new dataset opened

new capabilities with respect to modelling the Black Sea and a change in the research strategy was decided. Having such a high resolution dataset for every individual river runoff in the Black Sea and elsewhere, a numerical model would probably not suffer from under-specification of the fresh-water sources, and additionally it would provide a multitude of valuable oceanographic information through modelling the physical characteristics of the region (especially the Aegean Sea), regarding both the air-sea interactions as well as the three dimensional hydrodynamics of the basin, in climatic scales. This in combination with the potential for a grid construction interconnecting the Black and Mediterranean Seas, is a novel approach of increasing relevance in the scientific community, however such an approach had never been thoroughly applied for this system.

Despite the emerging importance of regarding the Black Sea – Mediterranean Sea basins as an interconnected oceanographic system, the necessity of using very high resolution grids to resolve the flow at the straits increases the numerical cost and in some cases renders such approaches prohibitive for long-term simulations. This is apparent in the scientific literature; with the exception of the aforementioned (Sannino et al., 2022; Sein et al., 2015), no other studies exist up to date that simulate the interconnected system as a whole for climatic periods of time, either in a historical or future projection sense. Aiming to an improved tool for climatic studies of the Aegean Sea, a numerical model was suitably configured for the whole EMBS. As a first application, a 30-year-long hindcast (covering the period 1985–2015) was produced, and the results are presented here in the form of an extended validation of the simulation. Simulations like this might suffer from several factors, a common one (apart from numerical instabilities) being numerical drift. Numerical drift refers to the gradual increase or decrease over time of a quantity or variable (e.g., Temperature, Salinity, SSH) at a specific region or even throughout the whole domain, which is clearly distinguishable from the inherent interannual variability of the system. This can occur in simulations with large or diverse domains, especially when the model is integrated over time for long periods with no intervention (i.e., assimilation of observational data). Practice has shown during this research, that in places of highly diverse topography and bathymetry, some grid/model configurations (be it the orientation and resolution of the grid, the selection of the mixing scheme and parameterization, or a combination of these) might produce unwanted results in terms of numerical noise, and subsequent drift in the long-term. Special care has been taken during the model configuration and grid construction process, to minimize numerical drift and to produce a tool capable of simulating long periods of time reliably, without the use of data assimilation schemes. This has been achieved through a process of trial and error in which, several different combinations of grid geometries and mixing

parameterization schemes have been tested out over simulation runs of decade-long periods, with the final configuration selection criterion being based (apart from the realistic representation of physics) on long-term drift minimization (see Section 2.1).

The present study addresses the aforementioned issues and introduces a simulation product that can realistically describe the climatology and physical oceanography of the Eastern Mediterranean with emphasis on the Aegean Sea (the region directly affected by the basin exchange), in terms of water transport, water characteristics, energy budget and buoyancy fluxes. Moreover, the dataset covers the 1985–2015 historical period for validation and reanalysis purposes, while also having the capacity to be extended into the future for the exploration of climate-change-related scenarios in the wider region.

The primary objective of this work is to make a dataset, which as a tool will be able to assist in understanding the complex oceanographic processes within this region, and to provide a better understanding on the long-term climatic variability of these processes. The main challenge here is to accurately replicate the dynamics that are inherently critical to the oceanography of the Mediterranean and Black Sea basins, in long-term climatic iterations, while maintaining the innovative part of the study: a physical connection between the two systems through a system of narrow straits and intermediary seas.

In pursuit of this main objective, several sub-objectives are devised. Firstly, the development of a high-resolution ocean numerical simulation that seamlessly integrates the Eastern Mediterranean and Black Sea and their interconnection in a single continuous grid, considering the unique hydrographic disparities of these basins. This includes a realistic reproduction of the water exchange through the Bosphorus and Dardanelles straits system –a crucial aspect often simplified or omitted in previous studies— and the consequential effects on the Aegean Sea’s stratification, water mass characteristics and distribution, and energy fluxes. Secondly, a thorough validation of the constructed numerical simulation against observational as well as modeled data, in order to verify the realistic reproduction of all the above, on decade-long numerical iterations. Finally, examining real physical processes in the Aegean Sea which are dependent on a proper description of the water exchange with the Black Sea (being the innovative part of this study), would be a first application of this new tool towards a better understanding of the physical oceanography of the region.

The innovative elements of this study arise both from the methodological approach, as well as from the applications of the research results. A significant innovation is the development of a single, continuous computational grid with varying resolution which is necessary to encapsulate both the dynamics of narrow straits, as well as that of open seas. Secondary innovative aspects of this work are, the description of the

long-term air-sea interaction and its variability under a proper simulation of the water exchange with the Black Sea, and the methodology of the marine heatwave analysis which introduces the surface heat fluxes as a measure of interaction between atmosphere and ocean during synchronous events. The innovation of this modeling system lies within its ability in simulating processes in the interconnected system, as well as its capacity of being extended into the future with minimal intervention, presenting overall a leap forward in modeling the interconnected Eastern Mediterranean and Black Sea system.



# 2

## METHODOLOGY

---

*“I’m just a soul whose intentions are good  
Oh Lord, please don’t let me be misunderstood”*

— Horace Ott, *Don’t Let Me Be Misunderstood*

**IN THIS CHAPTER:** Basic technical aspects and methodology are presented, regarding the area selection, the grid construction, the forcing and validation dataset preparation, the management of the output, and a description of an atmospheric model whose output was also used in this study. Some definitions regarding air-sea fluxes and heatwaves as well as the relevant data-preparation methods are also discussed.

### 2.1 NUMERICAL SIMULATION

#### 2.1.1 *Model Configuration*

The modeling system of choice for this simulation was the Regional Ocean Modeling System (**ROMS**) (Shchepetkin & McWilliams, 2003, 2005), a free-surface, hydrostatic, primitive equation model, featuring a highly versatile code with numerous vertical and horizontal mixing and advection schemes, as well as a terrain-following sigma coordinate system for the vertical levels.

The primary objectives of the model setup was to develop a product that (a) is able to simulate the physical characteristics of the Aegean Sea and their long-term climatic variability, as well as potential changes of those in a changing climate, while resolving interactions with the Black Sea that take place through the narrow straits of Bosphorus and Dardanelles; (b) can do so for long decadal-scale simulations without the need for corrective interventions (such as data assimilation or relaxation methods), giving it the ability to be used as both a historical simulation as well as a future projection tool; (c) does not require very high-frequency oceanic boundary conditions; and (d) is not excessively demanding of computational resources.

The above requirements determine to a large degree the simulation domain. In order to be able to dynamically reproduce potential future changes in the interaction between the Aegean and the Black Seas or its variability, an adequate simulation of the water properties of

the two basins is needed alongside the resolution of the volumetric exchange between them. The Black Sea is a water body whose physical characteristics are strongly affected by the inflow of riverine water by major rivers draining through its very large catchment area, spanning a considerable part of central/eastern Europe and western Asia. Therefore, any potential future change in the riverine water volume inflow into the basin (either anthropogenic or not), would need to be accounted for in the simulation. This dictates the inclusion of the Black Sea and the components of its hydrological cycle in the model setup. Furthermore, an open boundary at the southern end of the Aegean would render the region of interest directly dependent on the quality of boundary conditions. Hence, although the above was not an issue for historical data, it was decided as part of planning ahead to set the open boundary further west at roughly the longitude of Sardinia, using the Tyrrhenian Sea as a buffer in order to be able to use lower resolution (either temporal-wise or spatial-wise) boundary condition data for the future projections. This would also provide a larger simulation area, giving the opportunity to follow the signature of water masses entering and leaving the Aegean basin, while rendering the whole eastern Mediterranean/Black Sea region a single, compact and closed simulation system with only one and relatively short open boundary at the west. The geography of the domain, as well as the definition used here for the individual sub-basins, is presented in Figure 2.1.

The grid was constructed in a curvilinear-coordinate geometry with a variable size, in order to better describe the relatively diverse and convoluted coastline of the eastern Mediterranean/Black Sea basins. Studies of straits in the Mediterranean Sea demonstrate that the Bosphorus and Dardanelles hydrodynamic regime is further away from the hydraulic-control limit and closer to the viscous-advection-diffusive form limit, when compared to the Gibraltar strait (Hogg et al., 2001; Kanarska & Maderich, 2008; Maderich et al., 1998; Sannino et al., 2007). A past study (Sannino et al., 2007) shows that a detailed description of processes in the straits system requires the use of a non-hydrostatic model of very high spatio-temporal resolution, providing the ability to reproduce the intensity of hydraulic jumps in the straits. However, the present work investigates the extent to which a hydrostatic model is able to reproduce the hydrographic impact of the exchange on the neighboring basins over climatic time scales. To that aim, the gridline density was increased at those regions, leading to a final grid size ranging from around 5–7 km in areas of lower hydrodynamic requirements, to around 1.2 km at the straits, with an average size of 3 km for the whole simulation area. In this approach, the straits' resolution ranges from five grid cells in wider sections, down to one grid cell at their narrowest points, which in combination with the bathymetry presents a realistic topographic restraint to the flow, and can reasonably simulate—as will be shown—the

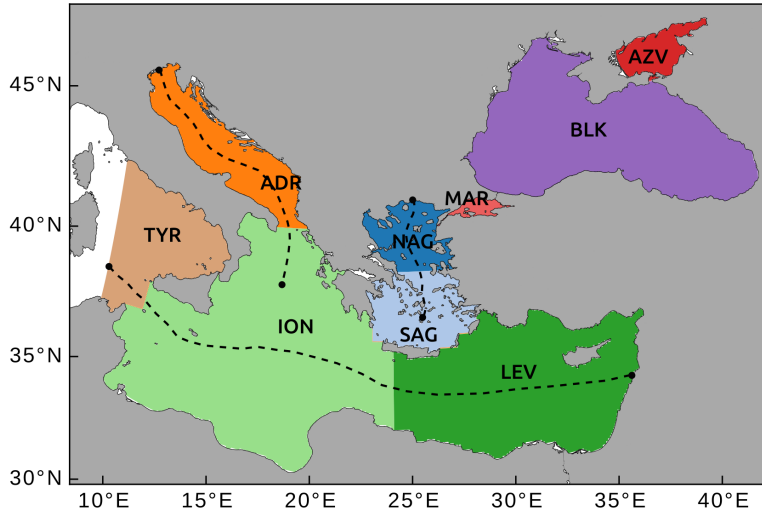


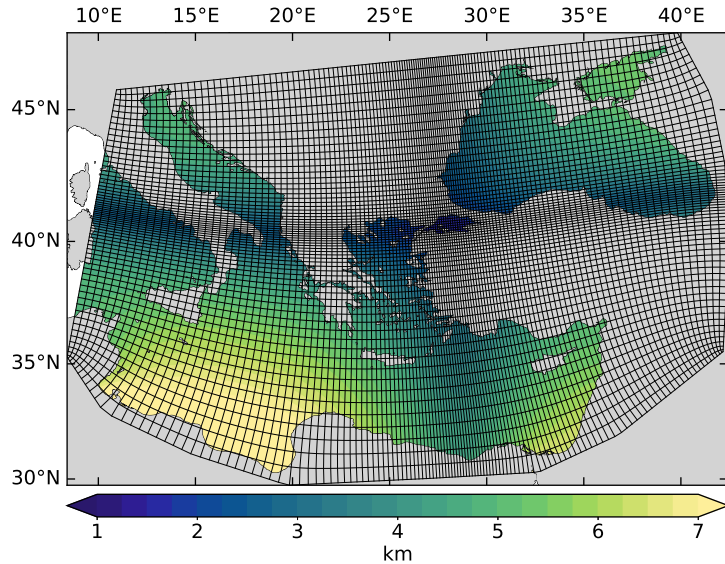
Figure 2.1: Spatial coverage of the individual sub-basins in the Eastern Mediterranean-Black Sea system, as defined within this study. Azov Sea (AZV), Black Sea (BLK), Marmara Sea (MAR), Aegean Sea (comprised by North Aegean, NAG and South Aegean, SAG), Levantine Sea (LEV), Ionian Sea (ION), Adriatic Sea (ADR), and Tyrrhenian Sea (TYR). Dashed lines indicate the mid-sections upon which potential density is calculated.

long term water exchange and water properties' advection, as well as their seasonal variability, for long-term studies. The geometry of the grid is presented in Figure 2.2, and the grid sizes for each basin in Table 2.1. The downsides of such a configuration is the deformation of the grid, and the relatively low resolution at the Northern Adriatic, the Azov Sea and at the Southern-most portion of the domain.

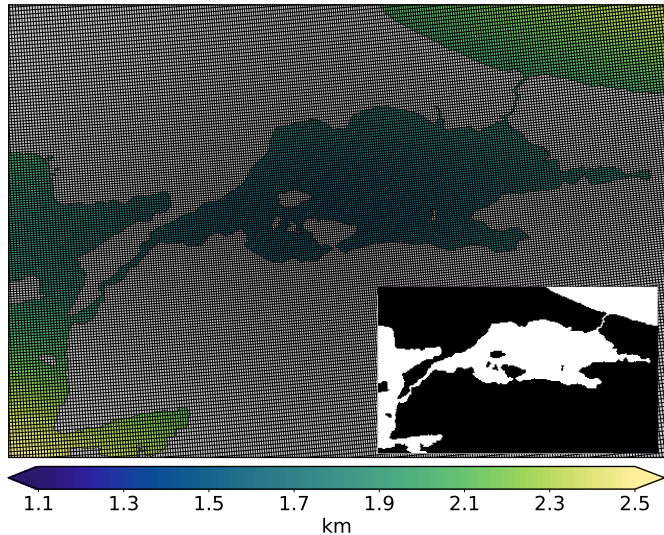
Previous experience in modeling the Aegean Sea has shown that boundary over-specification can propagate biased tracer and velocity-field values into the simulation domain. At the open boundary in the west, a sponge layer of ~10 grid points of increased viscosity and diffusivity values was used to provide a buffer zone and avoid this issue. Throughout the rest of the domain, horizontal mixing is additionally adjusted, by linearly scaling around diffusivity and viscosity coefficients' default values, with respect to grid cell area. Data output from the buffer zone is masked-out from the analysis.

In the vertical, three different configurations were tested using 25, 30 and 35 layers. The former configuration (25 layers) demonstrated occasional numerical instabilities originating within the straits system. The latter configuration (35 layers) did not provide a measurable improvement in performance compared to the 30 layer configuration, while

*Numerical instabilities within a GFD simulation can manifest themselves in a plethora of ways which, if not overcome, result in a simulation "blow-up". This mostly happens when stability criteria are surpassed (e.g. CFL condition), however, these might not be satisfied at the beginning of the simulation, but only latter on when certain hydrodynamic conditions are met.*



(a) The complete simulation domain. For clarity reasons in this figure, grid lines are drawn at eight times lower resolution ( $8\times$ ) compared to the final product.



(b) The grid in full resolution at the Dardanelles – Marmara – Bosphorus straits. In black and white the land mask derived by this grid (lower right corner).

Figure 2.2: Grid geometry of the simulation. The equivalent square area grid size of the simulation is shown in color-scale. The final grid is composed of  $512 \times 1024$  horizontal points, with 30 vertical sigma levels.

also increasing the computational cost significantly. For this reason, the configuration with 30 sigma coordinate layers of variable resolution was adopted, following the bathymetry provided by the 30 arcsecond General Bathymetric Chart of the Oceans (**GEBCO**) 2014 database (Weatherall et al., 2015), for the region of interest. For the sigma coordinate segmentation, the vertical transformation equation of A. Shchepetkin was used ( $Vtransform=2$ ) and the vertical stretching function of UCLA-ROMS of A. Shchepetkin ( $Vstretching=2$ ), as shown in Figure 2.3. In order to ensure the hydrostatic consistency of the grid and avoid pressure gradient errors, the bathymetry was smoothed via a direct iterative method (Martinho & Batteen, 2006) until the topographic stiffness ratio  $rx0$  (Beckmann & Haidvogel, 1993) and the hydrostatic instability number  $rx1$  (Haney, 1991) reached values of 0.13 and 7.39 respectively (both unit-less numbers). The baroclinic timestep was 60 sec with 20 barotropic timesteps in between, bringing the maximum barotropic Courant Number down to 0.56.

Table 2.1: Minimum, maximum and average grid size in km, for each individual basin (side of equivalent square area).

<b>Basin / Location</b>	<b>Min.</b>	<b>Average</b>	<b>Max.</b>
North Aegean Sea	1.29	1.85	2.78
South Aegean Sea	2.29	3.05	4.15
Ionian Sea	2.05	4.43	7.34
Levantine Sea	2.56	3.80	5.61
Black Sea	1.49	2.49	3.64
Dardanelles/Bosphorus	1.21	1.39	1.45
<b>Overall</b>	<b>1.21</b>	<b>3.05</b>	<b>7.34</b>

For the vertical mixing parameterization, the Mellor and Yamada level 2.5 closure scheme was chosen (Allen et al., 1995; Galperin et al., 1988; Mellor & Yamada, 1982), together with the Kantha and Clayson stability function formulation for further flexibility (Kantha & Clayson, 1994). The model’s default background values ( $5 \times 10^{-6} \text{ m}^2 \text{ s}^{-1}$ ) were used for vertical viscosity and diffusivity. For the horizontal mixing, a harmonic Laplacian operator was selected for diffusion and viscosity. A quadratic drag law was used for the parameterization of bottom stress and a free-slip condition along the horizontal boundaries. The default third-order upstream scheme was used for the advection of momentum, and the recursive-flux-corrected **MPDATA** algorithm for the advection of tracers, with a further limiter in upwind corrector fluxes for stability (Smolarkiewicz & Margolin, 1998).

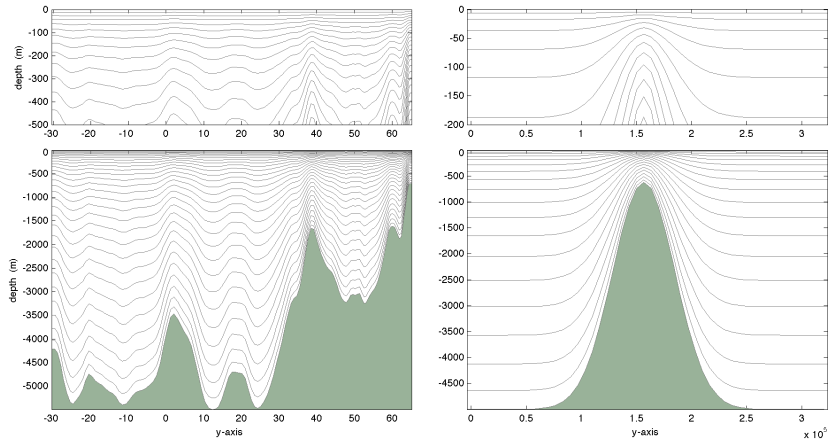


Figure 2.3: Examples of  $\sigma$ -surface vertical allocation using  $Vtransform=2$  and  $Vstretching=2$ , for 30 (left) and 20 (right) layers. This stretching of surfaces allocates more layers closer to the surface and the bottom where the dynamics are more intense [Adapted from [https://www.myroms.org/wiki/Vertical\\_S-coordinate](https://www.myroms.org/wiki/Vertical_S-coordinate)].

A combination of boundary conditions were used for the open lateral boundary at the west; more specifically, Chapman boundary conditions for the free-surface elevation (Chapman, 1985), an adaptive radiation-nudging condition for the 3D velocity and tracer fields (Marchesiello et al., 2001), and the so-called Shchepetkin (or Flather) condition for the barotropic velocity field (Flather, 1976; Mason et al., 2010). The Sea of Azov was included in the grid setup, with the intention of it functioning as a pre-mixing zone for the water inflow of Don and Kuban rivers into the Black Sea. This was designed in order to provide a more realistic representation of the water characteristics exiting the strait of Kerch, than what would result by assigning a point source at the strait. Moreover, it eliminates the need of oceanic boundary conditions in the Black Sea. Apart from the aforementioned functioning, Azov Sea fields are not considered part of the simulation and are masked-out from the analysis of the output. This is done mainly because of the relatively coarse resolution of the grid in this shallow basin, combined with considerations regarding realism of the topography/bathymetry at the strait.

Initial conditions were only provided for temperature and salinity (see Section 2.1.3), so a spin-up process was performed for the free-surface and velocity fields. A continuous 1985 year was used in a loop of two years, until the total kinetic energy of the model was stabilized (i.e., fluctuated around a value). The simulation was then initiated from the 1 January 1985, and ran for 30 years. Model output included daily averages for several relevant variables, among them tracers, barotropic

and 3D velocity fields, density, heat and salt fluxes, energy fluxes, all of which were considered valuable for dynamic or climatic studies.

Special effort was put to keep the simulation as close to realistic conditions as possible, assuring that the hindcast can be used for climate analysis, and also reproduces the climatic variability of the water characteristics and derivative physical parameters of the oceanography of the region. To that aim, realistic atmospheric forcing, open boundary conditions, river inflow data as well as initial conditions were chosen from well-established reanalysis/modeling studies (see Section 2.1.3) as external/forcing conditions. The model ran for a 30-year period from 1 January 1985 to 31 December 2014.

Finally, neither data assimilation schemes nor relaxation methods were employed during the simulation; this ensured that the same configuration could be used for future projections, using the same reproducible setup without major changes and consequent loss in model confidence.

### *2.1.2 Output & Resources Management*

The modeling system of choice (**ROMS**) offers a variety of options for the management of output and the selection of variable retention, on a software/operational level. Although this constitutes a more technical aspect of the configuration, it is shortly described here because of its relevance with the strategic planning of the project. The various decisions made at this step could result in differences of orders of magnitude in the final dataset size, and in this sense, finalizing the exact simulation setup strongly depended on the intended data analysis and usage.

The baroclinic timestep of the simulation is 60 seconds, so a comparable or slightly lower output rate (e.g. hourly or 3-hourly) is quite possible. However, such high retention rates are neither practical on a technical level because of the immense volume of data that would be created in a climatic run, nor especially useful in a physical sense due to the slowly evolving nature of the ocean at the spatial scales of this project. During the configuration process it was decided that an output rate of daily averages would be the optimum compromise between having a useful temporal resolution on multi-decade-long runs, while keeping the data volume manageable.

Regarding the specific variable selection for output, again, a thoughtful selection had to be made, because of the multitude of possibilities. Because of the intended use (i.e. study of thermohaline functioning, water transport, etc.), it was clear that the 3-dimensional fields of velocity, temperature and salinity, were necessary. In addition, 2D variables related to surface energy fluxes and fresh water fluxes would be very useful for climate sensitivity studies, because of their immediate relation to the oceanic conditions as calculated by the model, but would also facilitate tremendously the derivation of relevant fields (e.g. buoyancy

In the model-code configuration there is the option of using a set number of timesteps to provide the output in averages.

fluxes)<sup>1</sup>. A list of all the relevant variables that were finally selected for output in daily averages, is presented in Table 2.2. In addition to those, several variables that are related to the grid geometry and configuration were also exported as part of the final output product.

Table 2.2: List of 2-dimensional and 3-dimensional variables that are retained in the output of the simulation, in the form of daily averages.

	<b>Symbol</b>	<b>Description</b>	<b>Units</b>
	$\bar{u}$	: Vertically integrated horizontal velocity (x-axis)	$[m s^{-1}]$
	$\bar{v}$	: Vertically integrated horizontal velocity (y-axis)	$[m s^{-1}]$
	$\zeta$	: Surface Elevation	$[m]$
	$E$	: Evaporation at surface	$[kg m^{-2} s^{-1}]$
	$P$	: Precipitation at surface	$[kg m^{-2} s^{-1}]$
<b>2D</b>	$F_S$	: Net salt flux $(E - P) \cdot S$ (equivalent water flux)	$[m s^{-1}]$
	$Q_{NET}$	: Net heat flux through surface	$[W m^{-2}]$
	$SW$	: Short-wave radiation at surface	$[W m^{-2}]$
	$LW$	: Long-wave radiation at surface	$[W m^{-2}]$
	<i>latent</i>	: Latent heat at surface	$[W m^{-2}]$
	<i>sensible</i>	: Sensible heat at surface	$[W m^{-2}]$
	$u$	: Horizontal velocity in the model x-axis direction	$[m s^{-1}]$
	$v$	: Horizontal velocity in the model y-axis direction	$[m s^{-1}]$
	$u_{east}$	: Horizontal velocity in the eastward direction <sup>2</sup>	$[m s^{-1}]$
<b>3D</b>	$v_{north}$	: Horizontal velocity in the northward direction <sup>2</sup>	$[m s^{-1}]$
	$w$	: Vertical velocity in the model z-axis direction	$[m s^{-1}]$
	$T$	: Potential Temperature	$[^{\circ}C]$
	$S$	: Salinity	$[g kg^{-1}]$

The HPC system employed for the computational integration (HPC-ARIS in the GRNET facilities) was an *IBM NeXtScale nx360 M4* and the simulation was run using 20 thin compute nodes<sup>3</sup>, with 2 *Ivy Bridge - Intel Xeon E5-2680v2* processors of 10 cores for each node,

1 One would argue that the same variables could be retrieved from the atmospheric forcing itself. However, in that case the variables would not contain information regarding the state of the ocean as calculated by the model. With this approach the fields that are calculated by the model's bulk equations are retained, thus being more faithful to the simulation conditions.

2 Due to the grid shape, true east/north can differ to the x/y-axis locally, by several degrees (this constitutes a 2D variable called grid rotation or grid angle).

3 Out of the 426 thin nodes of the system which were available to multiple users to whom computational time was granted. The system usage was managed with a queuing protocol using the SLURM manager.

leading to a total of 400 cores for this simulation (with no hyperthreading) (<https://doc.aris.grnet.gr/>). The simulation was run in parallel using a distributed memory standard (**MPI**) and the tiling of the computational domain was arranged to  $20 \times 20$  tiles, in order to scale better with the allocated cores. The average wall-time with this scaling was  $\sim 1$  hour for 11 simulation-days, or 41 days for the 30 simulation-years (if executed in an uninterrupted fashion). Because of the inevitable occasional interruptions, either due to queuing or other reasons, the total real time added up to a total of 141 days for the 30-year simulation period.

### 2.1.3 *Realistic Forcing*

The simulation was run under realistic atmospheric forcing from the **ECMWF-ERA** interim reanalysis dataset. The temporal resolution of this dataset was 3-hourly, and the spatial resolution for all fields was  $0.125^\circ \times 0.125^\circ$  (which is provided in essence as an offline-upscaled version from  $0.75^\circ \times 0.75^\circ$ ). For a more realistic reproduction of the diurnal cycle, accumulated values were used, while fluxes of momentum and heat from the atmosphere into the ocean were derived using bulk flux parameterizations (Fairall et al., 1996). The shortwave radiation flux was distributed among the surface/upper layers, using an absorption function dependent on the optical properties of the water following specific Jerlov water types (Paulson & Simpson, 1977), as this has a significant influence on the distribution of heating of the upper water column, and consequently its stratification and vertical mixing dynamics. The Black, Azov and Marmara seas, along with the Bosphorus strait, were all assigned the eighth Jerlov water type (Black Sea), while the Dardanelles and the rest of eastern Mediterranean were assigned the second Jerlov water type (Mediterranean Sea).

Lateral boundary conditions for salinity (S), temperature (T), sea surface height ( $\zeta$ ) and velocity field (u,v) at the western boundary were calculated from daily averages of the Mediterranean Forecasting System at  $0.0625^\circ \times 0.0625^\circ$  resolution and 72 vertical z-coordinate levels (Pinardi et al., 2015; Simoncelli et al., 2019), and were interpolated to the simulation grid. The dataset covers the period between 1 January 1985 to 31 December 2014. Initial conditions for salinity and temperature for 1 January 1985 were constructed through bi-linear interpolation of the SeaDataNet II-MEDAR/MEDATLAS II project's observational dataset (Maillard & Balopoulos, 2002; Simoncelli et al., 2015).

Riverine daily volumetric inflow data (including water temperature) were introduced for rivers within the simulation regime. Over-definition of river sources could introduce numerical noise in a disproportional degree to the added realism, so only nine major rivers with the largest average volumetric flow rates were included; Danube, Dnieper, Dniester,

Don, Kuban, Red and Sakaraya in the Black Sea, and Po and Nile in the Mediterranean. For the first eight rivers draining from the European and Asian continents, data were provided from the results of the **HYPE** model of the **SMHI** (<http://hypeweb.smhi.se>, accessed on 28 January 2018) (Lindström et al., 2010), and the dataset consists of daily volumetric flow and temperature values. For the Nile river, data were provided by the University of New Hampshire—Global Runoff Data Center—Composite Runoff Fields V1.0 (<https://www.compositerunoff.sr.unh.edu>, accessed on 28 January 2018), as monthly volumetric flow climatology, which was then temporally interpolated to daily values. In general, water with salinity values between 0.5 and 30 is considered brackish, while the average salinity of world's riverine water is around 0.12 ("Venice System, Symposium on the Classification of Brackish Waters, Venice, April 8-14," 1958). This value can be much higher close to the river mouth due to sea water intrusion (Bellafiore et al., 2021); in this simulation, the salinity of all riverine water entering the domain was set to a constant value of 5, which apart from being realistic (given the cell area), also helped to avoid numerical instabilities.

## 2.2 DEFINITIONS & DATASET PREPARATION

### 2.2.1 Validation Datasets

**SST** data at a resolution of  $0.05^\circ \times 0.05^\circ$ , from the **CMEMS** reprocessed Mediterranean **SST** dataset and the **CMEMS** reprocessed Black Sea **SST** dataset, were used as part of the model's performance validation process (Buongiorno Nardelli et al., 2013; Buongiorno Nardelli et al., 2010; Pisano et al., 2016). Both datasets consist of daily SST fields fully covering the 30-year simulation period. The **EMBS** field was bi-linearly interpolated to the reprocessed satellite one. Estimated error standard deviation from the reanalysis process of converting satellite-swath data to a gridded dataset (mostly attributed to errors due to optimal interpolation of level 3 to level 4 data, and cloud-coverage-related uncertainties), is included in the **CMEMS** product and was used as a filtering variable for excluding data of lower quality. For each cell, days with an estimated error standard deviation larger than 0.5 were excluded, and monthly averages were then calculated for the comparison. Data for the Marmara Sea are absent in the **CMEMS** product, so this region is excluded from the comparison.

The all-satellites European Seas Gridded **SSALTO/DUACS** Sea Surface Height Level-4 product and derived variables altimetry was used for the validation of sea surface elevation (CMEMS, n.d.), also referred to hereafter as the **AVISO** dataset; the dataset covers the period from 1993 to 2014. Again, because of the higher resolution of the **EMBS** model compared to the altimetry dataset, the former was bi-linearly

interpolated to the latter, and monthly averages were calculated for the comparison. The **AVISO** dataset output includes the variables Absolute Dynamic Topography (**ADT**), Sea Level Anomaly (**SLA**), and geostrophic current velocities. The relation between these variables is that **ADT** is the sum of Mean Dynamic Topography (**MDT**) and **SLA**. The relevant output variable from the **ROMS** modeling system that can be used for comparison is sea surface height zeta ( $\zeta$ ), and here there are two considerations to be made. Firstly, regarding the datum of surfaces in the two datasets, **AVISO**'s **ADT** reference surface is the geoid, while in **ROMS** the default reference surface for  $\zeta$  is depth-level zero (i.e., the sea surface of the computational domain at rest). It was decided to use this default configuration during the simulation, as the two surfaces can be offset to the same datum in post-processing by subtracting the spatial-mean of **MDT** from the local **ADT**. The second consideration is with respect to the steric effect (inverse barometer effects are present in both the **AVISO** and **ROMS** datasets, and is further discussed in Chapter 4). While **ADT** in altimetry includes the contribution of steric effect (differences in surface height due to expansion or contraction of the water column), in **ROMS** the steric height is not included in **ADT**. Nevertheless, calculations suggest that steric effect contribution is very small (less than 5% of **SLA**), so it is considered adequate for the purposes of the present validation to directly compare **ADT** from altimetry with  $\zeta$  from the numerical model. Nevertheless, because of differences in the datum as mentioned above, surfaces in both datasets need to be centered around a common level (by subtracting the mean value). Due to the large extent of the simulation basin, considerable spatial variability in **ADT** exists for both the simulation and the satellite datasets, making local variability challenging to discern. For this reason the comparison is performed in two ways. In a first approach, maps of temporally averaged **ADTs** for both simulation and satellite data, are centered around zero for specific sub-basins by subtracting the spatiotemporal mean of that basin, and then the comparison is performed. This gives a better overview of the simulation performance regarding elevation of the sea surface itself, in specific areas. In the second approach, the horizontal gradient of the sea surface  $\zeta$ , and the barotropic component of geostrophic velocities are calculated by

$$\nabla_h \zeta = \frac{\partial \zeta}{\partial x} \hat{i} + \frac{\partial \zeta}{\partial y} \hat{j} , \quad (2.1)$$

and

$$u_g = -\frac{g}{f} \frac{\partial \zeta}{\partial y} , \quad v_g = \frac{g}{f} \frac{\partial \zeta}{\partial x} , \quad (2.2)$$

respectively, which makes possible the simultaneous comparison over the entire domain (with  $g$  the gravitational acceleration, and  $f$  the Coriolis parameter).

The validation of simulated volumetric water exchange through the straits is performed through the use of two datasets. One dataset comes from a theoretical study that employed a chain of hydraulic control Strait models and 1.5-dimensional ocean basin models to calculate water fluxes between the Black Sea and the Aegean Sea through the Dardanelles and Bosphorus straits (Maderich et al., 2015). These fluxes are given in daily values for the period 1985–2009, at both straits for the upper and lower layer; the upper or surface layer refers to the waters moving from the Black Sea towards the Aegean Sea, while the lower or bottom layer refers to the waters moving in the opposite direction. This dataset has been employed in previous numerical studies as boundary conditions, when the inclusion of the straits in the domain was not possible (Mamoutos et al., 2021; Mamoutos et al., 2017). The second dataset used for the validation comes from a study that used direct current velocity observations at the Dardanelles strait, to infer volumetric transport through the cross-sectional area of the strait (Jarosz et al., 2013). It is given in hourly values from 1 September 2008 to 31 August 2009. To calculate volumetric transport from the EMBS simulation current velocities, the product of each layer's cross sectional area with the normal velocity vector was taken, then for each gridbox the depth at which velocity changed direction with respect to channel direction was used as the division between the upper and lower layers, and the sum of transport was calculated for the two layers. In addition, seasonal averages of salinity and temperature were calculated along a vertical transect running from the exit of Bosphorus in the Black Sea through the Sea of Marmara and to the exit of Dardanelles in the Aegean Sea, following the same routing as in Beşiktepe, 2003, in order to examine whether the thermohaline composition patterns of the exchange at the straits are reproduced realistically when compared to hydrographic observations (Beşiktepe, 2003; Beşiktepe et al., 1994).

In order to perform a thorough and complete validation of hydrodynamic data, the entire three-dimensional domain needs to be examined. More specifically, a realistic ocean simulation is one that can adequately reproduce not only the surface or two-dimensional fields, but the entire water column. For this reason, observational datasets from oceanographic surveys describing temperature and salinity within the water column were extensively used during the model validation process. Data were provided from the MEDAR/MEDATLAS II and SeaDataNet II projects, forming a comprehensive collection of all available data from water column profile casts (Conductivity Temperature and Depths (CTDs), ARGO floats, etc.) for the Mediterranean and Black Seas (Maillard &

Balopoulos, 2002; Simoncelli et al., 2015). The available quality control of the datasets was used to include only top-grade casts; i.e., in a quality scale from 1 to 4, only casts that consisted of quality 1 data in at least 95% of the water column were selected. Preparation included making the vertical level quantization of the model (being in sigma coordinates) and that of the cast profiles relevant, by interpolating them to standard oceanographic depth levels. It is usual for simulation products to exhibit small or even large deviations from observations, making it difficult to judge and quantify whether a simulation performance is as good as it could be. Naturally, there is an upper limit in the realism one could expect from a model, so as an additional tier in this validation process, results from operational forecasting systems in the Mediterranean and Black Seas are included in the comparison, featuring state-of-the-art assimilation and surface-relaxation methods, thus making them reference products with respect to model realism. This is done in an effort to designate the upper performance limit for a simulation like **EMBS**, which is of similar resolution and setup, but runs without data assimilation. Moreover, such a comparison can showcase the importance of including the hydrodynamic interaction at the straits. The systems used for this reason here, are the Physical Reanalysis components of the **MFS** (Pinardi et al., 2015; Simoncelli et al., 2019), and the Black Sea Monitoring Forecasting Center (**BSMFC**) (Ciliberti et al., 2022; Lima et al., 2020). The **MFS** resolution is  $1/16^\circ$  with 72 vertical levels, and the simulation period is covering the range of the **EMBS** simulation (from 1985 to 2014), although years 1985 and 1986 are considered a spin-up and were only obtainable through personal communication with the authors. The **BSMFC** resolution is  $1/36^\circ \times 1/27^\circ$  with 31 vertical levels, and covering the period from 1993 to 2014. The modeling system for both **MFS** and **BSMFC** is the Nucleus for European Modeling of the Ocean (**NEMO**), and a three-dimensional variational data assimilation scheme (OceanVar) was used for temperature and salinity profiles, satellite Sea Level Anomaly along track data and satellite SST data assimilation. Simulated (**EMBS**) and control-simulation (**MFS/BSMFC**) vertical profile data are calculated at the same time and place as the observed survey profiles (MEDATLAS), and spatiotemporal averages as well as their variability are calculated and compared for the whole period within smaller areas (e.g., North Aegean Sea, Ionian Sea, etc.), in terms of average profiles.

### 2.2.2 *Hydrodynamic Properties at the Straits*

The topographic narrowing at the straits of Bosphorus and Dardanelles consists of an elongated horizontal contraction, which coincides with a vertical at one point in the straits (i.e. an oceanic sill). These contractions form control points to the bi-directional density-driven exchange at the

straits, and the flow characterization falls within a continuous regime which is limited by two extremes; one where the two-layer hydraulic solution dominates over mixing, and one where the viscous-advection-diffusive solution dominates -with velocity being limited by turbulent eddy viscosity (Hogg et al., 2001). It is shown in Kanarska and Maderich, 2008, that the corresponding hydrodynamic regimes of Bosphorus and Dardanelles straits are further away from the two-layer hydraulic solution than the Gibraltar strait, with the Dardanelles strait showcasing an even stronger dependence on turbulent friction and mixing. However, the above study concludes that the flow at the straits is still hydraulically controlled in part, especially at points of intense contraction (e.g. the Nara passage in Dardanelles, and the Bosphorus sill at its southern end).

As described in Section 2.1.1, because of the hydrostatic approximation and Reynolds decomposition employed in the ROMS model, horizontal and vertical turbulent mixing is resolved through parameterization. In this case, although turbulent mixing is indirectly calculated, the aforementioned limitation of the flow due to friction and mixing is highly dependent on the parameterization scheme used, and in any way, it is expected to represent only a rough estimate of the actual limiting factor. However, the limitation of the flow based on the hydraulic solution is still an important controlling factor, and can be estimated through the composite Froude number  $G$  (Armi & Farmer, 1986), defined as

$$G^2 = G_1^2 + G_2^2 = \frac{u_1}{g'h_1} + \frac{u_2}{g'h_2}, \quad (2.3)$$

where  $u_1, h_1$  and  $u_2, h_2$  the velocity and thickness of the upper and lower layer respectively,  $g' = g(\rho_2 - \rho_1)/\rho_2$ , with  $g$  the gravitational acceleration and  $\rho_1, \rho_2$  the densities of upper and lower layers respectively. Areas where the flow becomes supercritical ( $G^2 > 1$ ), can be regarded as points of hydraulic control.

Pratt, 2008 extends the two-layer calculation of composite Froude number to the generalized case for N-layers, which could be used in this case for the 30-layer output of the EMBS simulation. However, since observations and models used to validate the simulated water exchange follow the two-layer hydraulic differentiation and approach, composite Froude numbers are also calculated with the same approach, using Eq. 2.3 on the velocity field output of EMBS for each individual grid-cell within the straits of Dardanelles and Bosphorus. The division between upper and lower layers for each gridpoint (and consequent layer thicknesses  $h_1, h_2$ ) is determined by the change in the direction of velocities with respect to the strait's orientation, and a mean velocity is calculated for upper and lower layers ( $u_1, u_2$ ), as the weighted average of velocities in each  $\sigma$ -layer within the model (weighted on cross-sectional

area). Moreover, the density for the two layers  $\rho_1, \rho_2$ , is calculated for each gridpoint using the potential temperature and salinity fields and the thermodynamic equation of state for seawater. Again the mean potential density for upper and lower layers is calculated as the weighted average of each  $\sigma$ -layer within the model (weighted on cell volume).

### 2.2.3 Surface Field Preparation

The net surface heat flux is described as the sum of short-wave radiation, long-wave radiation, latent heat and sensible heat fluxes, by

$$Q_{NET} = Q_{SW} + Q_{LW} + Q_{latent} + Q_{sensible}, \quad (2.4)$$

which are internally calculated by the model's bulk formulas, using as input the forcing provided by ERA interim reanalysis and the ocean conditions as calculated by the simulation. The two-dimensional fields that result from the above, are then averaged in monthly, yearly and seasonal climatology for further analysis. Moreover, for the purposes of comparison to the CCLM atmospheric model (see Section 2.2.5), the daily surface heat flux (and temperature) fields -being of finer spatial resolution- are bi-linearly interpolated/remapped to the coarser atmospheric model grid (see Section 3.3).

*The retention of surface heat flux fields in the output, is activated through flags within the code.*

Due to the thermal expansion and the haline contraction of seawater, the buoyancy flux at the surface is comprised of a thermal ( $F_B^T$ ) and a haline ( $F_B^S$ ) component, and is calculated by

$$F_B = \underbrace{\frac{1}{C_p} g \alpha Q_{NET}}_{\text{thermal component, } F_B^T} - \underbrace{g \beta (E - P) S}_{\text{haline component, } F_B^S}, \quad (2.5)$$

where  $C_p$  the specific heat capacity of seawater,  $\alpha$  and  $\beta$  the coefficients of thermal expansion and haline contraction of seawater respectively,  $g$  the gravitational acceleration,  $E$  and  $P$  surface evaporation and precipitation, and  $S$  the surface salinity<sup>4</sup>.

---

<sup>4</sup> Equation 2.5 can be found in different forms either containing or not containing  $g$  in the numerator and/or  $\rho$  in the denominator. This depends on whether these constants are included in the coefficients  $\alpha$ ,  $\beta$ , and also on the desired final units of the product. In this case the final units are given in  $\text{kg m}^{-1} \text{s}^{-3}$ .

Lateral buoyancy input through a strait oriented in the  $x' - x$  direction, is expressed in equivalent surface buoyancy flux in the basin, as calculated by

$$F_B^L = - \frac{1}{A} \int_{z=-D}^0 \int_{y=-L(z)/2}^{L(z)/2} g (\rho - \bar{\rho}) u dy dz , \quad (2.6)$$

where  $A$  the surface area of the basin,  $D$  the strait's depth,  $L(z)$  the strait's width (as a function of depth),  $g$  the gravitational acceleration,  $\rho$  the density of incoming/outgoing water,  $\bar{\rho}$  the mean water density of the basin and  $u$  the water velocity in the  $x' - x$  direction.

#### 2.2.4 Definitions on Heatwave Events

During the last 20-30 years there has been a steadily increasing interest in the study of heatwaves, which in general refers to a prolonged period of extremely high temperatures in the atmosphere or in the ocean (Perkins & Alexander, 2013). This increasing interest has seen a step-up after the catastrophic heatwave event of 2003 in Europe, which resulted in tenths of thousands of mortalities, severe stress on crops and the ecosystem, forest fires, excess loss of Alpine glacier mass, threats to the water and energy supply systems, social and health system failures and great economic losses (e.g. García-Herrera et al., 2010; IPCC, 2007; Robine et al., 2008). Moreover, the oceanic equivalents referred to as marine heat wave (MHW), have been widely reported in recent years, showcasing severe damages in ecosystems and even mass mortality events of aquatic species (Cavole et al., 2016; Frölicher & Laufkötter, 2018; Garrabou et al., 2009; Holbrook et al., 2019). Because of the impact and the projected future increase in frequency of such extreme events (Collins et al., 2019; Perkins-Kirkpatrick & Lewis, 2020), the need to study, categorize and understand their underlying mechanisms is self-evident.

From the point of extreme temperature event classification, heatwaves are both statistical in nature describing the highest end of the temperature distribution (in combination with duration), but also exhibit a strong qualitative connection to the ecosystem due to the stress they can exert on the biosphere. The latter characteristic might help to track and register these events through their aforementioned effects, however, *a posteriori* heatwave detection on a diagnostic-analysis level is rarely based on either mortality or stress criteria (partly because of data scarcity). Detection of heatwaves is usually performed using a statistical approach on the more readily-available temperature records (either observational or simulated). Even so, because of the spatial diversity of earth's climate, the methods for classifying a certain event as a

heatwave, are equally diversified and largely dependent on local climate characteristics (Meehl & Tebaldi, 2004; Robinson, 2001). Meteorological organizations have all, on a national level, established their own definitions, with the World Meteorological Organization defining a heatwave as five or more consecutive days of prolonged heat in which the daily maximum temperature is higher than the average maximum temperature (1961–1990) by 5°C or more. It is clear that, the latter definition contains both statistical/objective elements, as well as more subjectively defined elements (i.e. the temperature threshold value). In recent years, several studies and global initiatives sought to introduce a more global heatwave definition; one that is based on statistical criteria which can transcend local particularities and be implemented on most locations (e.g. Kuglitsch et al., 2010; Perkins and Alexander, 2013; Russo et al., 2015), and even with a small lag, similar studies cover and focus on the MHW definition (e.g. Hobday et al., 2016; Hobday et al., 2018).

In this study, the definition of Hobday et al., 2016 is used for the detection of both atmospheric and marine heatwaves, using different duration threshold values for the two domains (see below). Within this algorithm, after calculating the daily temperature climatology in the area of study, a local threshold in terms of a percentile of highest temperatures is defined in order to characterize days that exceed the threshold, as a heat-spike. A duration criterion is then applied in order to characterize consecutive heat-spike days as a heatwave, also allowing for a break window of some days in between heat-spikes. For the detection of marine heatwaves in the dataset of this study the default configuration of Hobday et al., 2016 was used, namely, the 90th percentile as threshold for the daily SSTs, and 5 consecutive days allowing for 2 days break in between as the duration threshold. In the case of atmospheric heatwave detection, the definition of Russo et al., 2015 was adopted, using the 90th percentile as threshold of the daily maximum 2 meter temperatures, and a window of 3 consecutive days as the duration threshold, with the modification of allowing for 1 day break in between.

Heatwaves are phenomena that by definition point to an imbalance of heat input in the system (compared to the average conditions). Although the underlying forcing mechanisms for this can be many and diverse (as proposed within the aforementioned literature), the hypothesis here is that the shared interface between atmosphere and ocean and the subsequent heat exchange through it during extremely hot conditions, could potentially reinforce heatwaves in either domain. Similar hypotheses have already emerged in the literature, by studying co-occurring heatwaves and considering air-sea interactions during these events in terms of atmospheric pre-conditioning (Feudale & Shukla, 2011), coupled events (Salinger et al., 2019), air-sea-land interactions (Pathmeswaran et al., 2022), or even teleconnections between them (Mecking et al., 2019). The Mediterranean Sea however, has not received much attention

regarding coupled or co-occurring events, with the exception of Androulidakis and Krestenitis, 2022, where the Aegean, Ionian and Cretan Seas are examined with a focus on MHWs, while also assessing atmospheric winds and temperatures during those events. However, no direct connection to atmospheric heatwaves is examined. Arguably, the first step towards identifying and validating such forcing/feedback mechanisms would be the detection of coincidence of heatwaves in the two domains.

Analysis of oceanic (EMBS) and atmospheric (CCLM – see Section 2.2.5) datasets for the Aegean Sea is performed in Section 3.3 in two ways. At first, the detection method for heatwaves in both atmospheric and sea surface temperatures is applied on the raw timeseries, in order to reflect events as they actually occurred in a temporal sense. This helps to assess whether a co-occurrence of AHW and MHW can be detected in the historical period to begin with. In the second approach, the temperatures' timeseries are de-trended, by removing the global mean warming signal. This is done separately in both the atmospheric and oceanic data, in order to prevent biasing the emergence of events towards the end of the time series<sup>5</sup>. After de-trending, heatflux anomalies through the air-sea interface are also examined during heatwave events. For both aforementioned approaches the detection of heatwaves is performed locally, by applying the algorithm on the individual grid-cell timeseries. This provides spatial resolution and variability to the result and differentiates the approach from similar studies, which incorporate an additional spatial threshold in the detection method, by means of requiring a minimum area percentage to be under heatwave conditions in order to register an event over the whole region (e.g. Darmaraki et al., 2019).

Apart from the mere heatwave detection, the algorithm of Hobday et al., 2016 provides additional metrics which can be used for further characterization and classification of the events. In this study and especially for the case of MHWs, the total number of events ( $N$ ), the mean duration in days ( $\mathcal{D}$ ) and the mean intensity (or mean temperature anomaly in °C during the event –  $I$ ), are first normalized and then linearly combined into a heatwave index for ecosystem stress

$$HW_{esi} = w_1 N + w_2 \mathcal{D} + w_3 I , \quad (2.7)$$

where  $w_1$ ,  $w_2$  and  $w_3$  are weights. The idea behind this, is that given a coherent-enough spatio-temporal dataset of recorded temperature-induced stress on the ecosystem (e.g. mortality data), the weights in

---

<sup>5</sup> A warming trend within a temperature timeseries implies that the latter entries will be having larger absolute values, thus exceeding the threshold percentile easier than the initial entries, leading to a heatwave detection frequency which is skewed towards the end of the timeseries.

the equation above can be adjusted, so that the resulting  $HW_{esi}$  reflects the recorded stress on the ecosystem. Due to scarcity of such data in the Eastern Mediterranean, the calculation of  $HW_{esi}$  in Section 3.3.1 is provided with a proportional weighing ( $w_1 = w_2 = w_3 = 1$ ) for overview purposes.

Throughout the heatwave analysis in the present study the focus remains on the detection of atmospheric and marine heatwaves and coincidence rates in the two domains, however the direction of interaction between the two domains during these events is also examined through the EMBS simulated surface heat fluxes. In the case of a marine heatwave, the main drivers of the evolution of temperature  $T$  within a sea surface layer of depth  $H$  (either mixed layer or other), can be described as the sum of horizontal temperature advection and input of energy through the surface

$$\frac{\partial T}{\partial t} = - \frac{1}{H} \int_{-H}^0 (\mathbf{u} \cdot \nabla_h T) dz + \frac{Q_{NET}}{\rho C_p H} + \text{residual} , \quad (2.8)$$

with  $\mathbf{u}$  the horizontal velocity field,  $Q_{NET}$  the net surface heat flux,  $\rho$  the seawater density, and  $C_p$  the specific heat capacity of seawater (e.g. (Kataoka et al., 2017)). The residual terms in Eq. 2.8 are comprised of changes in temperature due to horizontal diffusion, and of heat fluxes through the layer's bottom interface

$$\text{residual} = - \frac{1}{H} \int_{-H}^0 \nabla_h \cdot (\kappa_h \nabla_h T) dz + \frac{q}{\rho C_p H} , \quad (2.9)$$

with  $\kappa_h$  the horizontal diffusion coefficient, and  $q$  the heat flux at the bottom interface. However, a simple scaling analysis shows that these terms have a much lower impact on the temperature evolution of the layer, as  $q \ll Q_{NET}$  and in the case of the large-scale flow in EMBS  $\nabla_h \cdot (\kappa_h \nabla_h T) \ll \mathbf{u} \cdot \nabla_h T$ .

Consequently the residual terms in Eq. 2.8 can be neglected, and the main drivers of local temperature change become: (a) the lateral advection of heat by the general circulation, and (b) the vertical input/output of heat through the sea surface; here, only the second driver will be examined. The net sea-surface heat flux  $Q_{NET}$ , is in general positive (heating the ocean) during the spring and summer months and negative (cooling the ocean) during autumn and winter months (see Section 3.2.1). For this reason, in order to distinguish the direction of the surface heatflux forcing during heatwaves, only heatflux anomaly with respect to the climatology is examined. This defines that a positive anomaly

would refer to excessive heating of the ocean, while a negative anomaly would refer to excessive heating of the atmosphere.

### 2.2.5 Atmospheric Model

Specifically for the detection of atmospheric heat waves (AHWs) and the determination of their coincidence with MHW events, atmospheric temperature data were used from an application of the **CCLM** atmospheric model, initially developed by the German Weather Service (e.g. Rockel and Geyer, 2008). The specific application used here was configured and implemented by the Climatology, Climate Dynamics and Climate Change working group of Justus-Liebig University in Giessen, Germany. The resolution was set at  $0.11^\circ$  (or  $\sim 10$  km), with the numerical grid covering Europe, the Mediterranean Sea, the Black Sea, as well as parts of central Asia, Middle-East, north Africa and Indian Ocean, including the **EMBS** grid area (Figure 2.4), and is described in more detail in (Hartmann et al., 2020; Hartmann et al., *in preparation*; Zhang et al., *in preparation*; Zhang et al., 2021). The simulation period was inclusive of the 1985–2015 **EMBS** range, and used the **ERA** interim dataset as forcing/boundary conditions (i.e. similarly to **EMBS**).

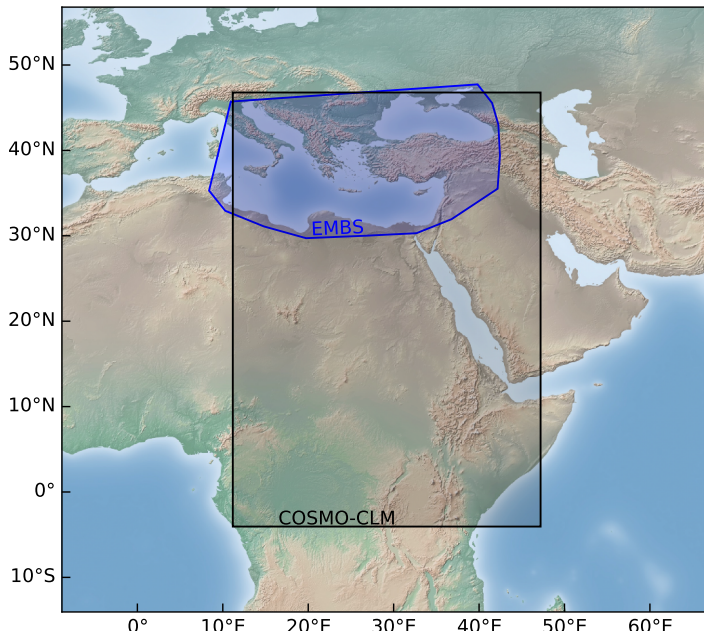


Figure 2.4: Geographic coverage of the two numerical grids. For the atmospheric **CCLM** simulation with **black**, and for the ocean **EMBS** simulation with **blue**.

Consequently, although neither one of the **CCLM** and **EMBS** simulations is coupled, they can be regarded as having an offline-coupling-like configuration with respect to each other, since they both focus on a common area, for a common period, sharing the same boundary conditions at their interface. Employing oceanic and atmospheric datasets with similar frames of reference is very useful when examining concurrent events within them. However, it should be stressed that when examining the direction of heat transfer in these events —essentially trying to determine causal relations between atmospheric and marine heat waves (**HWs**)—, the aforementioned configuration may suffer from a directional bias for the following reasons. Although these two simulations share common boundary conditions at their interface, the temporal resolution of these conditions are quite different for the two domains. In the case of the **EMBS** ocean simulation, boundary conditions of atmospheric 2-meter temperature and heat fluxes are provided by the **ERA** interim dataset in 3-hourly intervals. On the other hand, the **CCLM** atmospheric simulation receives as boundary conditions skin temperatures (**SSTs**) provided again by the **ERA** interim dataset, but interpolated from a combination of monthly and weekly intervals for the period before 2002, and from daily intervals for the period after 2002, as described in (Dee et al., 2011). Even for the latter daily intervals, they are provided by the **NCEP OISSTv2** reanalysis of satellite data, which has some key limitations, namely that satellite bias corrections require adequate in-situ observations which are very sparse in some regions, and that they may not represent actual conditions in persistently cloudy regions (according to the provider). This indicates that, while atmospheric heatwaves are clearly expressed in the forcing of the ocean model as anomalies in the daily cycle of 2-meter air temperature, marine heatwaves are not as clearly introduced as a forcing in the atmospheric simulation, because of the flattening of the **SST** time-series (due to interpolation from lower temporal resolutions, and satellite bias). This flattening might conceal the characteristic exaggerations and spikes of extreme events.

Nevertheless, due to the large thermal capacity of the ocean, this flattening is not as significant as it would be for atmospheric temperature, and it does not affect the statistical nature of the events. Both **AHWs** and **MHWs** can be easily detected in the datasets, while there is a statistical significance in their concurrency. However, caution should be taken in the determination of cause-and-effect relations when using these specific datasets, a hypothesis that requires further investigation (not performed here). It is argued that with this configuration the effect of marine events inducing atmospheric ones, could be underestimated, while the effect that atmospheric events have on marine ones remains unaffected.

As mentioned also in Section 2.2.3, for the purposes of the analysis on co-occurring heatwave detection, the simulated **SST** and surface

heatflux fields are bi-linearly interpolated/remapped to the **CCLM** model grid of 2-meter daily maximum temperatures.

# 3

## RESULTS & APPLICATIONS

---

*"Before I sink  
Into the big sleep  
I want to hear  
The scream of the butterfly"*

— James Douglas Morrison, *When The Music's Over*

**IN THIS CHAPTER:** The main part of the analysis and its results are presented. A thorough validation of the simulation against observational data is implemented and its performance is assessed. Air-Sea interactions are assessed with respect to surface heatfluxes, fresh water fluxes, surface and lateral buoyancy fluxes, and a statistical decomposition of buoyancy fluxes with principal component analysis, is performed. A heatwave detection method is applied and the conditions for co-occurrence of marine and atmospheric heatwaves are examined.

### 3.1 EVALUATION OF SIMULATION PERFORMANCE

The validation of the **EMBS** simulation performance is conducted in six steps. In the first two steps, surface fields (namely **SST** and Sea Surface Elevation) are validated against satellite observations. In the third step, a timeseries of the volumetric water exchange at the straits is compared to theoretical as well as observational studies, while seasonal averages of tracers in along-strait cross-sections demonstrate the distribution of water characteristics within the straits. In the fourth step, the general circulation both in terms of horizontal surface and subsurface currents, as well as in terms of the zonal and meridional overturning streamfunctions, is compared to known circulation patterns of the region. In the fifth step, vertical profiles of Salinity, Potential Temperature and Potential Density Anomaly are compared to both observations and state-of-the-art operational assimilated model results. In the sixth and final step, the potential for reproducing dense water formation events in the **EMBS** simulation is presented, again showcased along state-of-the-art operational assimilated model results.

### 3.1.1 Sea Surface Temperature

In this first step of the validation process, monthly-averaged **SST** observations in the form of level-4 Satellite-data reanalysis (**AVHRR**) are compared to results of the **EMBS** simulation. The spatial variability of **SST**, as observed by satellite, is closely reproduced by the simulation (Figure 3.1). Bias over the whole domain is close to  $0.55^{\circ}\text{C}$ , with largest Root Mean Squared Error (**RMSE**)/bias appearing in the Black Sea and lowest appearing in the Levantine Sea (Table 3.1). Regions of more significant deviation include areas of mesoscale gyres (see Figure 3.1b), like the Cretan cyclone (bias  $\sim+0.85^{\circ}\text{C}$ ) and Ierapetra anti-cyclone (bias  $\sim-0.50^{\circ}\text{C}$ ), the southernmost part of the Adriatic Sea (bias  $\sim+0.75^{\circ}\text{C}$ ), the eastern-southeastern part of the Black Sea (bias  $\sim+1.25^{\circ}\text{C}$ ), and the coastal area between the Nile river and Suez canal (bias  $\sim+1.00^{\circ}\text{C}$ ). The correlation between satellite and simulated **SSTs**, as described by Pearson's correlation coefficient, is above 0.98 for the whole domain due to the strong influence of the seasonal cycle. The same metric for the deseasoned signal shows high correlation of over 0.7 between simulated and observed **SSTs** for the whole domain (Figure 3.1d).

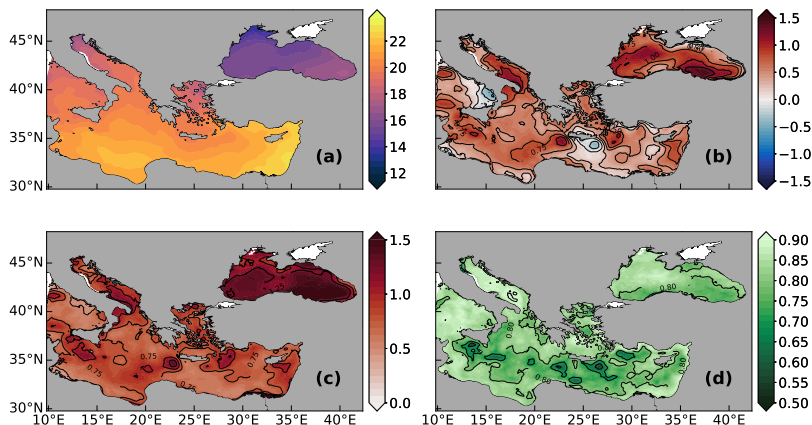


Figure 3.1: Time-averaged **SST** for the whole simulation period (1985–2014). (a) simulated, (b) bias from satellite (**EMBS–AVHRR**), (c) **RMSE**, and (d) Pearson's R-coefficient for the deseasoned timeseries. All values in degrees Celsius.

The domain-averaged temporal evolution of **SST** showcases the seasonal cycle as the most prominent source of variability in the timeseries (Figure 3.2), with the aforementioned overestimation of  $0.55^{\circ}\text{C}$  for the simulation, emerging systematically on the seasonal cycle (Figure 3.2c). The temporal variability of **SST** is reproduced accurately, with the deseasoned 1985–2014 simulated timeseries closely following the deseasoned

satellite observations (Figure 3.2b). The basin-wide long-term warming trend is underestimated, with  $0.046\text{ }^{\circ}\text{C}/\text{yr}$  for the satellite and  $0.030\text{ }^{\circ}\text{C}/\text{yr}$  for the simulation, both of which were tested for statistical significance with the Mann-Kendall test (with resulting  $s$ -values  $> 0$ , and  $p$ -values  $< 0.01$ ).

Table 3.1: Mean SST from the EMBS-simulation along with metrics of the comparison with satellite reanalysis, for different basins. The Pearson's R-coeff. is only shown for the deseasoned signal while being statistically significant for all individual grid points in the domain ( $p$ -value  $< 0.01$ ).

<b>Basin</b>	<b>SST (<math>^{\circ}\text{C}</math>)</b>	<b>Bias (<math>^{\circ}\text{C}</math>)</b>	<b>RMSE (<math>^{\circ}\text{C}</math>)</b>	<b>Pearson's R (De-seasoned)</b>
Aegean Sea	19.37	0.46	0.808	0.824
Adriatic Sea	18.62	0.66	0.952	0.852
Ionian Sea	20.86	0.58	0.802	0.790
Levantine Sea	21.55	0.40	0.771	0.783
Black Sea	15.79	0.76	1.310	0.808
<b>Overall</b>	<b>19.61</b>	<b>0.55</b>	<b>0.891</b>	<b>0.804</b>

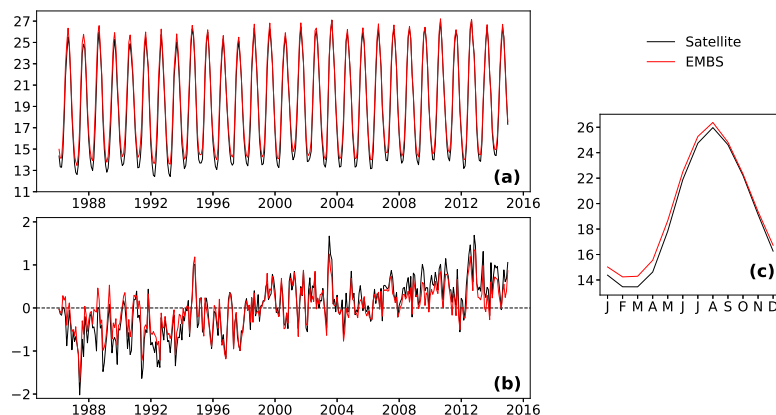


Figure 3.2: Basin-averaged monthly SST for the whole Eastern Mediterranean-Black Sea system. (a) SST timeseries, (b) deseasoned signal (monthly anomalies), and (c) seasonal SST cycle. All values in degrees Celsius, for satellite reanalysis (black) and EMBS simulation (red).

### 3.1.2 Sea Surface Elevation

A comparison of ADT as described in Section 2.2.1, between the EMBS simulation and satellite data for different sub-basins of the domain, can be seen in Figure 3.3. ADT in this analysis is zero-centered, meaning that the mean value is subtracted, which is almost the equivalent of moving the datum to zero meters. The overall shape of the sea surface for the period 1985–2014 closely resembles the one described by the satellite altimetry reanalysis product (AVISO). In combination with Figure 3.4, it can be seen that large and known elevation/flow patterns of the Mediterranean, are being reproduced qualitatively as well as quantitatively. More specifically, flows like the anti-cyclone of the North

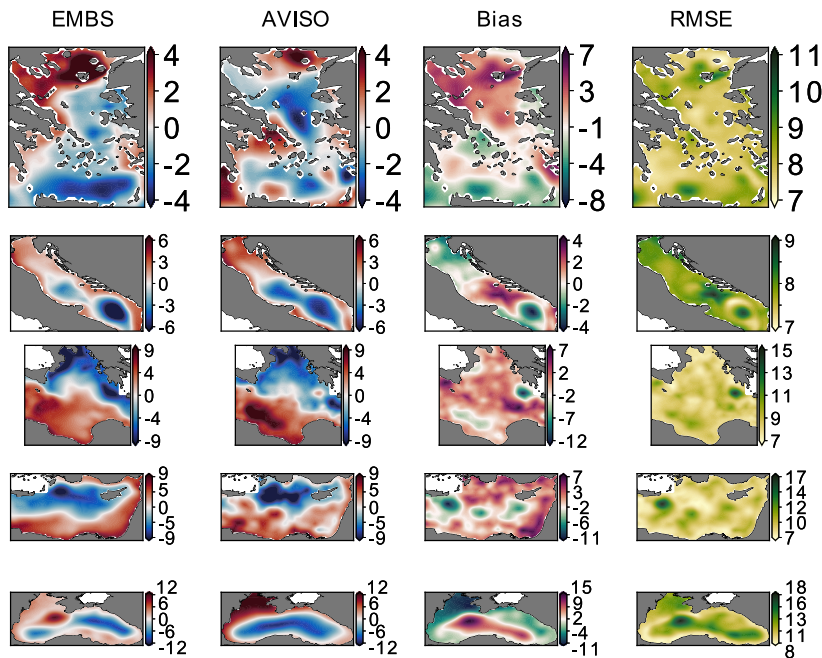


Figure 3.3: Sub-basin temporal-averages of zero-centered ADT for the period 1985 – 2014, for the EMBS simulation and AVISO satellite reanalysis, with Bias (EMBS – AVISO) and RMSE. All values are in centimeters (cm).

Aegean, the cyclone of the central Aegean and the front created by the Dardanelles outflow, the mid-Adriatic and south-Adriatic pit cyclones as well as the east and west Adriatic currents, the Atlantic Ionian Stream and the Atlantic Tunisian Current, the mid-Mediterranean Jet, the Lybio-Egyptian Current, the Asia Minor Current, the Rhodes Gyre, the East and West Black Sea gyres as well as the Sevastopol anti-cyclone, are all reproduced satisfactorily in terms of surface elevation. Although the ma-

jority of the jets, gyres and mesoscale features of the domain are properly reproduced by the simulation when compared to **AVISO** altimetry, with some inaccuracies in a few mostly transient mesoscale structures in the Levantine and southern-Ionian Seas (i.e., Western Cretan Cyclonic Gyre, Ierapetra Gyre, Shikmona Gyre, Mersa Matruh Gyre and Pelops Gyre). The comparison with altimetry shows deviations in regions of shallow continental shelves like the north-west Black Sea and the north Adriatic, as well as areas closer to coasts.

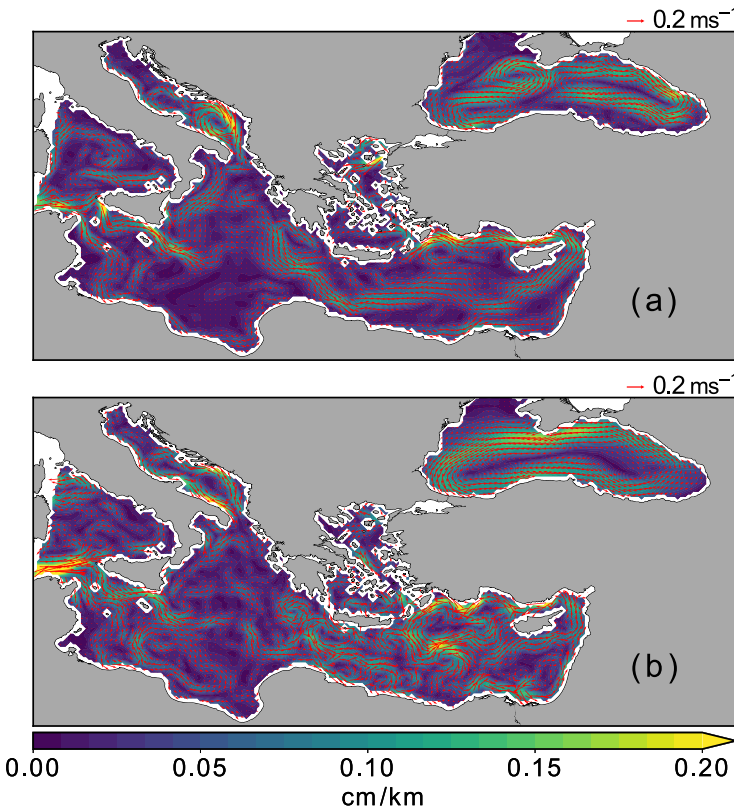


Figure 3.4: Horizontal gradient of surface elevation in  $\text{cm km}^{-1}$ , and barotropic component of geostrophic currents (red arrows), for the period 1985 – 2014. (a) **EMBS** simulation, and (b) **AVISO** satellite reanalysis.

The time-series of basin-averaged **ADT** and the deseasoned signal can be seen in Figure 3.5 for different sub-basins, and the associated metrics can be found in Table 3.2. The comparison reveals no significant disparities, with the mean value and the variability of sea surface being reproduced within acceptance levels by the simulation. The bias is lower than 1.1 cm for all basins, with **RMSE** being around 4.3 cm overall and 2.7 cm for the deseasoned signal, and Pearson's coefficient shows

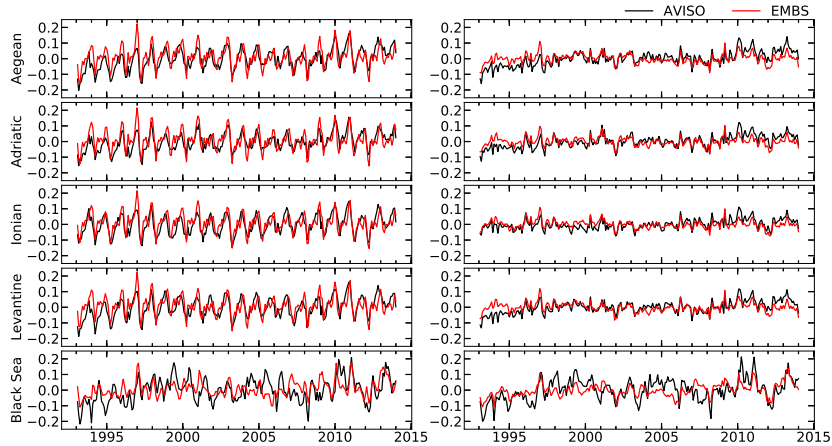


Figure 3.5: At the left column, time-series of spatially-averaged, zero-centered **ADT** in different sub-basins, for **AVISO** satellite reanalysis (black) and **EMBS** simulation (red). At the right column, as above with the seasonal cycle removed (deseasoned). All values in meters (m).

satisfactory correlation for all basins. The largest deviations appear in the Black Sea, where bias is around 0.9 cm, **RMSE** around 7 cm, and R coeff. around 0.5.

Table 3.2: Metrics of **ADT** (zero-centered) time-series comparison between **EMBS** simulation and **AVISO** satellite reanalysis data, for each sub-basin. Correlations are statistically significant for the whole domain ( $p$ -value  $< 0.01$ ).

<b>Basin</b>	<b>Bias (m)</b>		<b>RMSE (m)</b>		<b>Pearson's R</b>	
	<b>Seasonal</b>	<b>De-seasoned</b>	<b>Seasonal</b>	<b>De-seasoned</b>	<b>Seasonal</b>	<b>De-seasoned</b>
Aegean Sea	0.012	0.053	0.035	0.692	0.652	
Adriatic Sea	0.012	0.049	0.031	0.702	0.641	
Ionian Sea	0.012	0.048	0.026	0.722	0.636	
Levantine Sea	0.012	0.052	0.032	0.680	0.616	
Black Sea	0.009	0.069	0.057	0.494	0.590	
<b>Overall</b>	<b>0.011</b>	<b>0.043</b>	<b>0.027</b>	<b>0.690</b>	<b>0.701</b>	

### 3.1.3 Water exchange - properties at the straits

The straits of Bosphorus and Dardanelles constitute points of control on the flow, as discussed in Section 2.2.2. In order to estimate the

proximity of the flow regime to the hydraulic control limit, composite Froude numbers in the two straits (equivalent to the two-layer hydraulic solution), are calculated from the EMBS output and presented in Figures 3.6 and 3.7.

In Bosphorus, the mean composite Froude numbers remain subcritical ( $\sim 0.15$ ) for most part of the strait, with the highest mean values ( $\sim 0.85$ ) appearing towards the southern end of the strait (around Bosphorus sill, point B2 in Fig. 3.6a). Similarly, the percentage of days where the flow is hydraulically controlled is close to zero for the largest part of the strait, and reaches  $\sim 10\% - 25\%$  around the sill (Fig. 3.6b). The southern Bosphorus sill represents an additional vertical constriction which is added to the already horizontally constricted flow, pushing the flow to the hydraulic control limit on a seasonal basis as shown by the temporal evolution of composite Froude number (Fig. 3.6c). The location of seasonal maxima at the beginning of the year (around spring) coincides with the expected larger flow rates in the upper layer (i.e. velocities) due to increased fresh water outflow in the Black Sea at the same time.

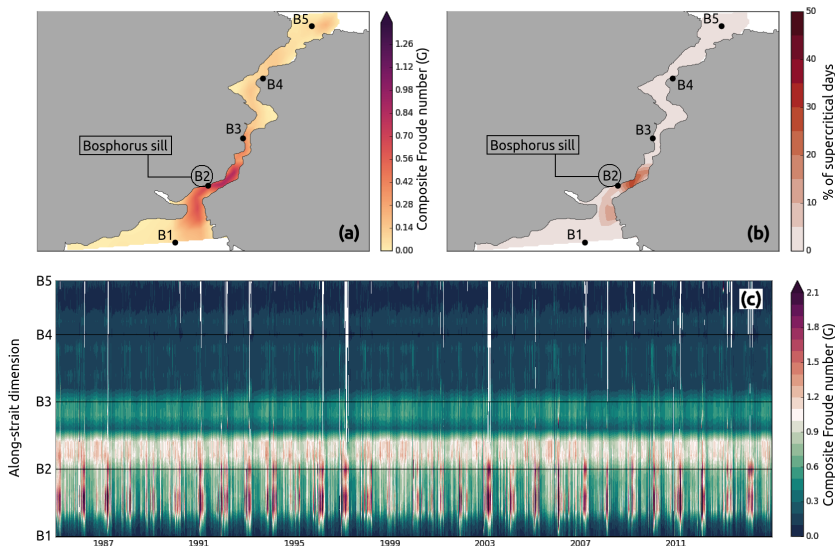


Figure 3.6: (a) Mean composite Froude number distribution in the Bosphorus strait, for the 1985–2015 period. (b) Percentage of days with supercritical flow ( $G^2 > 1$ ) for the same period. (c) Timeseries of composite Froude number, as calculated along the midsection of the strait. Horizontal lines correspond to the position of black dots in (a) and (b). Point B2 corresponds to the southern Bosphorus sill.

In Dardanelles, mean composite Froude numbers appear somewhat larger than in Bosphorus strait. For most part of the strait (i.e. the part north of Nara passage), mean composite Froude numbers range around

0.15, with no supercritical values appearing. However, especially at Nara passage but also further south until the exit to the Aegean, the flow is subjected to hydraulic control with mean Froude numbers close to 1, while more than 10% of days exceed critical levels reaching 70% at the Nara passage (Fig. 3.7a,b). The temporal evolution also reflects this behaviour and appears to do so on a seasonal manner as in Bosphorus, nevertheless, the difference is that the values are much higher and the maxima appear in mid to late summer. This is most probably due to the increased flow rates in the upper layer, caused by the seasonal atmospheric forcing in the form of wind stress by the Etesians, which have a prevailing NNE direction during that time of the year (i.e. in the direction of the strait towards the Aegean Sea).

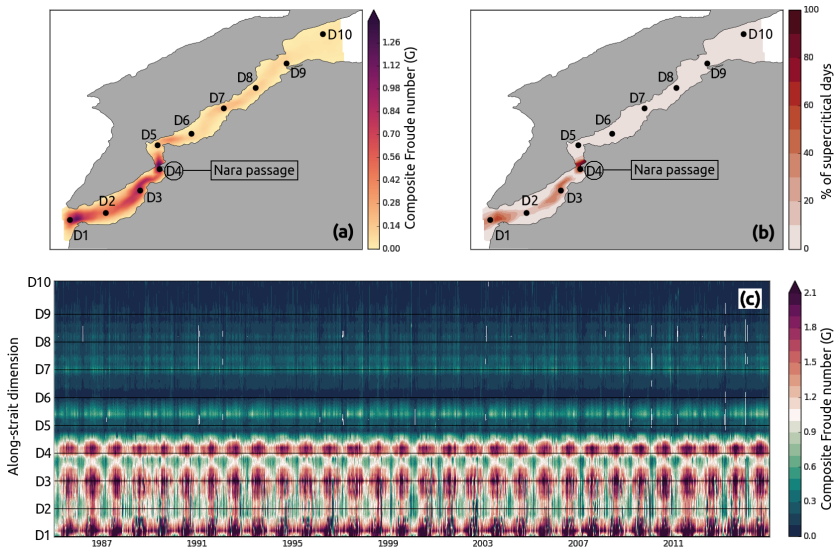


Figure 3.7: As in Fig. 3.6, for the Dardanelles strait. Point D4 corresponds to the Nara passage.

The above seasonal behaviour of both straits which coincides with the aforementioned mechanisms, suggests that criticality of the flow in both straits appears to be controlled by the upper layer flow, either through a relative increase in upper-layer velocity, a relative decrease in upper-layer thickness, or both (following Eq. 2.3). This can be seen in more detail when examining the seasonal along-strait cross sections (further down in this Section).

The volumetric water exchanges at the two narrow straits of Bosphorus and Dardanelles, as calculated by Maderich et al.'s chain-model, is reproduced by the EMBS simulation (Figure 3.8). A much higher variability is demonstrated by the simulation, while the upper limit of volume exchange is increased (for the upper as well as the lower layers).

Both these changes seem to be improving the calculated flow rates when compared to hydrographic observations at Dardanelles, especially for the upper layer. The spread of both upper and lower layer flows in comparison to the net flow is simulated to be larger in the Dardanelles than in the Bosphorus strait. This difference in the behavior of the two straits is also seen in the chain-model of Maderich, as well as in the observations (see Maderich et al., 2015). Time series of the net flow (Figure 3.9), and the corresponding metrics (Table 3.3), show that while upper layer flow rates are much higher in the EMBS simulation than in the Maderich et al. chain-model (in accordance with observations), the lower layer flow rates are of comparable or slightly lower magnitude, which results in net flow rates being higher overall in EMBS. For the period 2008–2009, this higher upper layer flows as well as the higher variability is an overall improvement when compared to the chain model. Figure 3.9b shows, as a closeup of Figure 3.9a, that the variability of the daily net volumetric exchange in the simulation is very similar to that calculated by observations at Dardanelles strait during 2008–2009, while for the chain model the variability of the same quantity is lower, as exhibited by the much smoother time-series.

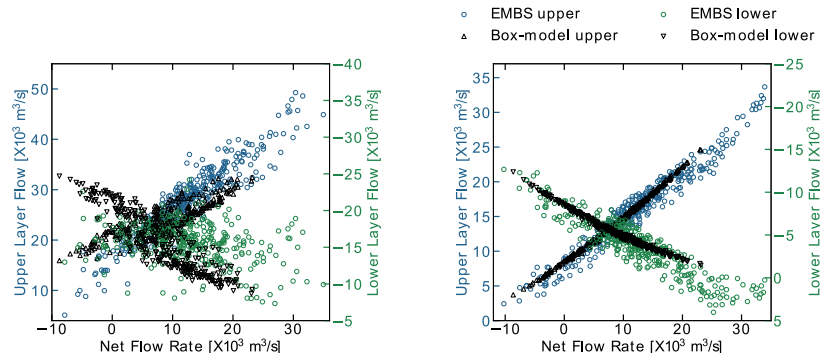


Figure 3.8: Volumetric water exchange at Dardanelles (**left**) and Bosphorus (**right**), for the two-layers flow. The upper and lower layer flows (y-axes) are compared to the net exchange (x-axes). Results of **EMBS** simulation are shown with circles, while results from the model of Maderich et al. described in Section 2.2.1, are shown with triangles, for the whole period in monthly-averaged values.

The simulated seasonal evolution of water characteristics along the Bosphorus Marmara Dardanelles (**BMD**) system, is compared to known patterns from published observational campaigns (Beşiktepe, 2003; Beşiktepe et al., 1994). The simulated temperature and salinity fields exhibit exceptional agreement with the observed fields, and features like the cold surface waters of Black Sea origin during winter (Figure 3.10a), the cold tongue between 10–30 m depth during spring (Figure 3.10b), the

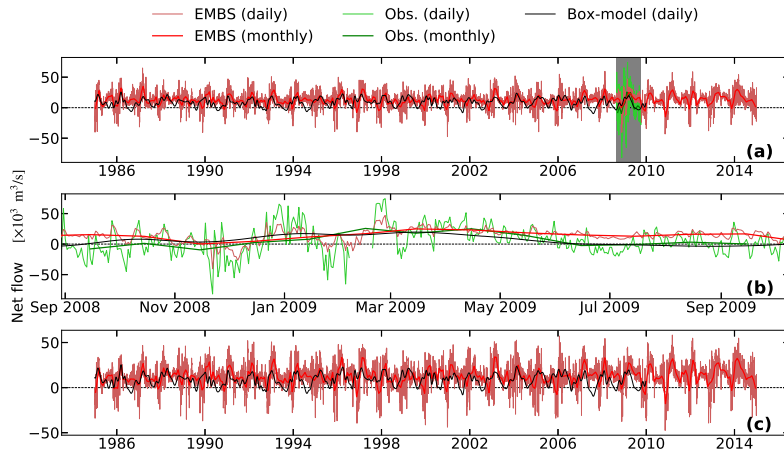


Figure 3.9: Time-series of net volumetric flow: **(a)** at Dardanelles, **(b)** at Dardanelles for the period denoted with the gray box, and **(c)** at Bosphorus. Comparison between the EMBS simulation, the model of Maderich et al., and 1-year-long observations at Dardanelles strait from Jarosz et al. described in Section 2.2.1, using daily values and monthly averages.

relatively warmer deep waters of Aegean Sea origin during summer and autumn (Figure 3.10c,d) and the overall doming around spots of abrupt changes in bathymetry (internal lee waves), are accurately reproduced.

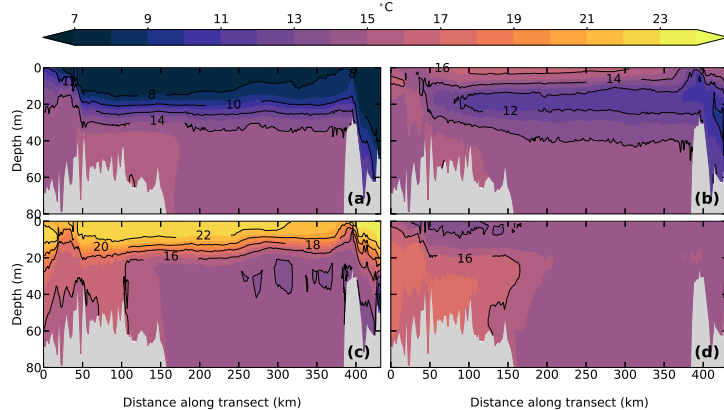


Figure 3.10: Seasonally-averaged vertical cross section of potential temperature, along a transect in the Dardanelles–Marmara Sea–Bosphorus line. Horizontal axis spanning from the Dardanelles exit at the Aegean to the Bosphorus exit at the Black Sea. **(a)** Winter JFM, **(b)** spring AMJ, **(c)** summer JAS, and **(d)** autumn OND. Nara passage in the Dardanelles is located around the 50 km mark, and the southern Bosphorus sill at the 400km mark.

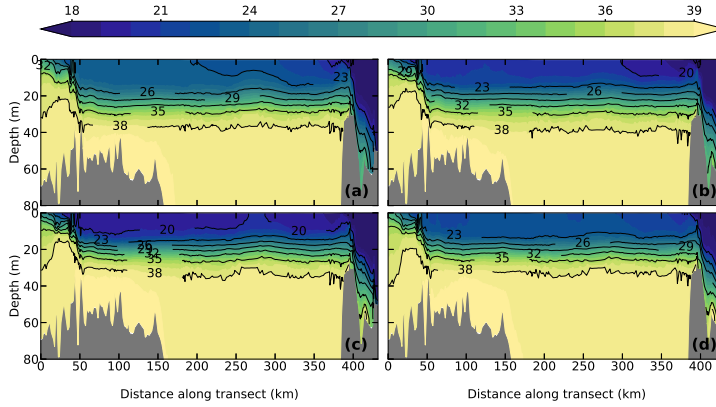


Figure 3.11: Same as in Figure 3.10, for salinity. (a) Winter JFM, (b) spring AMJ, (c) summer JAS, and (d) autumn OND.

The salinity field remains vertically stratified throughout the year, with low surface values of Black Sea origin and high near-bed values of Aegean origin reflecting the known circulation pattern of water exchange between the two Seas (Figure 3.11).

Table 3.3: Average two-layer (upper/lower) and net volumetric flow and standard deviation of flow at the Dardanelles and Bosphorus straits for the EMBS simulation and the box-model of Maderich et al. Comparison for the common period is first shown, while the additional comparison with observations at Dardanelles from Jarosz et al. is included for the period 2008–2009. Positive (negative) values denote direction towards the Aegean Sea (Black Sea).

(all flows in $\times 10^3 \text{ m}^3 \text{s}^{-1}$ )		EMBS Simulation		Box-Model		Observations	
Period	Location/Layer	Mean	StD	Mean	StD	Mean	StD
<b>1985–2009</b>	Bosp. Upper	+15.7	+9.4	+13.9	+4.5	—	—
	Bosp. Lower	-4.0	-4.6	-5.6	-2.3	—	—
	Bosp. Net	+11.8	+12.1	+8.4	+6.8	—	—
<b>2008–2009</b>	Dard. Upper	+27.6	+13.7	+23.9	+3.6	—	—
	Dard. Lower	-15.6	-5.8	-15.7	-4.1	—	—
	Dard. Net	+12.0	+11.2	+8.3	+6.8	—	—
	Dard. Upper	+29.4	+12.2	+23.2	+3.5	+37.8	+16.4
	Dard. Lower	-15.1	-5.3	-16.6	-4.6	-32.8	-13.4
	Dard. Net	+14.4	+10.7	+6.6	+7.7	+5.0	+23.2

As described in Baines, 1995 for the case of a two-layer flow over a sill, if the flow over it is strong enough to create controlled flow at and right past the sill ( $G^2 \geq 1$ ) then the adjustment of supercritical flow on that side, transitioning to a sub-critical further away from the sill, happens with a dissipative jump. In this simulation, the hydrostatic approximation prevents such sudden vertical jumps, however due to the terrain-following  $\sigma$ -layers, flow can still occur in the bottom layers over relatively smooth undulating topography, and the otherwise expected abrupt hydraulic jump manifests itself in this case as an internal lee wave right after passing the sill. This can be seen especially pronounced in the Temperature cross-sections (but also in Salinity), right after the upper layer flow passes south Bosphorus and Nara passage sills.

### 3.1.4 General Circulation

The simulated mean 1985–2014 current velocity is provided here, averaged over three different vertical layers of the water column (using layer width as the weighing factor), which in combination with meridional and zonal overturning streamfunctions throughout the domain, can provide useful insight regarding the general circulation, as well as the thermohaline circulation of the eastern Mediterranean and Black Sea system, as modeled in the EMBS simulation. The vertical extents of the three layers over which currents have been averaged—namely the surface layer (0–50 m), intermediate layer (50–400 m) and deep layer (400 m–max. depth) shown in Figure 3.12—were selected using the overturning streamfunctions as a guide for distinguishing between different water mass movements in the vertical (Figure 3.13).

The zonal overturning streamfunction for the whole eastern- Mediterranean, excluding the Black Sea, is shown in Figure 3.13a. The eastward moving west-Mediterranean waters of Atlantic origin (reaching 1.2 Sv in the top 120 m) are clearly visible in the clockwise rotating surface layer, reaching as far as the Levantine basin and the eastern parts of the Mediterranean. The contribution of the Adriatic dense waters (and potentially that of dense waters originating in the Aegean Sea) is pronounced in the area between 20° E–25° E, introducing a convection pattern which stretches down to the bottom of the basin (~22° E). Eastern Mediterranean Deep Waters (EMDW) of relatively high density ( $\sigma_0 \approx 29.3$ ) are found near the bottom around that area. The anti-clockwise circulation cell at 1000 m and deeper (blue section roughly between 10 E and 22 E in Figure 3.13a) is transporting these EMDW further east as can be seen also in the density field at the bottom layers, while transporting Levantine Intermediate Waters (LIW) between 400–1000 m westward over the Sicily strait and into the western-Mediterranean.

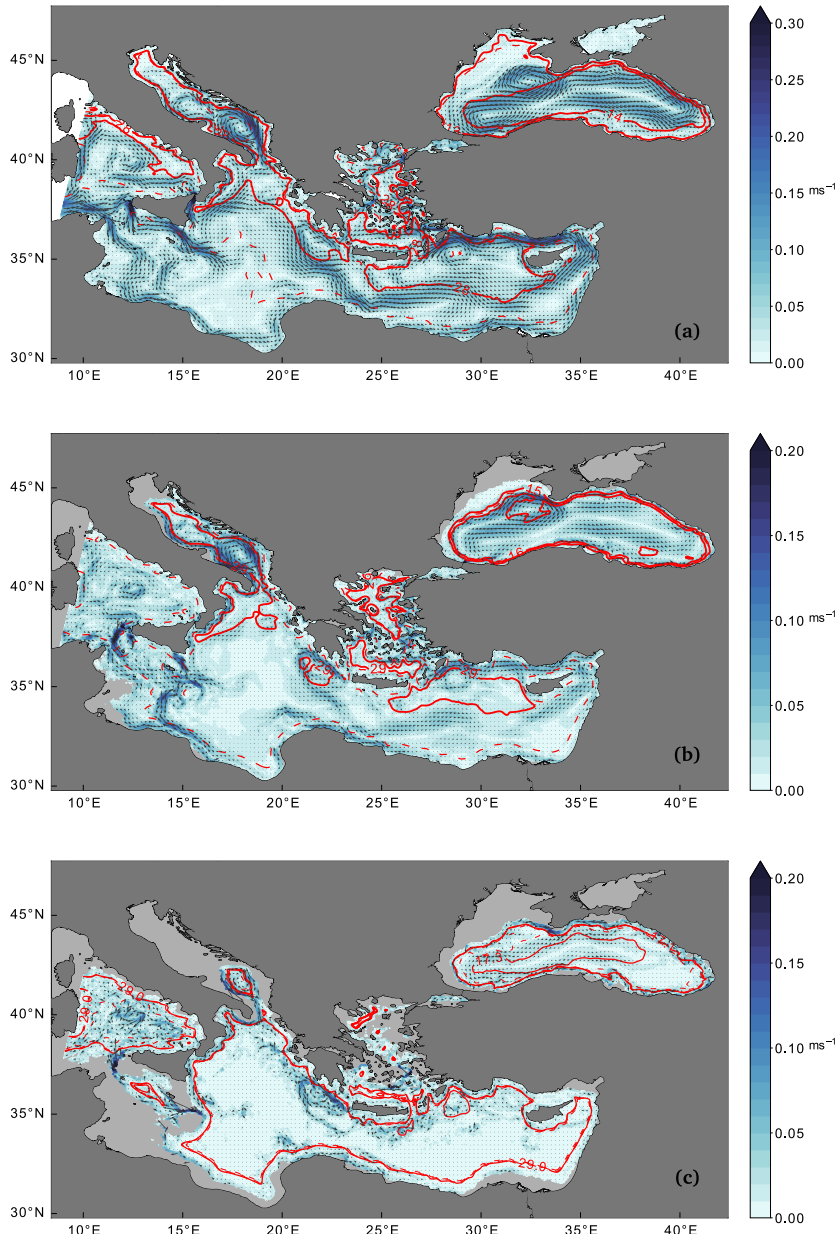


Figure 3.12: Currents and potential density for the period 1985–2014, vertically weight-averaged between (a) 0–50 m, (b) 50–400 m and (c) 400 m to maximum depth. Potential density is indicated with red contour lines. In (a,b), increments of  $1 \text{ kg m}^{-3}$  are used for solid lines, and  $0.5 \text{ kg m}^{-3}$  for dashed lines, while in (c),  $0.2 \text{ kg m}^{-3}$  for solid lines, and  $0.05 \text{ kg m}^{-3}$  for dashed lines.

In the horizontal field, “pools” of increased density extend horizontally from south of the Otranto strait, following the Ionian coast of Greece, to South Crete and then filling the whole southern-Ionian basin (Figure 3.12). At deeper layers, one can locate the LIW formation site in the north-Levantine between Cyprus and southeast of Crete (Figure 3.12b), and the EMDW transported eastward around the Rhodes gyre and southeast of Crete (Figure 3.12c), both of which agree with the known general and thermohaline circulation in the eastern-Mediterranean. In the deep circulation field, increased westward velocities are observed along the bottleneck created by the Sicily straits, transporting LIW to the western Mediterranean (Figure 3.12b,c). Overall, the highest densities are found in the deep Adriatic (north and south pits  $\sim 43^\circ$  N and  $42^\circ$  N in Figure 3.13b), most of the deep Aegean (Lemnos, Athos, Skyros and Cretan basins, Figures 3.12c and 3.13c), and the deep parts of the southern domain (south Ionian, Levantine seas), while the lowest densities are found in the surface waters over the northwest Black Sea shelf.

Following the meridional overturning streamfunction along the north-Ionian and Adriatic Seas (Figure 3.13b), a northward circulation of 0.1 to 0.4 Sv can be found in the surface to sub-surface layers up to the position of the south and north Adriatic pits ( $\sim 42^\circ$  N and  $\sim 43^\circ$  N respectively), where downward motion is observed and a subsequent doming of the isopycnals, with a returning benthic circulation of high density deep waters ( $29.2 < \sigma_0 < 29.4$ ) overflowing back into the south Mediterranean Sea following the bathymetry in a catabatic-wind-like fashion. At the surface and within the first  $\sim 50$  m, a southward moving circulation is observed at the northern-most part of the Adriatic, which corresponds to the contribution of riverine waters from Po river forming the west Adriatic current. A very similar picture can be seen in the meridional overturning streamfunction along the Aegean Sea (Figure 3.13c), with a northward circulation of comparable magnitude (0.1–0.4 Sv) and Levantine origin flowing into the Aegean through the Karpathos strait ( $\sim 35^\circ$  N,  $27^\circ$  E Figure 3.12a), flowing up to about  $38.5^\circ$  N– $40^\circ$  N, where downward motion contributes to dense water forming at the benthic layers, displaying some of the highest observed water densities of the whole domain ( $\sigma_0 \approx 29.5$ ). This northward moving surface circulation becomes sub-surface around  $38^\circ$  N– $38.5^\circ$  N, under a southward moving surface circulation of North Aegean waters mixed with waters of Black Sea origin (seen as an anti-clockwise surface cell, stretching roughly from  $37.5^\circ$  N to  $40^\circ$  N – Figure 3.13c). The benthic southward-moving circulation still exists, but is very reduced when compared to the north-Ionian/Adriatic case, due to the protruding bathymetry of the Aegean, which constrains the southward movement of high density benthic waters; this is consistent with the high densities observed at relatively shallow waters in the north and south Aegean ( $\sigma_0 \approx 29.3$ – $29.4$  at 500 m depth).

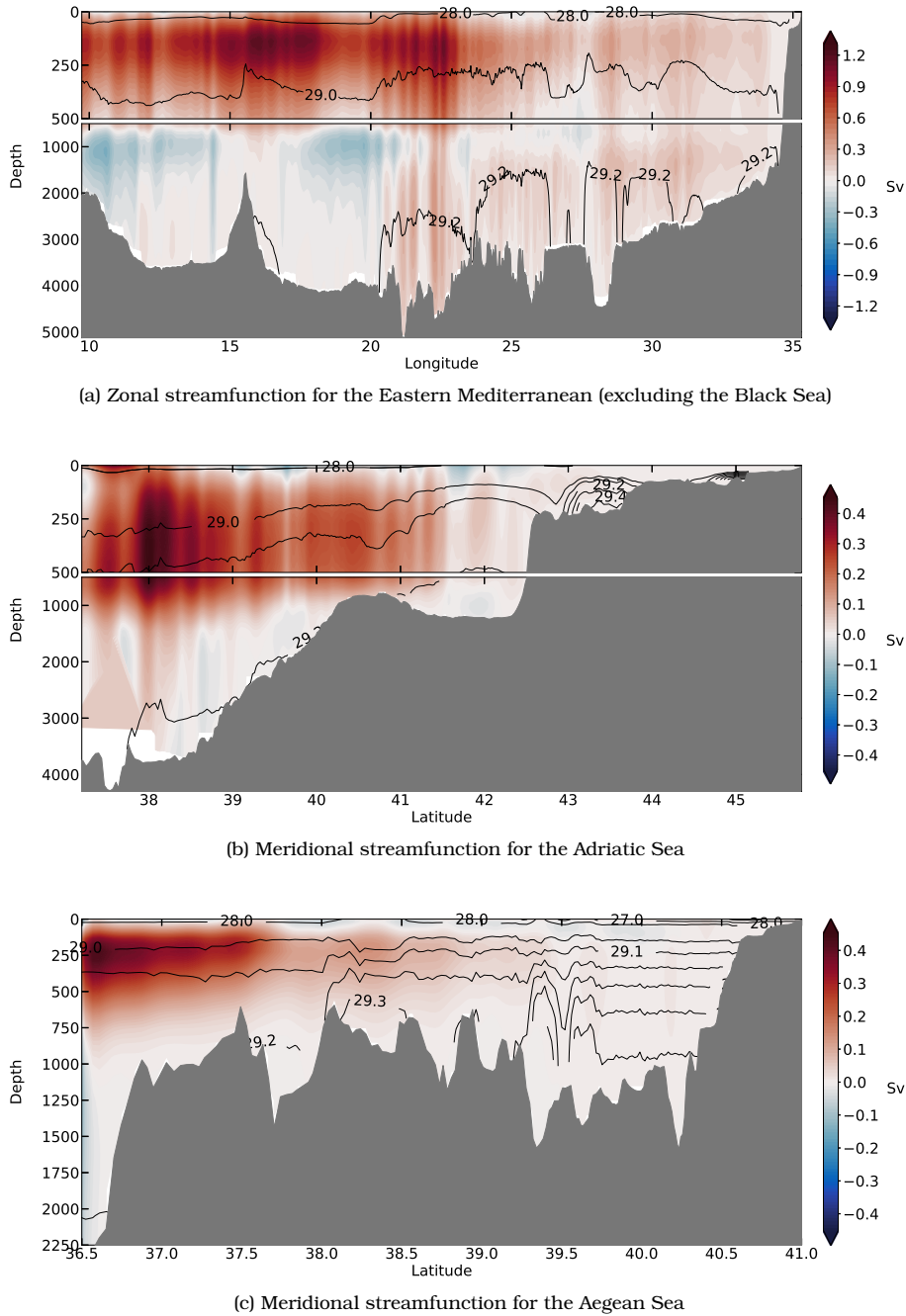


Figure 3.13: Zonal and meridional overturning streamfunctions for the period 1985–2014. Black contours indicate potential density along the midsection of the domain, which is depicted with dashed lines in Figure 2.1.

### 3.1.5 Column Structure - Profiles

In this part of the validation process, the vertical structure of the water column is compared to observations and state-of-the-art modeling systems. The comparison shows good agreement with observations, and the variability is reproduced accurately overall. In general, the **EMBS** simulation overestimates both salinity and temperature systematically over the whole column almost everywhere, nevertheless biases and **RMSEs** remain fairly low, with a very high correlation coefficient. While the **MFS** simulation (which makes use of these observations among others, as inputs for its assimilation scheme) reproduces the observations better than the **EMBS** simulation, the differences are very small. Moreover, in the area of immediate interest for this study (i.e., the north Aegean Sea), the performance of the **EMBS** simulation is comparable to the **MFS** operational forecasting system, especially reproducing vertical structures of the water column and density ranges (Figure 3.14). As can be seen in the figure, salinity in the north Aegean has a bias of 0.12 and an **RMSE** of 0.253, and potential temperature has a bias of 0.32 °C and an **RMSE** of 0.62 °C. Potential density has a bias of 0.017, and an **RMSE** of 0.169,

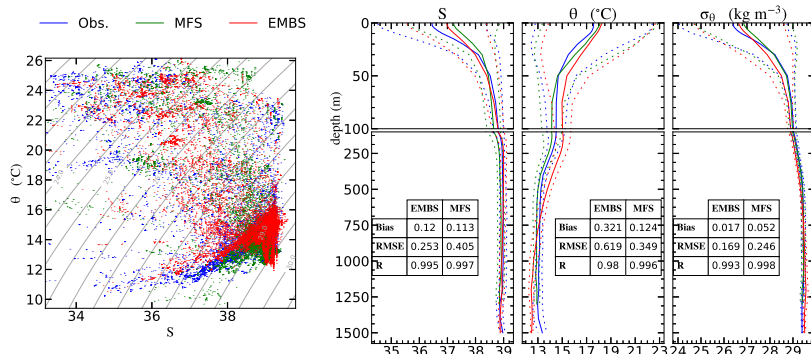


Figure 3.14: North Aegean Sea  $\theta/S$  diagram containing all profiles (casts) for the period 1985–2014, and average vertical profiles of  $S$ ,  $\theta$  and  $\sigma_\theta$  in the North Aegean Sea. Observations (blue), **MFS** simulation (green) and **EMBS** simulation (red) both calculated using profiles at the same place and time as the observations. The range of one standard deviation is shown with dashed lines as a measure of overall variability. Additional metrics for the averaged profiles (Bias, **RMSE** and R-coefficient) are shown for the two simulations compared to observations, with all correlations being statistically significant ( $p$ -value  $< 0.01$ ).

while the improvement is even higher at the surface layers for all fields. Apart from the mean profiles, points from all the individual profiles in the entire set can be seen in the  $\theta/S$  diagram, which shows

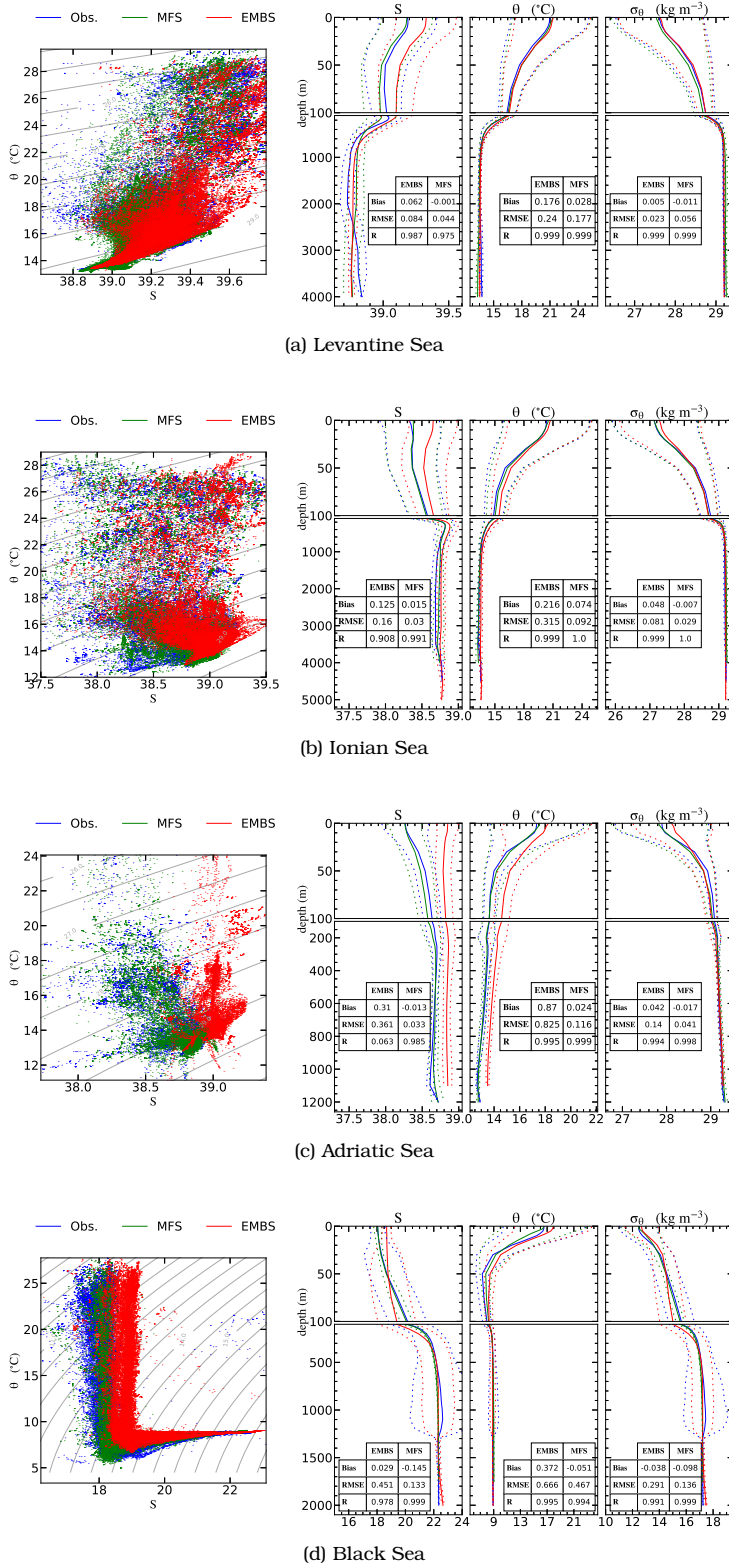


Figure 3.15: Same as in Figure 3.14, for different basins.

a satisfactory reproduction of the water characteristics of the area in a three-dimensional sense.

A similar profile comparison for different sub-basins can be seen in Figure 3.15, which demonstrates the spatio-temporal performance of the EMBS simulation (metrics are included as tables within the graphs, with all correlations being statistically significant). The Levantine basin (Figure 3.15a) is reproduced quite accurately, with surface salinity values being higher due to increased evaporation, and bias and RMSE remaining exceptionally low over all fields. The Ionian Sea (Figure 3.15b) shows a similar picture; the LIW are clearly visible at  $\sim$ 100–400 m, and simulation performance remains very high. In the Adriatic, the bias and RMSE especially for potential temperature are among the highest found overall (Figure 3.15c), the bias at the surface for potential density is around 0.2, but gets much closer to observations when moving downwards into the column, which indicates that the density driven circulation should not be heavily affected. The MFS simulation performs at its best in this sub-basin. In the Black Sea (Figure 3.15d), again, the performance is acceptable, with most deviations appearing at the surface, especially for the salinity field. It is noteworthy that the EMBS surface salinity at both the Adriatic and the Black Seas exhibit a positive bias, possibly attributed to the omission of minor rivers and thus a potential underestimation of the riverine input in the basins. Despite the presence of bias in the simulated fields, the  $\partial/S$  diagram and the vertical profiles of the hydrographic properties reveal a very good reproduction of the distribution of water masses throughout the basin, thus a faithful simulation of the overturning circulation and the production of intermediate and deep waters.

### 3.1.6 Dense Water Formation

As described in Section 1.1, several mechanisms can be directly or indirectly connected to the formation of dense water in the Aegean Sea and the Eastern Mediterranean in general. Some of the most important ones, namely heat, fresh-water and buoyancy fluxes and import, act along the air-sea interface or in areas of water inflow, and are further investigated in Section 3.2. In this section, only the reproduction and evolution of dense water formation events in the Aegean Sea is examined, in an effort to extend the validation process further into mechanisms that affect the whole water column. In addition, a reported precursor of such events that has been suggested in literature (i.e. increased salinity in the Marmara Sea) is shortly investigated, again in an effort to assess whether the model can reproduce such observations.

In order to investigate the capacity of the EMBS simulation to reproduce the interannual variability of processes like dense-water formation and mixing during stagnation periods, the interannual variability of

simulated density in one of the deep North Aegean sub-basins, northern Skyros basin, is presented in Figure 3.16. The isopycnal rise during 1987 – 1994, the subsequent gradual relaxation and deepening during the stagnation period (1994 – 2000), the following steady-state period until about 2006 and the more recent minor formation episodes are reproduced, as reported by several studies (e.g., Gertman et al., 2006; Kassis and Korres, 2021; Zervakis et al., 2000). The interannual vari-

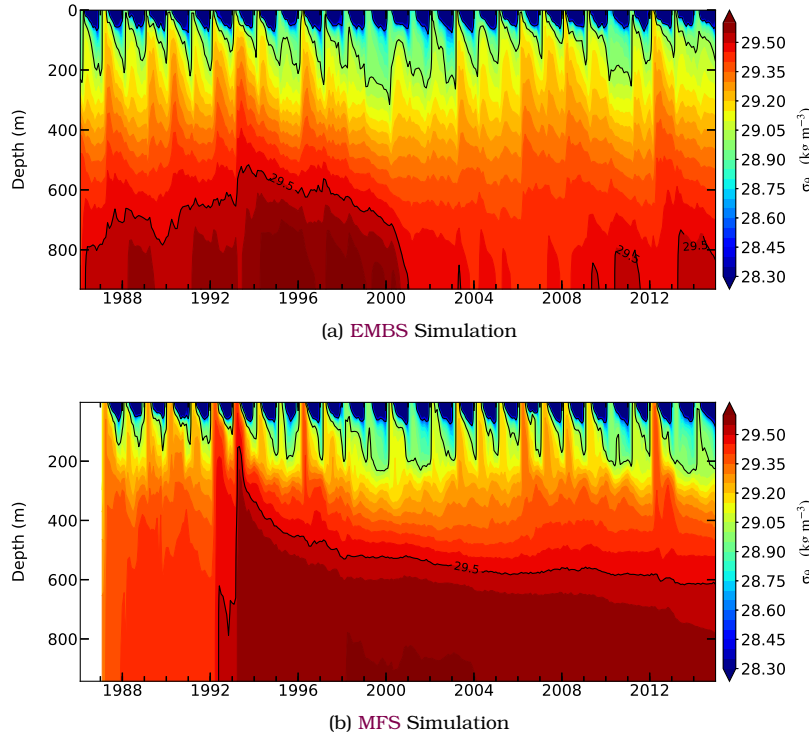


Figure 3.16: Hovmöller diagrams of potential density with depth for the 1987 – 2014 period at Skyros basin, central-north Aegean Sea ( $\sim 39^\circ \text{ N}, 25^\circ \text{ E}$ ), as simulated by the two modeling systems (EMBS and MFS). Color-scale contours have a spacing of  $0.05 \text{ kg m}^{-3}$ , while black contours are shown every  $0.5 \text{ kg m}^{-3}$ .

ability of the seasonal cycle of the surface and upper-layers, which can be attributed in large to winter-time cooling at the surface as well as dense water formation due to shelf convection/cascading, is also visible. In the same figure, a comparison with assimilated model results, shows distinct differences in the reproduction of the water-column density evolution at Skyros basin by the MFS simulation. The density field of the uppermost  $\sim 200$  meters of the domain, seems to be reproduced similarly by the two simulations (with the EMBS surface seasonal cycle reaching relatively deeper). However, the variability of the density in

deeper layers (i.e. bellow 300 meters depth) is drastically reduced in the MFS simulation, with almost multi-decade-long stagnation periods in several cases, which is not supported by the observation studies mentioned above. Moreover, the intensity of formation events seems to be reduced compared to the EMBS simulation (as showcased by the stripes of dense water spanning the whole water column during formation episodes). Because of the geometry of the basin, dense stagnant waters at its deepest parts can be removed either through ventilation due to vertical mixing, or through displacement by even denser waters (e.g. Zervakis et al., 2000). The semi-stagnant behaviour of the MFS simulation is in contrast with the more varying density of the EMBS simulation field, probably pointing to a more realistic vertical mixing and advection parameterization in the EMBS case.

High salinity values have been observed in a past study, at the surface waters of the Marmara Sea (Beşiktepe et al., 1994), immediately preceding major dense water formation events (like the one of 1987) in the Aegean Sea. In Figure 3.17, the average salinity of the upper 10 meters is calculated in daily values for the western part of Marmara Sea (adjacent to Dardanelles strait). The simulated values and variability of surface salinity closely follow the ones described and presented in (Beşiktepe et al., 1994), while the pattern and shape of the time-series is resembling the observed ones (although temporal coverage is relatively restricted in that study). Abrupt spikes of positive salinity anomaly are observed in the results of the EMBS simulation, especially in the individual grid-cells time-series at several instances, usually around late winter (e.g. in 1987, 1996, 1999, 2000, 2007, 2010). In some cases these anomalies appear within years known for dense water formation in the Aegean, as suggested by literature. It is worth noting that during the stagnation period (~ 1996-2000, see also Fig. 3.16) the salinity anomaly in Marmara Sea is not exceeding 1 salinity unit for the whole period. Although it is not suggested here (neither from observations nor from theory) that dense water formation in the Aegean Sea can be connected in a causal sense to salinity anomalies in the Marmara Sea alone, it is presented here to support the validation process, but also as a hypothesis for a possible contributing factor or precursor to dense water formation events.

### 3.2 AIR-SEA INTERACTIONS

In this section, the air-sea fluxes (for heat, water and buoyancy) are examined for the Aegean Sea, and are shortly compared to the ones in adjacent basins of the Eastern Mediterranean, highlighting differences and similarities. The climatic seasonal and interannual variability of these fluxes, as represented through the combination of terms in buoyancy flux determination, is then examined through Principal Component

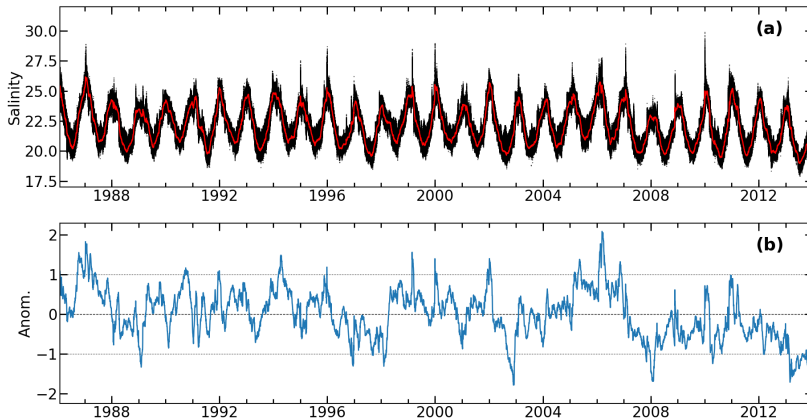


Figure 3.17: Time-series of daily surface salinity (upper 10 meters) in the western Marmara Sea. (a) Individual grid cells (**black**), and spatially averaged over the whole area (**red**). (b) Salinity anomaly of spatial averages (**blue**).

Analysis. The individual sub-basins mentioned here, are again as defined in Figure 2.1.

### 3.2.1 Heat Fluxes

Air-sea heat fluxes are calculated within the simulation as described in Section 2.2.3. The direction of heat fluxes is established relative to the ocean reference frame, and is considered positive towards the ocean (ocean warming) and negative towards the atmosphere (ocean cooling). In Figure 3.18, the simulated Net Heat Flux as described in Equation 2.4, is presented averaged for the Eastern Mediterranean over the period 1985–2015. The Aegean and the Adriatic Seas experience heat loss throughout the year, constituting regions where convective processes take place. Heat loss at the surface in climatological scales, constitutes one of the main factors for potential dense water formation processes. Despite the fact that Adriatic Sea has been recorded as the major source of EMDWs, mean heat loss in the Aegean Sea is simulated to be larger overall than that in the Adriatic. Coastal bands in Northern Africa and Southern Anatolia are also simulated to demonstrate high heat losses. This has been reported again in similar studies (Sevault et al., 2014), and was attributed to excessive latent heat loss during conditions of dry continental-winds blowing over these coastal regions.

A decomposition of the net heat flux into its components (Eq 2.4), is presented in Figure 3.19. As expected, the overall variation of the shortwave radiation follows the latitudinal gradient, so that the heat

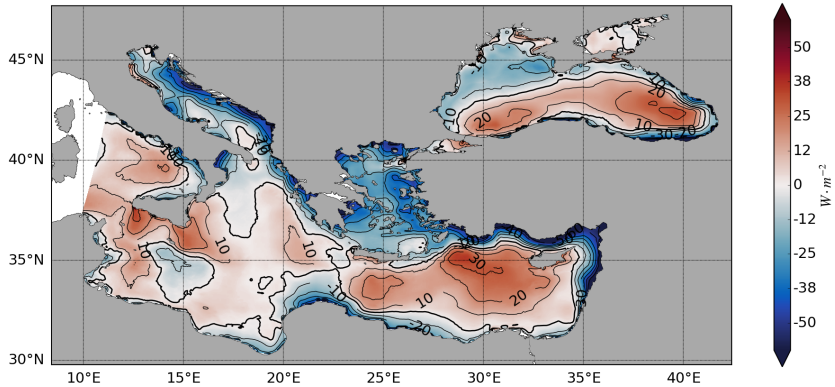


Figure 3.18: Mean heat flux over the eastern Mediterranean and the Black Seas over the 1985–2015 period. The negative sign signifies heat loss, positive signifies heat gain by the sea.

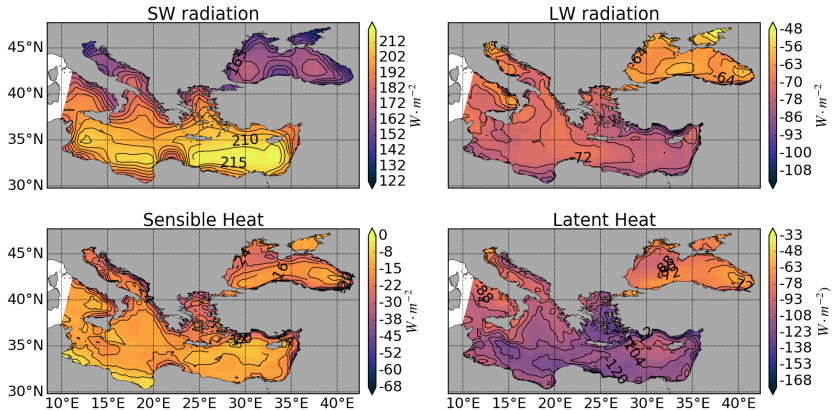


Figure 3.19: Mean heat-flux components over the Eastern Mediterranean and Black Seas over the 1985–2015 period.

input over the Southern part of the domain is higher compared to the Northern part. A similar gradient is observed in the losses due to long-wave and latent heat fluxes, which can be primarily attributed to the higher temperatures and evaporative fluxes in the southern part of the domain. However, the gradient is not as coherent or as pronounced as in the short-wave case. When comparing the Aegean and the Adriatic basins' heat flux balance, the excessive short-wave heat input in the Aegean is compensated by the remarkably stronger evaporative losses and higher long-wave net radiation of the Adriatic, resulting in comparable net heat fluxes. Sensible heat loss also plays a secondary, though important role, with relatively higher values in the Aegean.

The seasonal cycle of the four heat-flux components, along with the net heat flux, corresponding to the 30-year average over the Aegean

Sea is presented in Figure 3.20. Evaporative losses are the strongest among the contributors of heat-loss for most of the year, with high values during late summer and autumn. There is a noteworthy sign reversal in the sensible heat flux during summer months, indicating warmer atmosphere over cooler ocean. Long-wave radiation remains relatively stable throughout the seasonal cycle.

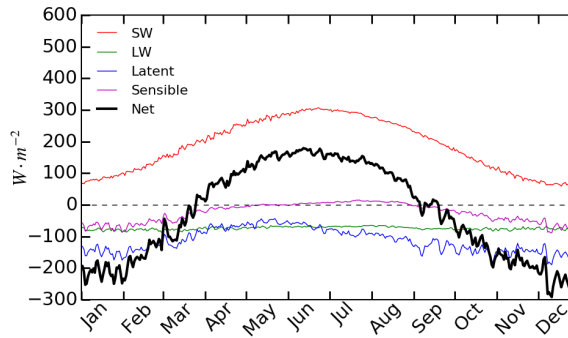


Figure 3.20: Seasonal cycle of the four heat-flux components over the Aegean Sea, in daily values for the 1985–2015 period.

The climatological mean heat-flux components (Fig. 3.19), as well as the total heat flux over five basins shown in Figure 2.1, along with the corresponding standard deviations, are presented in Table 3.4. The Levantine and Black Seas are weak importers of heat from the atmosphere, while the Ionian a weak exporter. More impressive is the large heat loss from the Aegean Sea, much higher than the mean Adriatic value. Therefore, the estimated overall heat exchange of the Eastern Mediterranean with the atmosphere is a loss, mainly due to the intense losses of the smaller, northern sub-basins, the Adriatic and the Aegean Seas.

Table 3.4: Climatological means and standard deviations of the various heat-flux components over the Eastern Mediterranean and Black Seas.

Basin	Shortwave		Longwave		Latent		Sensible		Net	
	Mean	StD	Mean	StD	Mean	StD	Mean	StD	Mean	StD
Aegean Sea	186.5	2.4	-74.7	2.2	-113.6	6.3	-26.1	4.6	-28	11.8
Adriatic Sea	167.6	2.9	-71.5	2.4	-91.5	4.5	-24.2	2.6	-19.6	7.4
Ionian Sea	195.0	1.8	-73.4	1.6	-106.8	3.5	-16.4	2.0	-1.7	5.6
Levantine Sea	208.9	1.6	-78.6	1.4	-112.8	4.5	-15.5	2.5	2.0	7.3
Black Sea	163.3	2.8	-63.7	2.1	-77.7	3.1	-20.9	2.5	1.0	5.5

As expected, latent heat flux is responsible for the highest heat loss in all basins, though significantly higher in the Aegean (by more than

$20 \text{ W m}^{-2}$ ) compared to the Adriatic. An additional feature is the much higher standard deviation of latent and sensible heat flux characterizing the Aegean Sea in comparison to the other basins, a fact possibly corresponding to the effect of the Etesian winds in summer, in combination with the resulting low surface temperatures due to coastal upwelling.

### 3.2.2 Fresh-water Fluxes

Fresh-water fluxes are calculated in equivalent meters per year change in the water surface, and the mean for the Aegean Sea over the 30-year period is presented in Figure 3.21. The whole basin's fluxes are dominated by evaporation (over precipitation), with relatively lower spatial variability in the southern part of the basin. Increased spatial variability appears in the northern and eastern parts of the basin, with small-scale features where  $E - P$  values are lower (a) due to higher precipitation along the coastal areas and (b) due to the presence of the cooler Black Sea waters which reduce the evaporation in the north Aegean's surface, and circulate in a cyclonic fashion (top panels in Fig. 3.21).

The seasonal cycle of fresh-water flux components, along with the net fresh-water flux, corresponding to the 30-year average over four basins is presented in Figure 3.22. Evaporative fluxes become stronger in the Aegean basin starting from late summer, remaining high during fall and winter, and reduce during spring. Precipitation is lowest during the summer months as expected, with highest values during late-autumn and winter months.

### 3.2.3 Buoyancy Fluxes

The 30-year climatological mean of the thermal component of the surface buoyancy flux is presented in Figure 3.23 (left panel). The strong net heat losses over the Aegean Sea drive the thermal component to a buoyancy loss over most of the region, and the only region where the sea exhibits a strong net heat gain from the atmosphere is the region in the Northeast Aegean neighboring the Dardanelles exit, and a weaker warming in the South Aegean Sea near the Cretan Straits. The spatial distribution of the climatological mean heat flux appears to be controlled by the dispersion of the Black Sea waters by the cyclonic circulation in the region.

In the seasonal buoyancy fluxes of Figure 3.23 (right panels), the strongest buoyancy gain by the sea due to the thermal component is observed in summer as expected, while the strongest loss during the winter. During these periods of highest fluxes, the strongest signals are observed in the Eastern Aegean Sea, possibly as a result of the mean cyclonic circulation, bringing warm waters through the extension of the Asia Minor Current in the eastern Aegean during winter, and due to

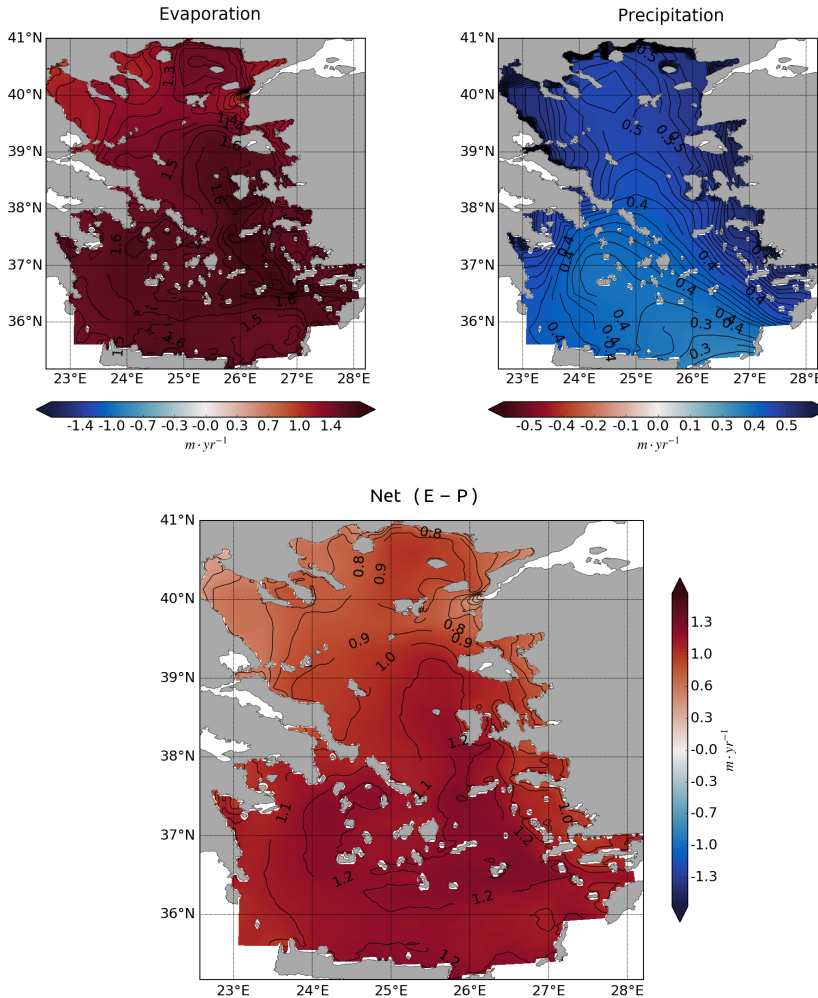


Figure 3.21: Mean water fluxes in equivalent meters per year at the surface, for the period 1985–2015. Evaporation (top left), Precipitation (top right), and the Net ( $E - P$ ) water flux (bottom) are indicated with positive values upward and negative values downward.

the effect of coastal upwelling in the summer. Weak buoyancy gain is observed in spring, with the northern and western parts of the Aegean exhibiting higher warming trends than the Eastern and Southern Aegean, possibly due to the coverage of the former by the cool modified Black Sea waters surface layer. Weak buoyancy loss is observed in the fall, intensified near the shores and bays surrounding the basin, possibly due to stronger heat losses because of the shallower and confined waters.

The 30-year climatological annual mean of the haline component of the buoyancy flux over the Aegean Sea is presented in Figure 3.24

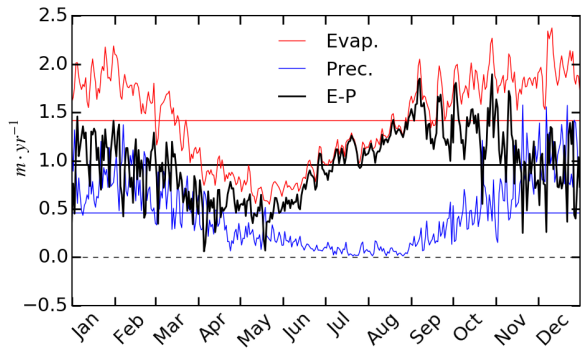


Figure 3.22: Seasonal cycle of Evaporation, Precipitation and Net water flux ( $E - P$ ) over the Aegean Sea, in daily values for the 1985–2015 period.

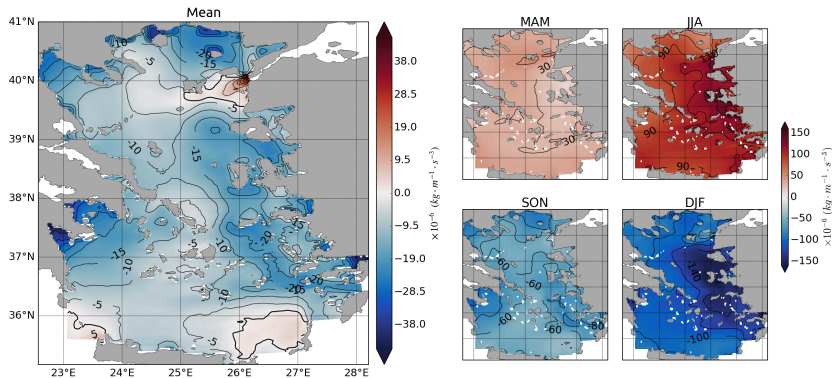


Figure 3.23: Buoyancy flux in the Aegean Sea due to the thermal component (see Eq. 2.5). Climatological mean (left panel), and seasonal (smaller panels to the right), for the 1985–2015 period.

(left panel). As the freshwater fluxes are dominated by the evaporative loss, the haline component is responsible for buoyancy loss from the sea surface throughout the Aegean. However, the buoyancy loss is moderated by the presence of the surface layer of the modified Black Sea waters extending throughout the northern and western shores of the Aegean. Lower SSTs, characteristic of the Black Sea waters, reduce the saturation specific humidity at sea temperature ( $q_s$ ) and consequently reduce its difference from the specific humidity of the atmosphere ( $q_a$ ) close to the sea surface ( $q_s - q_a$ ), thus reducing the amount of evaporated water.

In the seasonal haline component of buoyancy fluxes of Figure 3.24 (right panels), the haline component of the flux appears to be controlled by the low SST along the northwestern shores of the Aegean Sea during spring and winter, as determined by the Black Sea water dispersion by

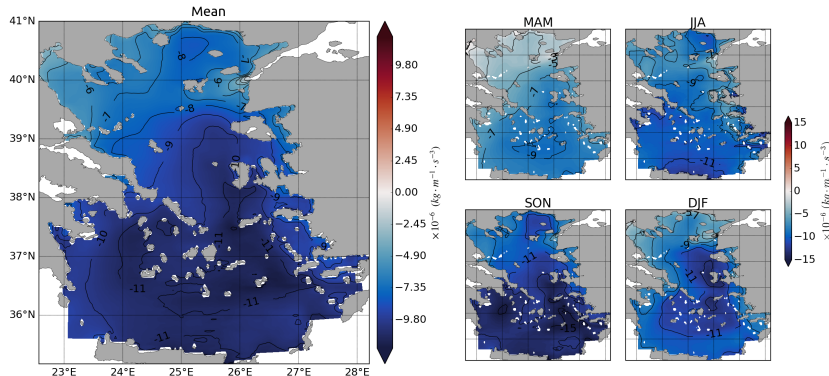


Figure 3.24: Buoyancy flux in the Aegean Sea due to the haline component (see Eq. 2.5). Climatological mean (left panel), and seasonal (smaller panels to the right), for the 1985–2015 period.

the cyclonic circulation. The highest buoyancy loss due to the haline component takes place in fall (September to November), a fact that must be attributed to high evaporation rates due to the highest SST values during that period and low air-temperatures.

Comparison between the two components of buoyancy flux (Figs. 3.23 & 3.24) shows that the thermal component is about two times larger than the haline component on an annual basis. Thus, the spatial distribution of the annual mean buoyancy flux (as given by the combination of components in Eq. 2.5) resembles the distribution of its thermal component, i.e. it is moderated by the dispersion of the Black Sea waters throughout the Aegean Sea (Figure 3.25).

In the limited region close to the Dardanelles exit in the northeast Aegean Sea, the mean buoyancy loss changes sign, as the sea gains buoyancy from the atmosphere on an annual basis due to the very low SST of the outflowing Black Sea waters through the Straits (because latent and sensible heat fluxes as well as the emitted longwave radiation are reduced). This buoyancy gain corresponds solely to the flux through the air-sea interface and is independent of (a) the insulating role of the thin surface layer, acting as a buffer to the transfer of heat and buoyancy to subsurface layers, and (b) of the lateral input of buoyancy to the North Aegean through the strait.

In order to compute the lateral buoyancy flux from the Dardanelles using Eq. 2.6, the time-dependent three-dimensional mean potential density of the Aegean was estimated (Fig. 3.26). This quantity exhibits a seasonal cycle, reflecting the variability of the shallow and intermediate layers.

Furthermore, the increase in the mean density of the deep layers during intense dense-water formation events in 1987, 1992, 1993, 2000, 2006, and 2012, as well as the stagnation periods of gradually decreasing

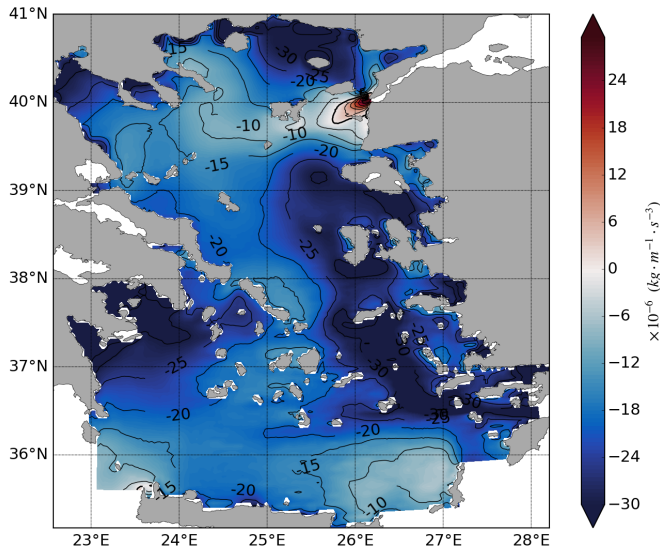


Figure 3.25: Mean net buoyancy flux in the Aegean Sea due to both the thermal and the haline components (see Eq. 2.5), for the 1985–2015 period.

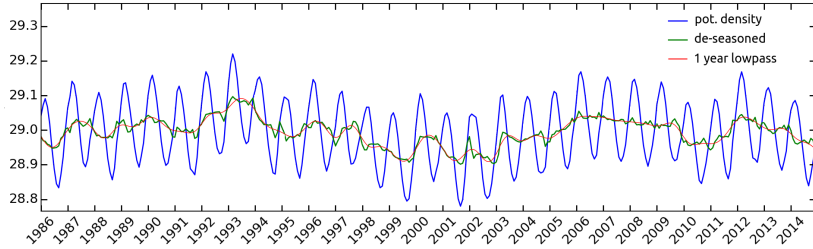


Figure 3.26: Temporal evolution of weighted-mean potential density averaged over the entire Aegean basin. Monthly time-series (blue), de-seasoned signal (i.e. monthly – climatology) of interannual variability (green), and a low-pass filtering of the de-seasoned with a Butterworth filter and a cutoff frequency of 1 year (red).

mean density is also distinguishable in the figure (also comparable to Fig. 3.16).

Using the aforementioned mean potential density time-series, as well as the density of the Dardanelles-strait current, the Dardanelles lateral buoyancy flux contribution is assessed, by converting it to equivalent of the Aegean surface flux and comparing it to the surface buoyancy flux and its thermal and haline components (Figure 3.27). While both surface

fluxes remove buoyancy from the Aegean Sea (the thermal component at a rate of about  $12.0 \times 10^{-6} \text{ kg m}^{-1} \text{ s}^{-3}$  and the haline component at a rate of  $8.5 \times 10^{-6} \text{ kg m}^{-1} \text{ s}^{-3}$ ), the lateral Dardanelles buoyancy flux introduces an additional  $11.3 \times 10^{-6} \text{ kg m}^{-1} \text{ s}^{-3}$  of buoyancy, almost canceling out the thermal loss. It is clear from the analysis that when considering the whole Aegean Sea, the Dardanelles contribution marginally reduces the overall buoyancy loss. However, such a reduction applied only over the North Aegean is roughly doubled, totally altering the character of this sub-basin.

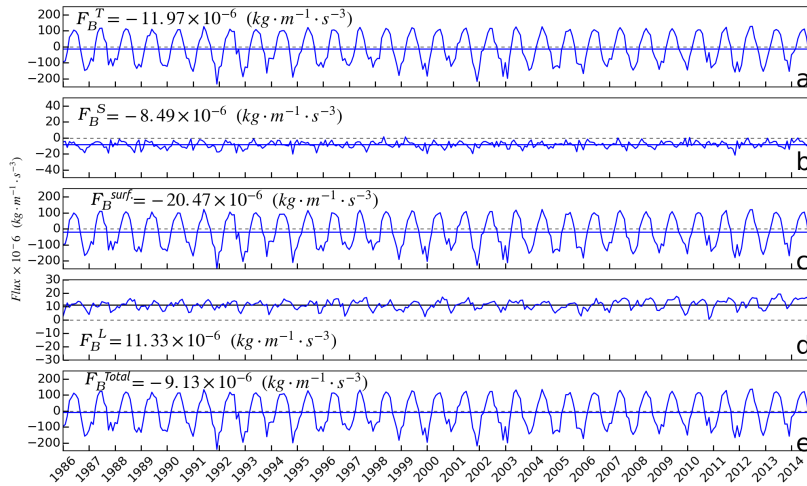


Figure 3.27: Temporal variability of buoyancy fluxes, as described in Eqs. 2.5 and 2.6: surface thermal component (a), surface haline component (b), surface buoyancy flux (c), lateral buoyancy flux from Dardanelles (d). Finally all the fluxes are added to calculate the total buoyancy flux at the surface of the Aegean Sea (e).

### 3.2.4 Principal Component Analysis

In the previous Section, the climatology of surface fluxes (energy, freshwater and buoyancy) was investigated for the Aegean Sea, incorporating their seasonal variability in the analysis in some cases. This approach however, is not describing the inherent climatic variability of the system in an intra-annual and/or inter-annual level. Here, Principal Component Analysis is incorporated to decompose the spatio-temporal signal and investigate de-correlated modes of variability through Empirical Orthogonal Functions (EOF), revealing both the seasonal and internal variability of the Eastern Mediterranean - Black Sea system, in an attempt to also discern its spatial patterns where possible.

For this reason, the buoyancy flux component was selected for performing the analysis on, as it is considered the most inclusive in terms of the range of variability it can explain. This comes from the fact that the surface buoyancy flux incorporates both the heat flux and the fresh-water flux in its calculation (Eq. 2.5), thus reflecting a composite of the variability of these constituents. It should be noted, that with this analysis it is only possible to discern the combined variability of heat and fresh-water fluxes, and not their individual contribution. However, the analysis of buoyancy flux variability is important for an additional reason; it is in large responsible for the variability in surface forcing of the thermohaline functioning of the basin.

The monthly-averaged buoyancy flux field is decomposed into modes of principal components time-series (or eigenvalues) and the associated two-dimensional fields (or eigenvectors). The first six modes explaining  $\sim 98\%$  of the total buoyancy flux variability of the region (including the seasonal signal), are shown in Figures 3.28 and 3.29. In order to calculate the contribution of each mode to the total buoyancy flux, each EOF field should be multiplied by the respective PC time-series, which results in units of  $10^{-6} \text{ kg m}^{-1} \text{ s}^{-3}$ . Principal Component Analysis is not based on physical principles, but rather on mathematically partitioning orthogonal (independent) modes within a dataset, which however retain a sound statistical nature. Analysing components (especially those of higher order) is prone to misinterpretation regarding the physical mechanisms that might be responsible for the variability shown. For this reason, apart from the first two modes, the rest are presented here with the intention of providing a statistical background to the internal variability of buoyancy fluxes, while any interpretation provided should be viewed more as a hypothesis than an explanation of underlying mechanisms.

The first two EOFs can be clearly associated with the seasonal variability of the system (accounting for about 95% of the total), because of the periodic nature of their Principal Component's time-series. Most probably, the first EOF reflects the seasonal heat flux component of the variability, as it oscillates over the whole domain between positive and negative values, following the seasonal signal of heat flux as in Fig. 3.20. The largest variability is observed over the central and east Aegean Sea, as well as along the southern Anatolian coast. The variability of the Black Sea in this mode is very small compared to the rest of the Eastern Mediterranean, which correlates very well with the pattern of lower short-wave and long-wave radiation in the Black Sea (Fig. 3.19).

In the second EOF, the positioning of highest variability is in areas where two different water masses meet (river outflows, Dardanelles exit, West-Mediterranean water inflow). This observation points towards a contribution of seasonal variability due to the lateral water input in the domain, which affects both the local salinity term in Eq. 2.5, as well

as the local energy exchange with the atmosphere because of the typically reduced temperatures of the imported water in all aforementioned regions<sup>1</sup>. Again, one of the regions of largest variability lies within the Aegean Sea.

The third EOF, features an oscillating-dipole pattern distinctly separating the western and eastern parts of the domain. The largest variability in this mode, lies (apart from the Tyrrhenian Sea and Sicily strait) within the central Aegean and the northern Adriatic (known producers of dense water). However, there is not a distinct periodicity in the PC time-series while there are certain events of intense buoyancy loss in the north Adriatic (e.g. positive spikes in 1988, 1991, 2000, 2001, 2007, 2010, 2011, 2012, 2014) and the central Aegean (e.g. negative spikes in 1989, 1993, 1995, 1996, 2002, 2003, 2006, 2012).

In the fourth EOF mode, there is again a dipole, this time separating the north from the south part of the basin along the line Sicily strait - Crete - Bosphorus strait - Kerch strait, and portrays again the north Aegean as the region of highest variability together with the eastern Levantine Sea. This north-south pattern in combination with the fact that the largest spikes in the PC timeseries occur only during cold months with an abrupt reversal from negative to positive values, suggests a combination of energy fluxes in this mode of variability.

The fifth EOF mode shows a specific pattern of regions known for having persistent cyclonic circulation being in phase, while there is a corridor-like structure in the Aegean Sea following the prevailing direction of the Etesian winds. This would suggest a combination of wind and circulation-induced upwelling/downwelling, and heat exchange with the atmosphere. The dominant frequency of the variability as seen in the PC time-series, is twice per year, with the cyclonic structures loosing buoyancy mainly during cold months (when upwelling due to cyclonic pumping brings relatively warmer water in contact with the colder atmosphere). The aforementioned regions in the Aegean Sea, are loosing buoyancy mainly during the summer months.

The sixth EOF mode is less coherent, with eddie-like structures appearing in the field, and the highest variability found in the Aegean Sea and the African coast south of Crete.

---

<sup>1</sup> Note that the blue (negative) sections in the map, become positive when multiplied by the PC during winter and early spring (also negative)

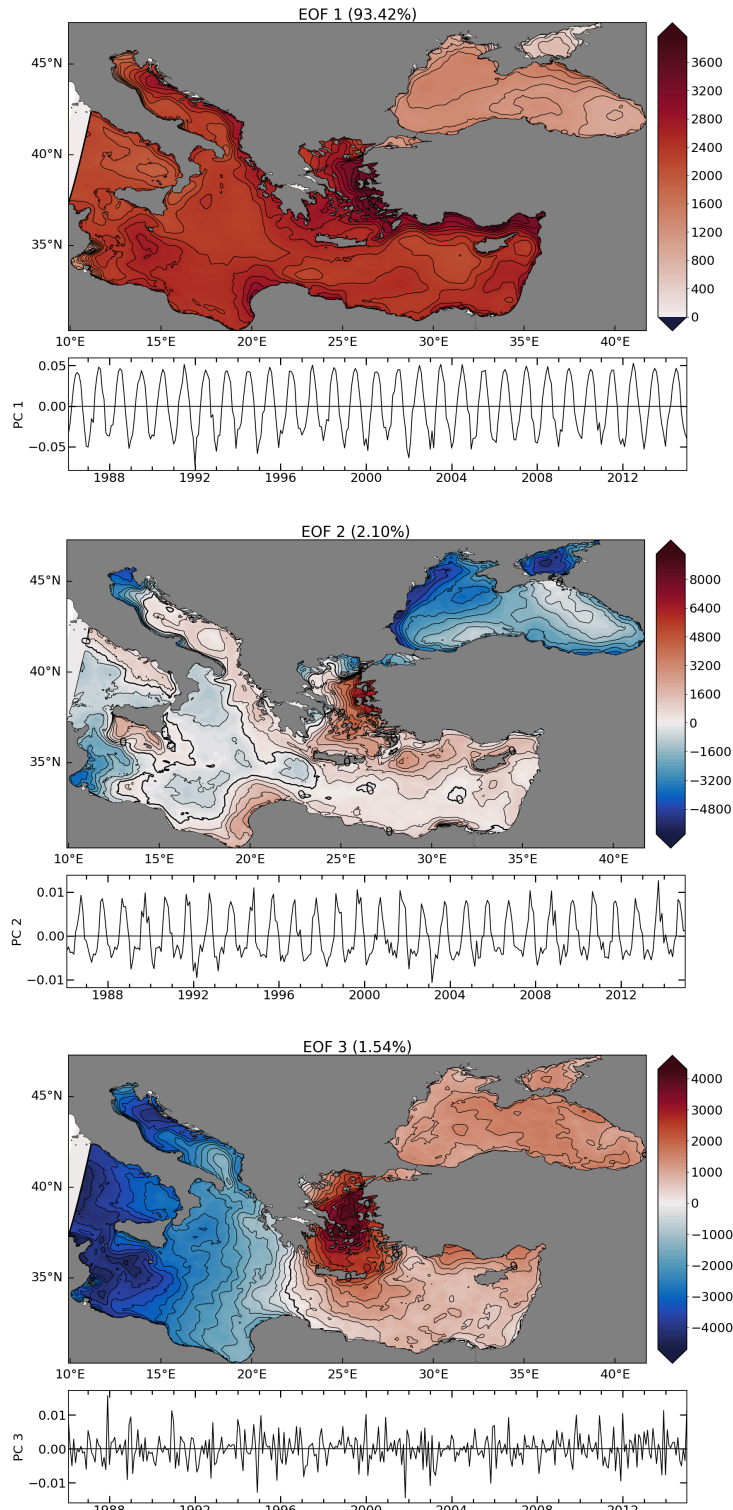


Figure 3.28: The first three EOF modes (1 to 3) for surface buoyancy flux, and the associated Principal Component (PC) time-series. In parentheses, the percentage of the total variability that each mode explains. See text for an explanation on units.

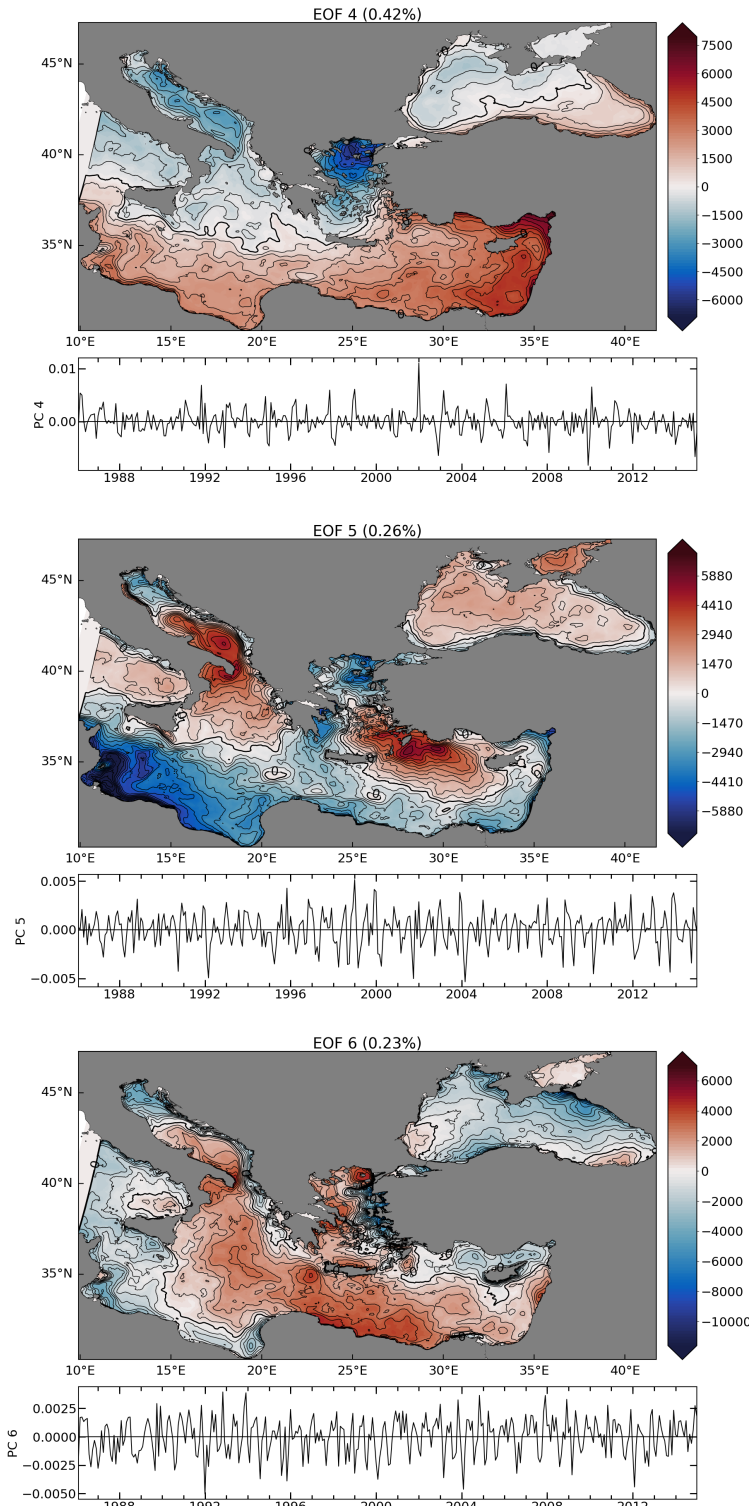


Figure 3.29: Same as in Figure 3.28, for EOF modes 4 to 6.

The importance of the Aegean Sea is highlighted throughout this section, as a major contributor to surface buoyancy flux variability, and thus a region that influences large the surface forcing variability and consequently the thermohaline functioning of the Eastern Mediterranean - Black Sea system.

### 3.3 MARINE HEATWAVES

Marine heatwaves occurring in the Aegean Sea are detected in the EMBS surface temperatures using the methods discussed in Section 2.2.4, for the 1985–2015 period. This follows the Hobday et al., 2016 definition, where the local daily SST anomaly must be exceeding the local 90th percentile for 5 days or more, allowing for 2-days break in between. Heatwave metrics and evolution of SSTs are shown for the 30-year period, while atmospheric and sea surface temperature anomalies are examined and compared for some case-periods exhibiting MHW conditions. Next, the global warming-trend signal is removed from ocean and atmospheric datasets, and heatwaves are detected in both domains. In this case the same criteria are used for the MHWs, while the atmospheric heatwaves are defined using the local 90th percentile of daily maximum 2-meter temperatures, with a minimum duration of 3 days allowing for a 1-day break in between. Here the focus is not on the statistics of heatwave occurrence themselves, but rather on the direction of interaction during co-occurring marine-atmosphere events.

#### 3.3.1 *Detection & Metrics*

Maps of spatial distribution for the number, mean duration, mean intensity and  $HW_{esi}$  (as defined in Section 2.2.4) of MHWs detected in the Aegean Sea, are presented in Figure 3.30. The number and mean duration maps demonstrate a complementary behaviour, meaning that areas with lower number of MHWs showcase higher mean duration values. This is expected to some degree, as their product (number  $\times$  duration) describes the total number of days under heatwave conditions, which remains fairly constant on a regional level considering the proportional criterion of selection (90th percentile), however the criterion on heatwave duration (5 days or more) also plays a differentiating role. The largest number of MHW events occur over the northern, north-western and western coastal areas of the Aegean Sea, a finding that agrees with a similar observational/modelling study (Androulidakis & Krestenitis, 2022). The south and south-east areas of the domain (especially the Cretan Sea) appears to host longer-lasting events. The highest mean intensity of these events is found around the Dardanelles exit, the Gulf of Saros (north of Dardanelles strait), as well as parts of northern

and central Aegean. Arguably based on these three metrics, it appears that areas which demonstrate the largest SST variability, host more MHW events that are shorter in length and more intense, while areas with lower SST variability host fewer, less intense and longer lasting events. Although it is demonstrated in literature that excessively high temperatures (or mean intensity of a MHW event) is a stress factor for species and especially the less mobile/benthic ones, it is not as clear whether ecosystems are affected stronger by longer-lasting events or by shorter and more frequent ones. Resolution of the latter argument (given more data), could help to realistically calibrate the ecosystem stress index. However, assuming an equal contribution of the above metrics to ecosystemic stress, produces the depicted  $HW_{esi}$  (Fig. 3.30). The  $HW_{esi}$  is largest at the Dardanelles exit, and along coastal areas and gulf of the northern Aegean Sea. Other places of interest are clusters of high  $HW_{esi}$  in the Cretan Sea, the central Aegean Sea and the region around the National Marine Park of Northern Sporades (which falls within the black rectangle of figure 3.30).

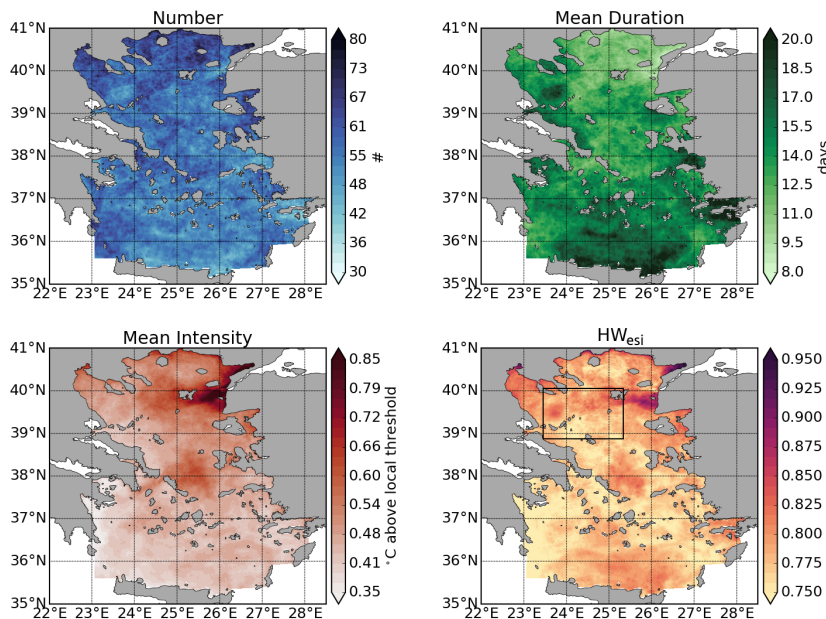


Figure 3.30: Detection metrics for MHWs in the Aegean Sea, after applying the Hobday et al., 2016 definition on EMBS simulation SST data (1985–2015). Total MHW number (top left), mean duration (top right), mean intensity (bottom left) and ecosystem stress index –as expressed in Eq. 2.7 using proportional weighing of factors (bottom right). The black rectangle designates the area over which the timeseries of Fig. 3.31 is calculated.

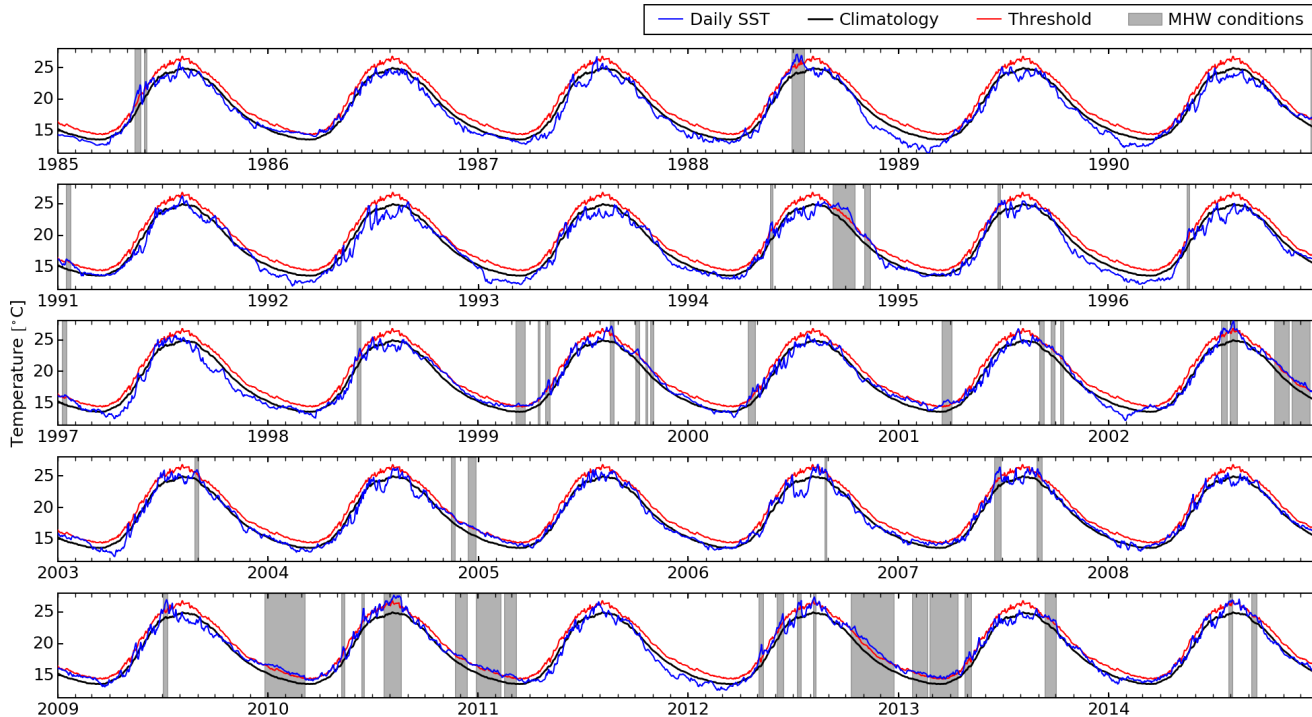
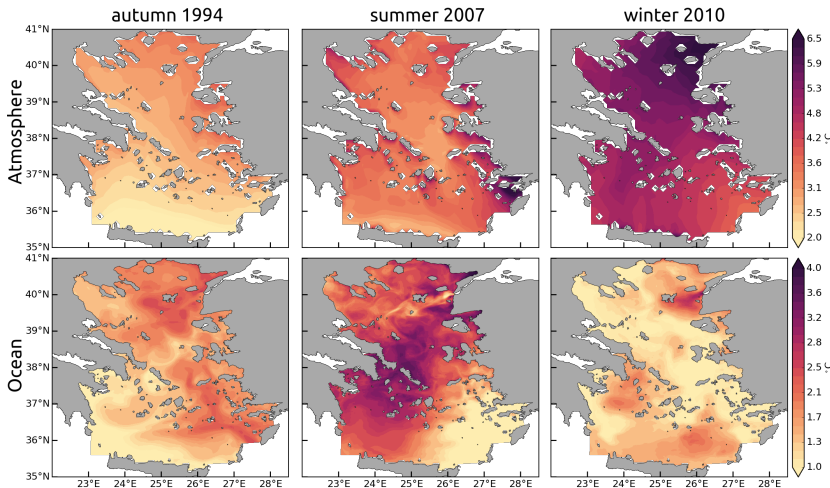


Figure 3.31: Daily SST timeseries for the 30-year simulation (in **blue**), spatially-averaged over the north Aegean Sea (black rectangle in Fig. 3.30). The equivalent climatology (**black**) and local threshold (**red**) are also shown. The resulting **MHW** periods are designated with **gray** bands.

A more descriptive picture of the heatwave detection, can be seen in Figure 3.31. The timeseries of daily spatial-mean of SSTs in northern Aegean is plotted, along the climatology and the local heatwave threshold, as set by the previously discussed criteria. Periods of MHWs emerge when the daily SST exceeds the local threshold for at least 5 consecutive days, and are shown with gray bands. Both shorter and longer enduring heatwaves can be seen, with spring and summer MHWs being relatively shorter and -in many cases- reoccurring within the same season. On the other hand the longer lasting events emerge during autumn and winter months and are not as recurrent. Part of the explanation for this, is that during warmer months the absolute difference between the threshold and the mean climatology is greater than that during colder months, which points to a greater variability range during the warm seasons. This means that the SST during warm months needs to become exceptionally high in order to exceed the threshold, a condition not maintainable for very long periods. By contrast, the proximity of the threshold to the climatology during colder months means that the heatwave conditions can be maintained for much longer, especially since the mixed layer is much deeper in winter (i.e. translating to a surface layer of much higher volume/thermal capacity, thus a much larger inertia). Finally, it is evident that the existing warming trend within the timeseries biases the heatwave occurrence, with more events towards the end of the 30-year period, as discussed in Section 2.2.4.

Averages of daily maximum atmospheric temperature anomalies and daily SSTs anomalies during MHW events are shown in Figure 3.32, for three distinct cases (autumn 1994, summer 2007 and winter 2010). The temperature anomalies are temporally-averaged over periods in which extensive marine heatwave events were taking place in a large proportion of the Aegean Sea, and are thus considered indicative of the spatial relations of conditions in the atmosphere and the ocean coinciding with MHWs, as well as their seasonal differences.

Atmospheric temperatures in Europe were exceptionally high during most of 1994, and especially the heatwave of late summer broke multi-decade-lasting records and drew public attention (Lhotka & Kysely, 2015; Urban et al., 2017). In the EMBS simulation data, a long-lasting autumn MHW is detected in the Aegean Sea, with a visible signal in the SST average anomalies of Fig. 3.32 which are large ( $> 2.5^{\circ}\text{C}$ ) over most of the north, central and eastern parts of the basin. However, the CCLM simulated atmospheric temperature anomalies -although positive- are not as intense ( $< 2.5^{\circ}\text{C}$ ), showing receding signs by that time and an out-of-phase behaviour for the two domains. In the second case, south-eastern Europe hosted a notoriously strong AHW during the summer of 2007, which gravely affected Greece (Founda & Giannakopoulos, 2009; Mircheva et al., 2017). Temperature anomalies are large in the atmosphere and exceptionally large in the ocean (reaching  $3.5\text{--}4^{\circ}\text{C}$  over



**Figure 3.32:** Mean anomalies for the atmospheric (top) and sea surface temperatures (bottom), during three distinct heatwaves (autumn 1994, summer 2007 and winter 2010-2011). The averaging windows for these three periods, coincide with extensive MHWs that took place in the Aegean Sea (see also Fig. 3.31).

large areas of the central-western Aegean). In combination with the fact that the summer mixed layer in the ocean is relatively shallow, shows an indication of concurrency with the ocean being affected by the atmosphere. The Black Sea region was much less affected during this heatwave, which can be seen in the distinct signal of much lower temperature anomaly import through the Dardanelles strait. Finally, the case of 2010 shows an extremely intense atmospheric temperature anomaly ( $> 5^{\circ}\text{C}$ ) over the whole Aegean Sea, even during the winter season i.e. months after the devastating summer heatwave over Russia and eastern Europe (Hoag, 2014). The ocean, although experiencing long-enduring MHW conditions (see also Fig. 3.31), demonstrates very low temperature anomalies, probably also due to the lower temperature variability during winter months, as previously discussed. The winter-time ocean mixed layer is at its deepest, which increases inertia due to the large volume/thermal capacity. This indicates signs of high atmospheric temperatures being accentuated by a long-lasting MHW event. Moreover, in this case there is an import of much warmer waters at the Dardanelles which originated in the Black Sea most probably through interaction with the atmosphere during the intense atmospheric blocking and heatwave conditions of the past summer. It should be stressed again here, that the above case-study analysis is not aiming to demonstrate causal or directional relations between atmospheric and marine heatwave events, but rather the intrinsic response and underlying physical state of a

complex system with interacting components (ocean-atmosphere), under extreme conditions.

### 3.3.2 Concurrent Events

Until now, no detection of atmospheric heatwave events has been performed. In order to characterize a heatwave event as concurrent (i.e. occurring in both the ocean and the atmosphere at the same time, without considering temporal lags in any of the domains), the global warming trend is firstly removed from both the **CCLM** atmospheric temperature data and the **EMBS** surface temperature data. An example for the ocean case is shown in Figure 3.33, where the average Aegean Sea **SST** anomaly is plotted against the average global **SST** anomaly, with a prominent much larger (almost twofold) warming rate for the Aegean Sea.

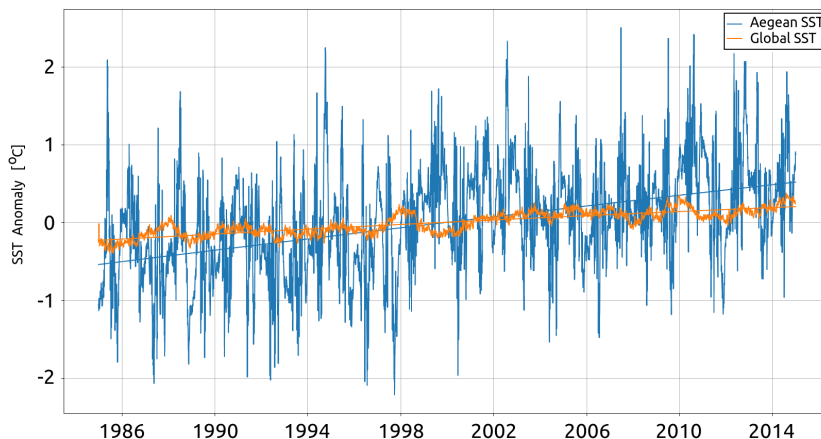


Figure 3.33: Timeseries of daily **SST** anomalies, averaged over the Aegean Sea (**blue**) and globally (**orange**). Linear fits of the global and local warming trends for the 30-year period are also shown (tested for statistical significance with MK-test).

The global warming trend is obtained from the globally averaged **ERA** interim dataset of daily maximum 2-meter temperatures for the atmosphere, and from the globally averaged **NOAA/NCEP** dataset of daily sea surface temperatures for the ocean. These trends are then compared to the temperature trend of each individual gridpoint timeseries, and the spatial distributions of warming ratios (local over global warming trends) can be seen in Figure 3.34. The atmosphere over the Aegean Sea is warming 1.7 to 2.2 times faster than the global mean, with the northern parts demonstrating the highest trends and south-eastern parts demonstrating the lowest ones. The Aegean Sea itself is warming in most parts between 1.6 and 2.4 times faster than the global ocean,

reaching lower values in the north, and northwestern parts, but certainly not below the global ocean trend (although with no statistical significance in those areas).

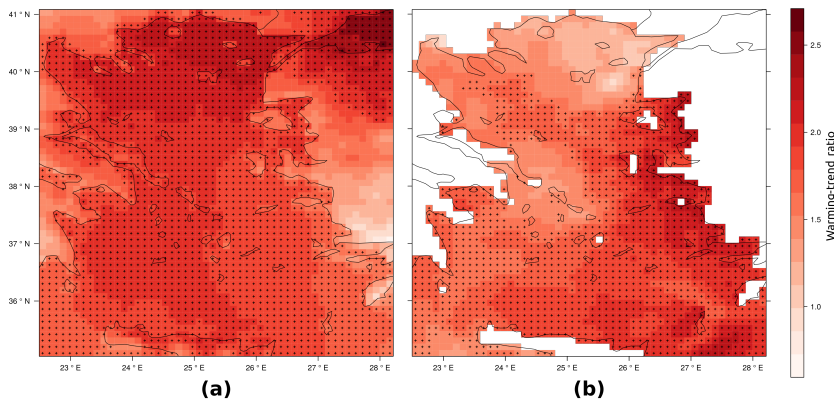


Figure 3.34: Relation between local and global warming-trends, for temperature data of (a) the atmospheric model and (b) the ocean model, for the period 1985–2015. A warming-trend ratio larger than (smaller than) one, means that the local trend is greater than (less than) the global trend. Black crosses designate statistical significance.

The global trends are then removed from the atmospheric and oceanic datasets on a gridpoint level, and heatwaves are again detected using the Hobday et al., 2016 definition using the selection criteria already discussed for the two domains. This forms a spatially varying database of heatwave days for both the ocean and the overlying atmosphere, and concurrent marine-atmosphere heatwave days are defined as those days in which a heatwave is present in both domains simultaneously.

In order to examine possible reinforcing through air-sea energy exchange during heatwave events (as described in Section 2.2.4), the anomaly of the simulated sea surface heatfluxes is temporally averaged for those days where a co-occurring marine-atmosphere event takes place. The result for the whole 30-year simulation period is shown in Figure 3.35. Surface heatflux anomalies are positive over the whole Aegean Sea, designating an overall input of heat from the atmosphere into the ocean during concurrent events.

This demonstrates an interesting one-way direction, in the sense that **AHWs** are shown to reinforce the ocean temperature anomalies and possibly either cause or help in the creation of a **MHW**. However this is merely a simplification of the whole picture, as seasonal differences in heatwave conditions are not taken into consideration. As discussed in Section 3.3.1, there is a larger **SST** variance in summer than in winter, while the intra-seasonal variance of net surface heatfluxes as depicted in Figure 3.20 is larger in the winter (most probably due to the larger vari-

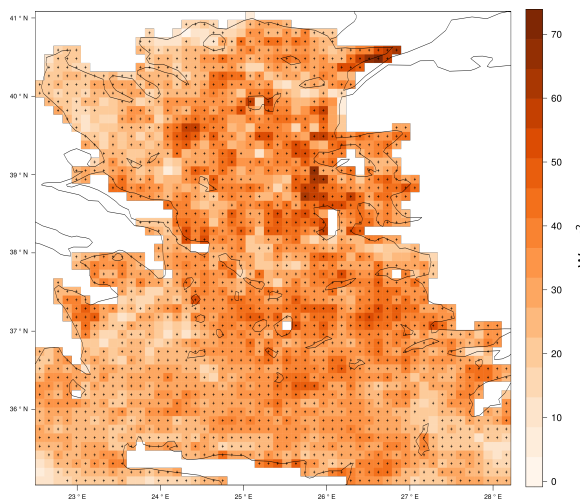


Figure 3.35: Surface heatflux anomaly during days with co-occurring marine-atmospheric heatwaves, as simulated by the EMBS model for the 1985–2015 period. Positive values designate excess heat flowing into the ocean; black crosses designate statistical significance.

ance of latent and sensible heat fluxes during those months). Moreover, there is no way of discerning whether the directionality portrayed by the heatflux anomaly represents a heatwave in one domain which reinforces an already existing heatwave in the other, or triggers one to happen<sup>2</sup>. For this reason it is considered valuable for the analysis, to differentiate the surface heatflux anomalies by averaging them in two clusters. Firstly according to season, and secondly according to heatwave occurrence in either one domain, the other or both.

The surface heat-flux anomalies are segregated according to season and type of event in Figure 3.37. Each column represents only the fluxes for a specific season, while rows represent different ways of calculating heat-flux anomalies. Positive values show a heat-flux direction into the ocean (or downward). The sign of daily heatflux varies across the year, however for the region under examination, daily average surface heatflux is negative (or upward) during the winter months and positive (or downward) during the summer months (e.g. see Chang et al., 2013, Fig. 3.20 and the thermal component of Fig. 3.27).

The top row represents differences in heat-flux anomalies during concurrent events compared to that of atmospheric events only, and values are mostly negative across seasons. The middle row represents differences in heat-flux anomalies during concurrent events compared

<sup>2</sup> This is because the anomaly is calculated over days of concurrent events in the two domains, but no information is included for the days before or after the concurrency. It is often the case that during those days heatwaves still exist in only one of the domains

to that of marine events only, and here values are mostly positive across seasons. This is conceptualized in Figure 3.36 for the cases of winter and summer, but the underlying idea can be extended to all seasons. In essence, the negative values in the top row of Figure 3.37 show that the main difference of a concurrent heatwave from a standalone atmospheric heatwave, is an increased heat input from the ocean to the atmosphere. In turn, the positive values of the middle row, shows that the main difference of a concurrent heatwave from a standalone marine heatwave, is an increased heat input from the atmosphere to the ocean. Put another way, during a concurrent event each domain receives more heat input from the other domain than it would if it was under a self-standalone event, which by itself represents a reinforcement mechanism that makes concurrent heatwaves more severe for both the atmosphere and the ocean, and especially so in the winter months.

The bottom row of Figure 3.37 represents differences in heat-flux anomalies during concurrent events, with respect to the average of single-domain events (either atmospheric or marine). This is in essence a residual of the first two rows, which shows whether the reinforcing mechanism of concurrent events discussed above shows a preference in direction. The slightly positive values overall demonstrate that the additional severity of a concurrent heatwave event with respect to a standalone one, is impacting the ocean more than the atmosphere (heatflux anomaly downwards).

The summer months in general, demonstrate values closer to zero (either slightly positive or slightly negative), which means that heatfluxes during summertime concurrent events are not differentiated as much with respect to standalone events (or in other words, in the summer concurrent heatwaves are not much more effective on either domain than single-domain heatwaves).

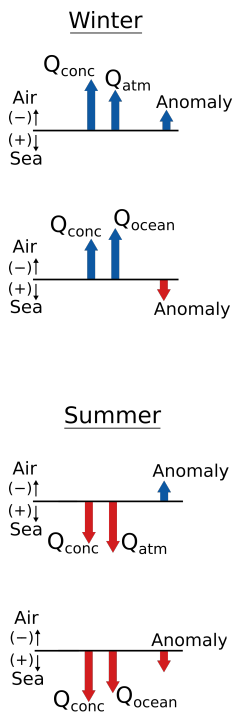


Figure 3.36: Conceptual schematic of heatwave flux direction at the atmosphere-ocean interface during winter and summer heatwaves (not to scale). The fields of Fig. 3.37 represent what is portrayed here as *Anomaly*.

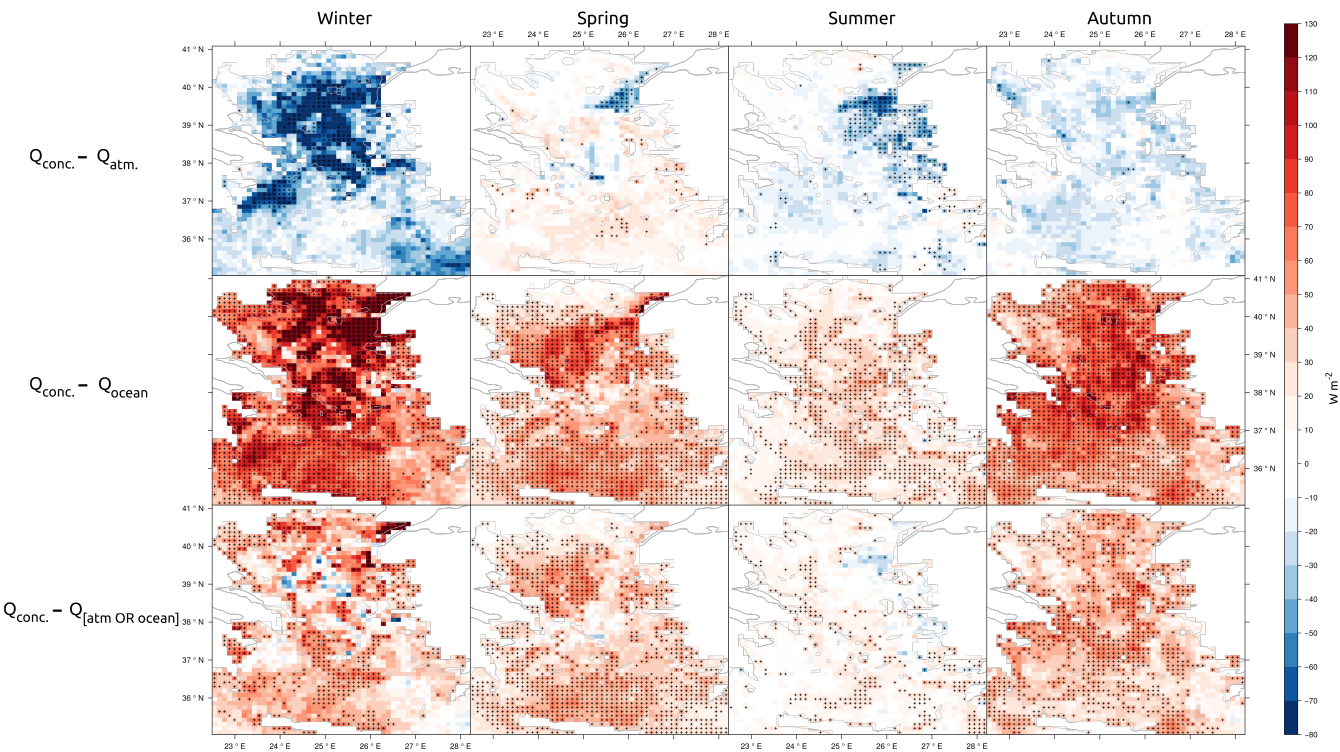


Figure 3.37: Comparison of seasonal surface heatfluxes during standalone atmospheric, standalone marine and concurrent marine-atmospheric heatwaves, in the Aegean Sea. **Top row:** Anomaly of surface heatflux during days of concurrent events ( $Q_{\text{conc.}}$ ), with respect to days of only atmospheric heatwaves ( $Q_{\text{atm.}}$ ). **Middle row:** Anomaly of surface heatflux during days of concurrent events ( $Q_{\text{conc.}}$ ), with respect to days of only marine heatwaves ( $Q_{\text{ocean}}$ ). **Bottom row:** Anomaly of surface heatflux during days of concurrent events ( $Q_{\text{conc.}}$ ), with respect to days of either marine or atmospheric heatwaves ( $Q_{[\text{atm. OR ocean}]}$ ). Positive values (red) designate heatflux into the ocean: ( $\text{atmosphere} \rightarrow \text{ocean}$ ), and vice versa (for a thorough interpretation see text).



# 4

## DISCUSSION

---

*“Words are flowing out  
like endless rain into a paper cup,  
They slither while they pass,  
they slip away across the universe”*

– John Lennon, *Across the Universe*

IN THIS CHAPTER: A discussion recapitulating the findings of this study and expanding on some aspects and interpretations not covered in the results. See Chapter 5 for a synoptic conclusion on the main innovations of this study.

### 4.1 SIMULATION PERFORMANCE

A novel modeling setup was hereby introduced for the simulation of the interconnected Eastern Mediterranean – Black Sea system (**EMBS**), in order to produce a tool for improved climatic hindcasts and future projections for the Aegean Sea. The evaluation of the **EMBS** simulation performance through comparison of the 30-year-long hindcast (1985 – 2014) to available hydrographic/oceanographic observations and data, exhibits positive results and reveals a satisfactory representation of the physical oceanography of the interconnected Eastern Mediterranean–Black Sea system on climatic timescales, also being among a handful of existing modeling configurations today able to simulate the interacting system. Despite the absence of relaxation and data assimilation schemes, the free-run simulation bias and **RMSE** are low and consistent for all fields, comparable to operational model results. The structure and intensity of the exchange flows in the straits of Dardanelles and Marmara were reproduced with impressive accuracy, despite the relatively low grid resolution of about 1 km at contraction points and the use of a hydrostatic model. All the goals that were established upon creation of the simulation were achieved (see Section 2.1.1), with the resulting model proving to be a very capable tool for climate studies in the region. Due to the extended validation of the model presented hereby, a presentation of the interannual variability revealed through the hindcasts is beyond the context of this work.

The representation of simulated surface fields (temperature and surface elevation) as validated against satellite observations/reanalysis is fairly accurate for such an extended free run, and most of the known surface circulation features of the basin are reproduced, as seen in Figure 4.1. However, there are some discrepancies which can be attributed to either flaws in the model configuration (i.e., grid setup, atmospheric forcing, etc.), or the satellite reanalysis itself. In more detail, the simulation shows some inaccuracies in meso-scale phenomena in the southern part of the domain and especially eddies and gyres south of Crete and in the Levantine basin, specifically: the Pelops Gyre (SW of Peloponnese) appears cyclonic instead of anti-cyclonic, the northern gyre of the Mersa Matruh System (north of Alexandria, Egypt) is properly represented but the southern gyre is missing, the Shikmona Gyre (south of Cyprus), the Ierapetra Gyre (south of Crete) and the Western Cretan Gyre, are all represented, but they appear to be of much lower intensity and/or shifted in position (see Figs. 3.12a and 4.1). Spatial variability of the general circulation and sea elevation seems to be reduced when compared to the altimetry (see Sections 3.1.1 and 3.1.2); however, it is similar to that of other modeling systems of comparable configuration like **MFS** (see Pinardi et al., 2015), while the gyres mentioned above are much better represented in shorter temporal averages (i.e., daily, monthly, seasonal, etc.—not shown here). The deformation of the grid due to variable resolution leads to a very low ratio of  $x$  to  $y$  gridbox dimensions in the region (Figure 2.2), which inserts different scales in the solver and is known by the model developers to be an impediment in smaller scale hydrodynamics. This, together with the relatively higher resolution in the area (5–7 km) can be part of the explanation for the misrepresentation of these few meso-scale phenomena in the southern-most part of the domain by our simulation. However, we cannot rule out the possibility that the discrepancy of the **EMBS** and **AVISO** fields could be attributed to the low temporal resolution of the satellite products, in comparison to the near-continuous record of the modeled results. In the latter case, transient mesoscale eddies would be averaged out in a 30-year long record, while averaging over a more discrete data set (as in the case of the satellite record) could result in aliasing causing high wavenumber artifacts. Further investigation of this is not within the context of the present work, but is planned for a subsequent analysis. In other parts of the domain, and especially in coastal regions, land contamination is reported to reduce the accuracy of satellite altimetry (Andersen & Scharroo, 2011), while corrections for inverse barometer, tide and high frequency wind effects on the satellite data (Ponte & Ray, 2002) can lead to reduced accuracy in regions where these corrections are difficult to model. Additionally, inaccuracies in the riverine-discharge dataset can lead to deviations in the temperature and salinity fields, which, keeping in mind the large volumetric flows of rivers involved in this simulation,

can be responsible for a considerable fraction of the simulation bias. This is evident when comparing surface fields (e.g., SST in Figure 3.1) with vertical profiles (e.g., temperature in Figure 3.15d), where it can be seen that deviations are larger at the surface, but much lower further down the water column, indicating a connection to surface processes (e.g., fresh water input/output through river discharges or through atmospheric forcing precipitation/evaporation). All the above can provide the reasoning behind the larger Bias/RMSE of the simulation in shallow regions, like the north-western plateau in the Black Sea or the northern part of Adriatic Sea (both of which are shallow and recipients of major riverine discharges), the south-east/east coast of the Levantine and other such coastal areas. Nevertheless, on climatic scales the bias, RMSE, and more importantly, the seasonal variability and inter-annual variability of these fields are all very well reproduced. A comparison of the Aegean and Levantine Seas SST with results from comparable models like ALERMO in (Vervatis et al., 2013), shows a similar structure of the basin-averaged interannual timeseries and average SSTs, with temperatures being slightly higher overall in our model. This can be partly attributed to the different periods of reference (1960–2000 for the ALERMO run and 1985–2015 for the EMBS). When compared to AVHRR/satellite SSTs, temperatures are slightly overestimated by our simulation and slightly underestimated by ALERMO (Vervatis et al., 2014). Results for the eastern Mediterranean SST from the MED36 simulation in (Mavropoulou et al., 2022), demonstrate an overestimation with respect to the AVHRR timeseries similar to that of EMBS, and a comparable warming trend.

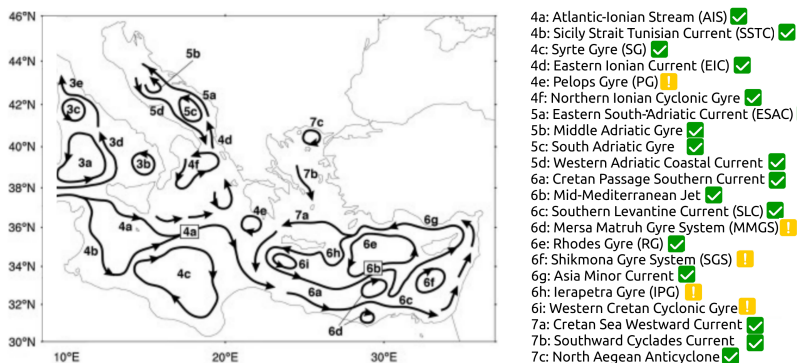


Figure 4.1: Known surface circulation patterns of the Eastern Mediterranean, as reproduced by the assimilated MFS simulation for the 1987–2007 period (Adopted from Pinardi et al., 2015). Names of these circulation features are provided in the legend, along with a designation of whether they are also represented by the EMBS simulation properly (green), or partially (yellow), as demonstrated by the surface circulation of Fig. 3.12.

The main reasoning for interconnecting the Black Sea with the Eastern-Mediterranean Sea in a single modeling domain, is the ability to simulate the exchange of water properties between the two domains, enabling one to influence the other as is the case in the physical world. Important efforts have already been established by other studies (i.e., the chain-model of Maderich et al.), towards a physically accurate representation of the long-term climatic water exchange at the **BMD** straits, in terms of average volumetric flows with part of the respective variability being modeled. Nevertheless, there is plenty of room for improving both the average flow and the full extent of the seasonal/inter-annual variability of the exchange, which is of crucial importance for a physically accurate representation of the interactions taking place between the sub-domains. This has been achieved to a great extent in the **EMBS** simulation, with large improvements in the average upper layer flow as well as in the overall variability of the flow in both layers (when compared to the chain-model with respect to observations). There has not been such an improvement in the average lower layer flow (with values being comparable to those of the chain-model), and this means that the influence of the Black Sea on the Aegean Sea is going to be more prominent than vice versa (because the lower layer describes the flow from the Aegean to the deep layers of the Black Sea); this is acceptable for the purposes of this study, which focuses on the Aegean/Eastern-Mediterranean Seas. The proper representation of the lower layer flow is hindered in this case, mainly by the hydrostatic approximation of the model in combination with the intensely variable bathymetry at the Bosphorus and especially the Dardanelles straits. However, the improvement in the simulated water characteristics of the Aegean Sea compared to studies that do not incorporate the exchange properly in their resolution is evident in the vertical profiles analysis, proving both the importance and success of such a setup. The analysis of vertical transects along the Bosphorus–Marmara–Dardanelles line shows very good agreement with past observational studies, both for temperature and salinity. The two-layer flow is clearly well-reproduced in the fields. The larger variability of flow partitioning between upper and lower layers in Dardanelles strait, as seen in Figure 3.8, can be attributed to the physical shape of the two straits and the subsequent differences in hydrodynamic behavior. The Bosphorus strait's shape is more consistent, with an almost constant width throughout its length, while the Dardanelles strait features a diverse geometry with several contractions and expansions in its width. The consistently narrow, channel-like width of Bosphorus leads to fewer degrees of freedom in a hydrodynamic sense, and a more stable partitioning of the flow between the upper and lower layers compared to Dardanelles. Another factor affecting the variability of partitioning of the flow between upper and lower layers, could be external forcing; the along-strait wind stress on the Dardanelles' upper layer may display a

larger variability compared to Bosphorus, due to the strait's position as well its direction compared to the locally prevailing winds and/or seasonal systems (i.e., the Etesians). Although the simulation uses the hydrostatic approximation, indirect effects of the hydraulic control at the straits are reproduced in the form of internal lee waves and changes in upper and lower layer thicknesses (Fig. 3.10). It is clear from the analysis in this study, that flow at Dardanelles strait transitions periodically to hydraulic control for an extended period during the year. The analysis of Kanarska and Maderich, 2008 shows that Dardanelles strait is closer to the viscous-advection-diffusive limit than the hydraulic solution limit. However, the range of possible flow regimes for Dardanelles in that study allows for hydraulic control, which probably takes place due to the large flow variability in the strait (Tab. 3.3).

The general circulation follows known patterns as observed by satellite altimetry, and cyclonic and anticyclonic features as well as jets and currents are well reproduced, with the exception being meso-scale phenomena in the southern portion of the domain, as discussed above. In addition, there is a discrepancy in the Black Sea circulation and some patterns are being exaggerated while others depreciated in terms of intensity. The simulated horizontal circulation as discussed above, in combination with the simulated vertical overturning circulation as depicted in zonal and meridional streamfunctions, demonstrate that the thermohaline functioning of the basin is clearly and accurately reproduced, with surface western Mediterranean waters entering the eastern Mediterranean through the Sicily strait, branching in the Ionian to a northward branch towards the Adriatic and an eastward branch towards the Levantine. Intermediate waters are formed in the Levantine (**LIW**), which then flow towards the western Mediterranean, while Eastern Mediterranean Deep Waters (**EMDW**) are formed in the western part of the Levantine Sea and disperse towards the south Ionian and the east Levantine. Meridional streamfunctions in the Adriatic and the Aegean highlight the special role and similar functioning of these two basins. It is evident that the diverse bathymetry of the Aegean Sea acts as a hindering factor in the transport of benthic dense water formed in its various deep pits and basins, in contrast with the naturally-southward-sloping of the Adriatic/north-Ionian Seas' bathymetry, making the transport of dense waters towards the south Ionian much easier in that case. Dense waters formed in the various deep Aegean pits gradually propagate southwards via either turbulent mixing with overlaying layers, or displacement by denser waters. The surface pools of less saline waters, one due to Black Sea inflow and the other due to riverine inflow, are visible in the overturning functioning of the Aegean and Adriatic Seas, respectively. The intensity, shape and volumetric transports of the eastern Mediterranean zonal streamfunction, as well as the Adriatic and Aegean meridional streamfunctions, compare very closely to that presented in (Mavropoulou

et al., 2022). However, the anti-clockwise circulation cell caused by Black Sea water inflow at  $\sim 40^\circ$  N and 0–250 m depth reaching southward to  $\sim 38^\circ$  N and 0–100 m depth (Figure 3.13c), is shallower and not as pronounced in the simulation results of Mavropoulou et al. This can be probably attributed to the better representation of the Black Sea water inflow and its variability in the EMBS simulation.

The evaluation of the simulation within the whole water column highlights that its performance is good overall for a free-running model. Comparison with in situ profiles as well as operational assimilated model profiles, shows accurate representation of both the average profiles as well as their variability, with performance being very close to and even exceeding that of the assimilated model in specific areas. In the north Aegean Sea, there is an evident improvement in the modeling of water characteristics (especially salinity and potential density), which is attributed to the accurate representation of Black Sea water characteristics and inflow. In the Ionian and Levantine basins performance remains very high and close to that of the assimilated simulation (including variability). In the Adriatic and Black Sea, the bias and RMSE for all fields, but especially for salinity, point towards riverine inflow under-representation as a forcing term. It is very probable that the inclusion of only the Po river in the Adriatic leads to an overestimation of both salinity and temperature by the EMBS simulation, a fact nevertheless that translates to a slight overestimation of density only in the first 20–30 m, while being very close to the observations in the rest of the water column. In the Black Sea, similar overestimation is observed while the variability inherent in the observations is reproduced by the simulation, but not by the assimilated one. In general, all metrics show acceptable reproduction of the observed potential density, which is of paramount importance for proper simulation of the density driven flows in the domain.

It is evident from the results and their interpretation, that including the interaction of the Mediterranean with the Black Sea in the simulation configuration, greatly improves the capacity to generate long-term simulations of the oceanographic properties and circulation of the domain, especially in the Aegean Sea. The absence of any need for assimilating observational data during the simulation and the minimal drift, if any, that the final product demonstrates, highlight the potential of this modeling setup to be used in hindcast as well as future projection climate studies.

#### 4.2 APPLICATIONS

The successful completion of the validation process for the 30-year EMBS simulation, designates that the hindcast can be further analysed to help describe some known physical problems in the region.

The thermohaline circulation of the Aegean Sea and its response to the interannual variability is often studied in terms of the meteorological and oceanographic forcing, but very few studies focus on the forcing mechanisms themselves. One of the first applications is on air-sea interactions (Section 3.2), with a comprehensive analysis of the climatological annual and seasonal mean heat, mass, and buoyancy fluxes over the Aegean for the period 1985–2015.

For the first time, the diverse role of the Black Sea waters outflow as a moderator of the buoyancy loss of the basin has been revealed: The thin surface layer of modified Black Sea waters flowing into the Aegean Sea acts as an effective insulator regarding dense-water formation processes, by restricting air-sea energy exchanges. These waters also act (a) as a moderator of buoyancy fluxes over their trajectory and (b) as a provider of significant lateral buoyancy to the basin, thus making it very sensitive to meteorological forcing.

The climatological mean buoyancy loss averaged over the whole Aegean, has been estimated through this study to be  $9.1 \times 10^{-6} \text{ kg m}^{-1} \text{ s}^{-3}$ . However, if the Black Sea water inflow was absent, the buoyancy loss would correspond to the high values observed over the Eastern Aegean, an area not directly affected by the presence of Black Sea waters, i.e. about  $30 \times 10^{-6} \text{ kg m}^{-1} \text{ s}^{-3}$  (Fig. 3.25). The surface heat loss over the Aegean is much higher than all neighboring seas (Table 3.4), including the Adriatic –the dominant dense-water formation site for the Eastern Mediterranean. Due to the aforementioned effects that the Dardanelles outflow exert on the Aegean Sea buoyancy budget, it becomes evident that an improvement on the description of the exchange at the Dardanelles-Marmara Sea-Bosphorus strait system, can greatly enhance the realism of the basin's variability as a dense-water exporter to the Eastern Mediterranean.

Furthermore, the spatiotemporal analysis performed through Principal Component Analysis, shows that the Aegean Sea hosts the greatest variability of surface buoyancy fluxes, for all the first five modes which explain ~98% of the total buoyancy flux of the entire Eastern Mediterranean – Black Sea system.

Extreme events like heatwaves are projected to become more frequent in a changing climate. Especially in the Eastern Mediterranean these events are progressively less studied as one moves from the atmospheric realm, to the ocean realm, and even more so when considering co-occurring marine-atmosphere events and possible air-sea interactions.

Marine heatwaves in the Eastern Mediterranean Sea have been gaining attention, however, the spatial relations of their occurrence has not been equally explored. The analysis performed in this study, shows that the most frequently occurring events are found in the northern and northwestern Aegean, while the longer lasting ones in the southern and south-eastern part. The intensity of such events increases at regions of

increased temperature variability, showcasing once more the important role of the Dardanelles inflow in affecting the climate of the Aegean Sea. A heatwave ecosystem stress index is introduced by combining marine heatwave metrics, as a method of identifying regions of increased mortality or stress on local species. Nevertheless, larger spatiotemporal coverage is needed on ecosystem status data, in order to calibrate the algorithm.

Hints on the interaction between the atmosphere and the ocean can already be seen by examining temperature anomalies in the two domains, during case examples of marine heatwaves. The important role of the Dardanelles inflow is once again demonstrated. Moreover, it is argued that the local warming trend of sea surface temperatures biases the occurrence of MHWs towards the end of the period under consideration. Local trends are calculated for the Aegean Sea, and the spatial distribution of the temperature slope for both the atmosphere and the ocean show a warming trend of 1.7 to 2.2 times that of the global atmosphere/ocean.

Subsequently, the global trend is removed from the local trend and the surface heatflux anomalies are calculated during days with concurrent marine-atmosphere heatwaves, which shows that during concurrent heatwaves there is an excess of heat flow towards the ocean. Further clustering compares the events by season and by type of event, which reveals that during concurrent events the atmosphere and marine realms are receiving more heat input than they would have received, had they been under a standalone event. This is most prominent during the winter months and less prominent during the summer months.

# 5

## CONCLUSIONS

---

*“The time is gone, the song is over  
thought I’d something more to say“*

— Roger Waters, *Time*

There has been an increasing interest on studying the physical properties of the Mediterranean Sea, whether it is the circulation, thermohaline functioning and interactions with other basins (in a purely oceanographic sense), or the ocean interactions with the atmosphere and their interannual and seasonal variability and extremities (in a purely climatic sense). However, there has been a very important shortfall in the efforts of the scientific community in producing reliable climate projections of the marine circulation and physical characteristics of the Aegean Sea on time scales of decades. This involved the simulation of the Black Sea inflow, which was initially performed through parameterizations derived mainly from observations, but later also from simple theoretical estimates of the Mediterranean-Black Sea water exchange. The contribution of this exchange is of paramount importance in shaping the hydrographic characteristics and circulation of the Aegean Sea, as the incoming Black Sea waters have very different characteristics (namely, temperature and salinity) from those of the Mediterranean, and are much lighter, thus influencing the marine dynamics. In addition, the discovery in recent decades of some physical processes that are unique for the Eastern Mediterranean region and relevant to the aforementioned exchanges (e.g., EMT, BiOS, etc.), has supplied an additional need to study their underlying mechanisms in retrospect while also projecting possible changes within a changing climate.

Recognising the importance of including the interaction between the two seas, the scientific community has produced continuous improvements in the exchange parameters. These improvements, are considered adequate for use in numerical simulations of the circulation over parts of the historical period, or for operational forecasts. However, they are considered inappropriate for time periods in the order of decades, due to the gradual change in the characteristics of the two seas and consequently the exchanges between them. The production of reliable climate projections for the Aegean Sea therefore, required the full numerical simulation of the integrated Eastern Mediterranean – Black Sea system, with the Straits system of Dardanelles (or *Hellespont*), Sea of Marmara

(or *Propontis*) and Bosphorus fully integrated into the numerical grid, a task that had never been implemented before. The small dimensions of the above Straits (Dardanelles and Bosphorus) require a very high resolution for the numerical simulation of hydrodynamics and circulation within them. This is the main reason it has been so common for numerical simulations of the Aegean and Mediterranean sea circulation, to use parameterizations for the exchanges with the Black Sea.

Addressing the aforementioned issues formed the main motivation for the present study, which focused on the problem around two major axes of approach. The first is a technical approach, namely the creation of the necessary tool and validation of its performance, while the second is a descriptive/analytical approach, namely the application of the created tool in studying physical processes in the Aegean Sea.

For the first approach, an ocean numerical simulation setup that realistically replicates the physical oceanography of the Eastern Mediterranean and Black Seas incorporating their interconnected nature, was created. This tool produced a daily averaged, three-dimensional hindcast dataset covering the period from *January 1<sup>st</sup> 1985* to *December 31<sup>st</sup> 2014*, whose performance was hereby exhaustively validated against remote sensing data for the surface fields, modeling and oceanographic survey data for the three-dimensional datasets, observational/modeling data for the volumetric water exchanges at the straits, and qualitative comparison with known features in the region (i.e., vertical overturning circulation, cross-sections of T and S along the straits, general circulation). The validation process has led to an overall positive assessment for the model's performance (especially considering the absence of relaxation or data assimilation procedures), and the simulation results extend the possibilities for a more comprehensive climate study of the region.

In the second approach, analysis of the dataset produced by the numerical simulation is applied to study real physical processes in the Aegean Sea. Firstly, with respect to air-sea interactions and by studying the Black Sea waters inflow in the Mediterranean and their role in controlling the buoyancy fluxes of the Aegean Sea. For the first time, the diverse role of the Black Sea waters outflow as a moderator of the buoyancy loss of the basin has been revealed: The thin surface layer of modified Black Sea waters flowing into the Aegean Sea acts as an effective insulator regarding dense-water formation processes, by restricting air-sea energy exchanges. The improvement on the description of the exchange at the Dardanelles-Marmara Sea-Bosphorus strait system, can greatly enhance the realism of the Aegean Sea's variability as a dense-water exporter, as well as highlight the basin's behaviour as the major source of surface buoyancy flux variability in the Eastern Mediterranean. Secondly, with respect to extreme events in the region and especially marine and atmospheric heatwaves in the Aegean Sea. This is performed

by incorporating the use of data from a separate atmospheric model, and by investigating the statistics of these events and the direction of energy fluxes between the two domains during co-occurring heatwaves. In conclusion, there is a measurable reinforcement between the two domains during co-occurring events, when compared to stand-alone events in one domain or the other. However, further investigation is needed in order to quantify and explain this mechanism.

Both approaches concluded in fruitful results, and the initial goals of the study were met. The main innovations emerging from this study can be summarized in the following:

- a) A novel machine learning method was developed and adapted to the Black Sea catchment area, for the estimation of land runoff in past and future climates, using only precipitation, runoff and topographic data, with very satisfactory results.
- b) A single, variable resolution, coherent numerical grid interconnecting the Eastern Mediterranean and Black Seas, was developed, tested and applied for the first time in the region using the **ROMS** modelling system. In order to achieve the required spatial resolution for a realistic simulation of the exchange at the Dardanelles and Bosphorus straits, resolution was increased in these areas of high hydrodynamic demands, and decreased away from the areas of interest for higher computational efficiency.
- c) The validation of the thirty-year simulation used a particularly wide and complete set of observations of the marine environment, while the evaluation was not limited to the sea surface, but includes the interior of the sea column. The process concluded with very satisfactory results and realistic performance for the 30-year hindcast integration.
- d) The influence of the Dardanelles outflow on the modulation of atmospheric exchanges over the Aegean Sea was highlighted for the first time, and the diverse role of the Black Sea waters outflow as a moderator of buoyancy loss in the basin, has been revealed.
- e) The behaviour of the Aegean Sea acting as the host of the largest variability in surface buoyancy fluxes in the entire Eastern Mediterranean – Black Sea system has been revealed for the first time.
- f) A relatively large warming trend has been revealed for the Aegean Sea waters and overlaying atmosphere, during the 30-year period (being around two times that of the global average trend, both in the ocean and the atmosphere).
- g) Marine heatwaves were detected and analysed with relation to the existence of co-occurring atmospheric heatwaves for the first

time in the Mediterranean, and possible interactions between the two where studied formulating the hypothesis of a mechanism for reinforcement through heatfluxes. The first results support the proposed reinforcement mechanism, although the analysis is not complete yet.

The developed Eastern Mediterranean Black Sea System (**EMBS**) simulation represents a significant advancement in the available tool-set for climatological studies in the Eastern Mediterranean, with a particular emphasis on the Aegean Sea. This numerical simulation has enhanced the understanding of both the climatic variability of the region and the intricate hydrodynamic processes at play. By interconnecting the Black Sea with the Eastern Mediterranean within a single, coherent simulation environment, the **EMBS** simulation has successfully described both the complex exchange of water between these two domains and its properties, an aspect that was previously modeled with only a limited degree of realism.

The simulation has introduced substantial methodological advancements that include a unique grid construction method for the region, and minimal long-term drift despite the absence of data assimilation schemes. Specifically, the system described the water exchange at the straits of Dardanelles and Marmara with high accuracy, despite the use of a hydrostatic model. This stands in stark contrast to the simplifications often employed in previous studies, which tended to overlook the importance of including these critical region in the simulation. The model's performance demonstrated minimal numerical drift over an extended 30-year simulation period, which verifies its robustness and its capability to produce reliable long-term climatic projections without the need for assimilating observational data.

Compared to existing tools, the **EMBS** simulation provides a more reliable and detailed account of the climatology and physical oceanography of the region. While other models (like **ALERMO** or **MFS**, exhibit valuable insights into the Eastern Mediterranean's oceanographic conditions, **EMBS** incorporates a unique integration of the exchange with the Black Sea and a comprehensive validation against observational data. The simulation results, indicate an improvement in capturing average flows, interannual variability, and a robust representation of water mass distributions (including a more accurate distribution of deeper dense waters in the Aegean Sea). The representation of air-sea interactions, both on the energy fluxes domain, as well as on the atmospheric and marine heatwave occurrence, gave new insights on how the water exchange with the Black Sea can affect the climatic variability of conditions in the region, and highlighted one more time the importance of including the exchange in the modeling domain.

Future work, includes extending the hindcast analysis of buoyancy fluxes, as well as creating a better formulation of the co-occurring heatwave definition and detection methods, while also exploring further the possible reinforcing mechanisms between marine and atmospheric heatwaves. Additionally, the conditions of future climate scenarios are going to be configured in anticipation/preparation of extending this dataset into future projections.

## EPILOGUE

As a final reflection, not so much for it's scientific value but rather as a celebration of the captivating nature of oceanographic processes, Figure 5.1 is presented. A true-color image captured from the Moderate Resolution Imaging Spectroradiometer (**MODIS**) on NASA's Terra satellite over the eastern Mediterranean, shows part of the southern Black Sea, the Sea of Marmara and the central and northern Aegean Sea (Figure 5.1a). A high concentration of a substance is observed in the surface waters of the Sea of Marmara, which passing through the Dardanelles strait disperses and diffuses into the Aegean Sea. This substance could be either coccolithophores (i.e. a type of phytoplankton), calcium carbonate, elemental sulfur, sediments, or a combination of the above; the important factor is that it is changing the color of the surface waters, which produces this stunning result and acts as a tracer for the dispersal of Marmara Sea surface waters into the Aegean.

Within the **EMBS** simulation there are three tracers that could be used for the purpose of illustrating the surface Marmara Sea outflow into the Aegean; either sea surface temperature, sea surface density or sea surface salinity. Although they all have very different values between the Marmara Sea and the Aegean, the former two are more closely affected by air surface temperature, winds and heat-fluxes, making sea surface salinity the best candidate for the illustration. In order to produce Figure 5.1b, the sea surface salinity field of the same date as in the **MODIS** picture was used as a tracer of the Marmara Sea waters. A two-way-diverging color-map was constructed by using a "turquoise" color as a central value for the average surface salinity in the Marmara Sea (~20-21), which then diverges into two different dark blue colors, characteristic of the equivalent points in the southern Black Sea (~18) and the central Aegean Sea (~38). The specific color codes for all three control points were deduced from the satellite picture in order to obtain a similar looking result. The comparison showcases the high quality of the **EMBS** simulation performance, after almost 20 years of free run.

The physical phenomenon discussed above, stretches across the borders between physical, chemical and biological oceanography, and the comparison also involves geophysical fluid dynamics. Using creative methods for representing and illustrating some of these multidisciplinary

processes within numerical ocean simulations is a rewarding process, which does not serve as a desperate attempt to close the unbridgeable gap between real ocean and its artificial counterpart, but rather as an inventive viewpoint to marvel at the beauty of nature.



(a) True-color Terra MODIS picture (from [Visible Earth](#), NASA)



(b) [EMBS](#) Simulation surface field

Figure 5.1: Comparison of a true-color satellite picture taken on June 25 2003, with the surface field from [EMBS](#) simulation for the same day. In the satellite picture, high concentrations of a natural tracer (e.g. coccolithophores) that changes the color of the surface waters within the Sea of Marmara, is dispersing and diffusing into the Aegean Sea. In the [EMBS](#) simulation figure, the meticulous calibration of the color-map for the surface salinity field, reveals a similar pattern.







## ΕΚΤΕΝΗΣ ΠΕΡΙΛΗΨΗ ΣΤΑ ΕΛΛΗΝΙΚΑ (EXTENSIVE SUMMARY IN GREEK)

**ΣΥΝΟΨΗ:** Οι ανταλλαγές υδάτων μέσω στενών διαύλων είναι ένας αρκετά σημαντικός παράγοντας διαμόρφωσης της κυκλοφορίας και των υδρογραφικών χαρακτηριστικών γειτνιαζόντων θαλασσών λεκανών, ιδίως σε κλιματικές χρονικές κλίμακες. Ο κρίσιμος αυτός ρόλος της αλληλεπίδρασης μεταξύ της Μεσογείου και του Εύξεινου Πόντου συχνά παραβλέπεται σε αριθμητικές μελέτες υδροδυναμικών προσομοιώσεων του Αιγαίου, οι οποίες βασίζονται κυρίως σε παραμετροποιήσεις για την περιγραφή της ανταλλαγής υδάτων, μια πρακτική που οδηγεί στην ουσία σε υδροδυναμική αποσύνδεση των δύο λεκανών. Στην παρούσα μελέτη, το σύστημα Ανατολικής Μεσογείου-Εύξεινου Πόντου προσομοιώνεται για την ιστορική περίοδο (1985-2015) με πλήρη υδροδυναμική σύζευξη των δύο λεκανών, και με χωρική έμφαση του πλέγματος στο Αιγαίο Πέλαγος.

Για τον σκοπό αυτό, χρησιμοποιείται ένα υδροδυναμικό, πλήρως τρισδιάστατο σύστημα προσομοίωσης ακεανών (**ROMS**), με ρεαλιστικές οριακές συνθήκες (ακεανίες, ατμοσφαιρικές και υδρολογικές). Περιγράφεται διεξοδικά η διαμόρφωση της διάταξης προσομοίωσης και αξιολογείται επισταμένα η απόδοσή της κατά τα 30 έτη της ιστορικής περιόδου. Αυτό επιτυγχάνεται με σύγκριση των αποτελεσμάτων με παρατηρησιακά δεδομένα αλλά και αποτελέσματα άλλων προσομοιώσεων, αξιολογώντας την ορθή αναπαράσταση των επιφανειακών πεδίων, της κυκλοφορίας, των τρισδιάστατων υδρογραφικών χαρακτηριστικών, των ογκομετρικών ανταλλαγών νερού και της χωροχρονικής μεταβλητότητας των παραπάνω.

Η σύγκριση δείχνει σημαντική βελτίωση σε σύγκριση με μελέτες μοντελοποίησης που δεν περιλαμβάνουν την αλληλεπίδραση με τον Εύξεινο Πόντο, καθώς και αξιόπιστη αναπαραγωγή της μεταβλητότητας του συστήματος σε χρονικές κλίμακες που κυμαίνονται από ημερήσιες έως εποχικές και δεκαετείς. Επίσης διαφαίνεται αρκετά ακριβής αναπαραγωγή των μέσων γραμμικών τάσεων μεταβολής των χαρακτηριστικών της λεκάνης, για την περίοδο αυτή των 30 ετών. Επιπλέον, λόγω της διαμόρφωσης της προσομοίωσης για ελεύθερο τρέξιμο (δηλαδή της απουσίας μεθόδων αφομοίωσης παρατηρησιακών δεδομένων), δεν απαιτούνται επιπλέον δεδομένα κατά το τρέξιμο του ομοιώματος, γεγονός που καθιστά δυνατή την αξιόπιστη επέκταση της ίδιας διάταξης για σενάρια όπου δεν υπάρχουν διαθέσιμα δεδομένα παρατήρησης, όπως για παράδειγμα σε μελλοντικές προβλέψεις.

Τέλος, τα αποτελέσματα της προσομοίωσης αξιολογούνται σε επίπεδο φυσικών διεργασιών. Η ανάλυση των ογκομετρικών ροών νερού, και των

ροών θερμότητας και πλευστότητας στο Αιγαίο Πέλαγος καταδεικνύει τη σημαντικότητα της επίδρασης της εισροής από τα Δαρδανέλια, στη θερμόαλη λειτουργία της λεκάνης και την ιδιαίτερη συμπεριφορά της ως περιοχής με τη μεγαλύτερη μεταβλητότητα των ροών πλευστότητας στην Ανατολική Μεσόγειο. Επιπροσθέτως, εξετάζεται η εμφάνιση θαλάσσιων και ατμοσφαιρικών καισώνων στην περιοχή σε μια προσπάθεια να εντοπιστεί αν υφίσταται μηχανισμός ανάδρασης/αλληλοενίσχυσης μεταξύ ατμοσφαιρικών και θαλασσίων καισώνων, με τα πρώτα αποτελέσματα να υποστηρίζουν την ύπαρξη ενός τέτοιου μηχανισμού.

## ΕΙΣΑΓΩΓΗ

### *Περιγραφή του Θέματος*

Η Μεσόγειος και ο Εύξεινος Πόντος είναι δύο γειτνιάζουσες και επικοινωνούσες θαλάσσιες λεκάνες με αντιθετική λειτουργία και θερμόαλη κυκλοφορία. Η Μεσόγειος εξάγει πυκνό νερό, ενώ ο Εύξεινος Πόντος εξάγει ελαφρύ, υφάλμυρο νερό. Η ανταλλαγή υδάτων μέσω των Στενών του Βοσπόρου, της Θάλασσας του Μαρμαρά και των Στενών των Δαρδανελίων είναι καθοριστικής σημασίας για τον προσδιορισμό των ωκεανογραφικών χαρακτηριστικών της Μεσογείου, ενώ παράλληλα ρυθμίζει το ισοζύγιο της πλευστότητας του Αιγαίου Πελάγους καθώς και την κυκλοφορία ανατροπής.

Το Βόρειο Αιγαίο Πέλαγος (παρότι δέχεται είσοδο πλευστότητας από τον Εύξεινο Πόντο) έχει αναφερθεί ως η περιοχή που πυροδότησε το λεγόμενο Μεταβατικό συμβάν της Ανατολικής Μεσογείου (Eastern Mediterranean Transient (**EMT**)). Αφενός, ο ρόλος της εισροής μειωμένης πλευστότητας μέσω των Δαρδανελίων ως έναυσμα του **EMT** έχει αμφισβητηθεί, παρόλα αυτά υπάρχει η ανάγκη για ορθότερη αναπαράσταση της ανταλλαγής υδάτων με τον Εύξεινο Πόντο μέσω του συστήματος των στενών Βοσπόρου-Δαρδανελλίων (**BMD**) για την ακριβή αναπαραγωγή της κατακόρυφης δομής της στήλης νερού στο Βόρειο και Κεντρικό Αιγαίο Πέλαγος. Στις υπάρχουσες υδροδυναμικές προσομοιώσεις για το Βόρειο Αιγαίο, αυτή η ανταλλαγή υδάτων περιγράφεται είτε με χρήση παραμετροποιήσεων του επιχιακού κύκλου της ανταλλαγής, είτε με έμμεσο τρόπο υπολογίζοντας το ισοζυγίου νερού του Εύξεινου Πόντου. Η υπάρχουσα βιβλιογραφία σχετικά με τις αριθμητικές μελέτες που προσομοιώνουν τις διασυνδεδεμένες λεκάνες Ανατολικής Μεσογείου-Εύξεινου Πόντου μπορεί να θεματοποιηθεί σε δύο κατηγορίες με βάση τη χωροχρονική έκταση και την ανάλυση. Στη μία κατηγορία, εμπίπτουν μελέτες που επικεντρώνονται κυρίως στην προσομοίωση της ανταλλαγής και της υδροδυναμικής στα στενά, μη συμπεριλαμβάνοντας την ευρύτερη περιοχή. Η δεύτερη κατηγορία περιλαμβάνει μελέτες που προσομοιώνουν μόνο ένα μέρος του συστήματος σε κλιματικές κλίμακες (δεκαετίες ή έτη) είτε για την ιστορική περίοδο, είτε ως μελλοντική προβολή, είτε και τα δύο. Οι μελέτες αυτές προσομοιώνουν

τη Μεσόγειο Θάλασσα για μεγαλύτερες χρονικές περιόδους και χρησιμοποιούν παραμετροποιήσεις για τις ανταλλαγές στα Δαρδανέλια και τα στενά του Βοσπόρου αντί για αριθμητική επίλυση της υδροδυναμικής και της ροής.

### *Προπαρασκευαστικές Ενέργειες*

Αρχικά η μελέτη αυτή είχε ως στόχο να εκτιμήσει την εκροή νερού από τον Εύξεινο Πόντο στο Αιγαίο Πέλαγος χρησιμοποιώντας μεθόδους διατήρησης της μάζας. Ωστόσο, για να πραγματοποιηθεί κάτι τέτοιο απαιτούνταν μεταξύ άλλων και δεδομένα ποτάμιας εκροής στον Εύξεινο Πόντο. Το μόνο γνωστό συνεχές σύνολο δεδομένων για την απορροή ποταμών όταν ξεκίνησε η μελέτη, παρεχόταν από το Σουηδικό Μετεωρολογικό και Υδρολογικό Ινστιτούτο (**SMHI**), το οποίο όμως δεν κάλυπτε ολόκληρη την ιστορική περίοδο (1985 - 2015), αλλά ούτε μελλοντικές περιόδους και κλιματικά σενάρια. Έτσι, η εκροή έπρεπε να υπολογιστεί εμμέσως, συσχετίζοντας την ποτάμια εκροή με την βροχόπτωση στην λεκάνη απορροής του Εύξεινου Πόντου (για την οποία υπήρχαν δεδομένα). Για τον σκοπό αυτό έγινε χρήση τεχνητής νοημοσύνης και εκπαιδεύτηκε ένα σύνολο νευρωνικών δικτύων για την αναπαραγωγή της μη γραμμικής αυτής σχέσης. Αυτή η διαδικασία εκπαιδεύσης έκανε χρήση ημερησίων δεδομένων βροχόπτωσης από το 1981 έως το 2006 και εκροής ποταμών. Το 5% των αποδοτικότερων από τα εκπαιδευμένα νευρωνικά δίκτυα επιλέχθηκαν για τον τελικό υπολογισμό (με βάση το ποσοστό επιτυχίας της εκπαίδευσης σε γνωστές τιμές εισόδου). Με αυτόν τον τρόπο δημιουργήθηκε ένα εργαλείο που μπορούσε να υπολογίσει την ποτάμια εκροή στον Εύξεινο Πόντο όχι μόνο για την ιστορική περίοδο, αλλά και για διάφορα μελλοντικά κλιματικά σενάρια (εφόσον υπάρχουν διαθέσιμα τα δεδομένα βροχόπτωσης).

Η μέθοδος αυτή αποσκοπούσε στη βελτίωση των υπολογισμών του ισοζυγίου νερού του Εύξεινου Πόντου, η οποία θα μπορούσε στην συνέχεια να χρησιμοποιηθεί για τον υπολογισμό της ανταλλαγής υδάτων με το Αιγαίο Πέλαγος και κυρίως της υπερετήσιας και εποχικής μεταβλητότητας αυτής. Παρά τα πολλά υποσχόμενα αποτελέσματα της μεθόδου, σύντομα μετά την ολοκλήρωση της μελέτης δημοσιεύτηκαν τα ημερήσια δεδομένα ποτάμιας απορροής από το υδρολογικό μοντέλο **HYPE** για ολόκληρη την ευρωπαϊκή ήπειρο και τον Εύξεινο Πόντο, συμπεριλαμβανομένων των μελλοντικών προβλέψεων για τρία σενάρια εκπομπών (RCP) έως το 2100, γεγονός που κατέστησε τη μέθοδο υπολογισμού με χρήση τεχνητής νοημοσύνης παρωχημένη. Αυτό το νέο σύνολο δεδομένων άνοιξε νέες δυνατότητες για τη προσομοίωση του Εύξεινου Πόντου και στο σημείο αυτό αποφασίστηκε η αλλαγή της ερευνητικής στρατηγικής.

Αποφασίστηκε η χρήση των παραπάνω δεδομένων ως οριακές συνθήκες σε ένα σύστημα προσομοίωσης που θα περιέχει ολόκληρο το σύστημα Εύξεινου Πόντου - ανατολικής Μεσογείου ως διασυνδεδεμένου ωκεανογραφικού συστήματος, όμως η ανάγκη χρήσης πλεγμάτων πολύ υψηλής ανάλυ-

σης για την επίλυση της ροής στα στενά αυξάνει το αριθμητικό κόστος και καθιστά τέτοιες προσεγγίσεις απαγορευτικές για μακροπρόθεσμες προσομοιώσεις. Για να αντιμετωπιστεί αυτό το ζήτημα, αποφασίστηκε να γίνει κατάλληλη διαμόρφωση του υπολογιστικού πλέγματος, με μεταβλητή ανάλυση, ώστε να επιλύει μεν την υδροδυναμική των στενών με σχετικά υψηλή ανάλυση, αλλά να αυξάνει το μέγεθος των κελιών σε περιοχές όπου δεν υπάρχουν υψηλές ανάγκες και έτοι να μειώνει το υπολογιστικό κόστος.

Ο πρωταρχικός στόχος αυτής της εργασίας είναι η δημιουργία μιας βάσης τρισδιάστατων ωκεανογραφικών δεδομένων για την λεπτομερέστερη μελέτη των πολύτιλοκων φυσικών διεργασιών στην περιοχή, αλλά και την κατανόηση της μακροπρόθεσμης κλιματικής μεταβλητότητας αυτών των διεργασιών. Η κύρια πρόκληση είναι η ακριβής αναπαραγωγή της δυναμικής που είναι κρίσιμη για την ωκεανογραφία των λεκανών της Μεσογείου και του Εύξεινου Πόντου σε μακροπρόθεσμα κλιματικά τρεξίματα (άνω της τριακονταετίας), διατηρώντας παράλληλα το καινοτόμο μέρος της μελέτης: μια φυσική σύνδεση μεταξύ των δύο συστημάτων μέσω ενός συστήματος στενών πορθμών και ενδιάμεσων θαλασσών.

Τα καινοτόμα στοιχεία της μελέτης αυτής προκύπτουν τόσο από τη μεθοδολογική προσέγγιση όσο και από τις εφαρμογές του παραχθέντος εργαλείου στην ανάλυση φυσικών προβλημάτων (π.χ. ροές πλευστότητας και ενέργειας, θαλάσσιοι καύσωνες στο Αιγαίο Πέλαγος κλπ.). Μια σημαντική καινοτομία είναι η ανάπτυξη ενός ενιαίου, συνεχούς υπολογιστικού πλέγματος με μεταβλητή ανάλυση, το οποίο είναι απαραίτητο για την ταυτόχρονη προσομοίωση της δυναμικής τόσο στους στενούς διαύλους όσο και στις ανοικτές θάλασσες.

## ΜΕΘΟΔΟΛΟΓΙΑ

### *Αριθμητική Προσομοίωση*

Για την προσομοίωση αυτή επιλέχθηκε το σύστημα ωκεάνιας μοντελοποίησης **ROMS** για την μελέτη των φυσικών χαρακτηριστικών του Αιγαίου Πελάγους και της υπερετήσιας κλιματικής μεταβλητότητάς τους, καθώς και των πιθανών αλλαγών εντός ενός μεταβαλλόμενου κλιματικού συστήματος. Η διαμόρφωση του μοντέλου αποσκοπούσε στην ανάπτυξη ενός προϊόντος που θα μπορούσε να χρησιμοποιηθεί για προσομοιώσεις μακράς (υπερδεκαετούς) κλίμακας χωρίς την ανάγκη διορθωτικών παρεμβάσεων, που δεν θα απαιτεί ωκεάνιες οριακές συνθήκες υψηλής συχνότητας, και δεν θα είναι υπερβολικά απαιτητικό σε υπολογιστικούς πόρους.

Η περιοχή προσομοίωσης καθορίστηκε από την ανάγκη δυναμικής αναπαραγωγής πιθανών μελλοντικών αλλαγών στην αλληλεπίδραση μεταξύ του Αιγαίου και του Εύξεινου Πόντου ή της μεταβλητότητας αυτής. Για να επιτευχθεί αυτό, απαιτούνταν μια ακριβής αναπαραγωγή των ιδιοτήτων του νερού των δύο λεκανών, κάπι το οποίο μπορεί να επιτευχθεί μόνο μέσω της ακριβούς αναπαραγωγής της ανταλλαγής υδάτων. Το ανοιχτό

όριο τοποθετήθηκε στην Τυρρηνική Θάλασσα αφενός για την αποφυγή υπολογιστικού θορύβου στο Αιγαίο από τις οριακές συνθήκες, αφετέρου για την κάλυψη μεγαλύτερου εύρους διεργασιών.

Το πλέγμα κατασκευάστηκε με καμπυλόγραμμη γεωμετρία συντεταγμένων και μεταβλητό μέγεθος για να περιγράψει καλύτερα την δαιδαλώδη ακτογραμμή των λεκανών της ανατολικής Μεσογείου/Εύξεινου Πόντου. Η πυκνότητα των γραμμών του πλέγματος κυμαίνεται από περίπου 5-7 χιλιόμετρα σε περιοχές με χαμηλότερες υδροδυναμικές απαιτήσεις, έως περίπου 1,2 χλμ. στα στενά, με μέσο μέγεθος 3 χλμ. για ολόκληρη την περιοχή προσομοίωσης.

Διερευνήθηκαν τρεις διαφορετικές διαμορφώσεις για την προσομοίωση με 25, 30 και 35 κατακόρυφα στρώματα. Η πρώτη διαμόρφωση έδειξε περιστασιακές αριθμητικές αισθήσεις που προέρχονταν από το σύστημα των στενών, ενώ η δεύτερη διαμόρφωση δεν παρείχε μετρήσιμη βελτίωση στην απόδοση σε σύγκριση με τη διαμόρφωση 30 στρωμάτων. Η διαμόρφωση με 30 στρώματα συντεταγμένων μεταβλητής ανάλυσης υιοθετήθηκε για την περιοχή ενδιαφέροντος.

Στη μελέτη χρησιμοποιήθηκε ένας συνδυασμός οριακών συνθηκών για το ανοικτό πλευρικό όριο στα δυτικά, συμπεριλαμβανομένων των οριακών συνθηκών Chapman για το ύψος στάθμης της ελεύθερης επιφάνειας, μιας προσαρμοστικής συνθήκης για τα τρισδιάστατα πεδία ταχυτήτων θερμοκρασίας και αλατότητας (radiation-nudging), και της συνθήκης Shcheretkin για το βαροτροπικό πεδίο ταχυτήτων. Η Αζοφική Θάλασσα συμπεριλήφθηκε στο πλέγμα για να παρέχει μια πιο ρεαλιστική αναπαράσταση των χαρακτηριστικών του νερού που εξέρχεται από τον πορθμό του Κέρτσ.

Η προσομοίωση ξεκίνησε από την 1η Ιανουαρίου 1985 και διήρκεσε έως την 31η Δεκεμβρίου 2014 (30 έτη). Η καταγραφή των εξαγόμενων δεδομένων από το μοντέλο περιελάμβανε ημερήσιους μέσους όρους για διάφορες μεταβλητές, όπως θερμοκρασία, αλατότητα, βαροτροπικά και τρισδιάστατα πεδία ταχύτητας, πυκνότητα, ροές θερμότητας και ροές ενέργειας. Η προσομοίωση σχεδιάστηκε έτσι ώστε να είναι όσο το δυνατόν πιο κοντά σε ρεαλιστικές συνθήκες, να μπορεί να χρησιμοποιηθεί για κλιματική ανάλυση και να αναπαράγει την κλιματική μεταβλητότητα των χαρακτηριστικών του νερού και των παράγωγων φυσικών παραμέτρων της ωκεανογραφίας της περιοχής. Το βαροκλινικό χρονικό βήμα της προσομοίωσης είναι 60 δευτερόλεπτα, με τρία ενδιάμεσα βαροτροπικά βήματα (ανά 20 δευτερόλεπτα).

Η προσομοίωση εκτελέστηκε υπό ρεαλιστικό ατμοσφαιρικό εξαναγκασμό στην επιφάνεια (forcing), με χρήση δεδομένων από το **ECMWF-ERA** reanalysis, με χρονική ανάλυση 3 ωρών και χωρική ανάλυση  $0,125^\circ \times 0,125^\circ$ . Η μικρού μήκους κύματος ακτινοβολία κατανέμεται μεταξύ των επιφανειακών/ανώτερων στρωμάτων χρησιμοποιώντας μια συνάρτηση απορρόφησης που εξαρτάται από τις οπικές ιδιότητες του νερού ακολουθώντας συγκεκριμένους τύπους νερού κατά Jerlov, ανάλογα με την γεωγραφική θέση.

Η μελέτη υπολογίζει τις πλευρικές οριακές συνθήκες για την αλατότητα, τη θερμοκρασία, το ύψος της επιφάνειας της θάλασσας και το πεδίο ταχύτητας στο δυτικό όριο χρησιμοποιώντας τους ημερήσιους μέσους όρους του συστήματος πρόγνωσης **MFS**, το οποίο καλύπτει την περίοδο από τον Ιανουάριο του 1985 έως τον Δεκέμβριο του 2014. Στην προσομοίωση συμπεριλήφθηκαν εννέα μεγάλοι ποταμοί με τις μεγαλύτερες μέσες ογκομετρικές ροές (Δούναβης, Δνείπερος, Δνείστερος, Κουμπάν, Ντον, Άλυς, Σαγγάριος, Νείλος, Πάδος/Αδίγης). Η αλατότητα όλων των ποτάμιων υδάτων που εισέρχονται στο πλέγμα έχει οριστεί σε σταθερή τιμή 5‰, η οποία πέρα από ρεαλιστική, συμβάλλει και στην αποφυγή αριθμητικών ασταθειών.

### *Ορισμοί και Προετοιμασία*

Για την επικύρωση της επίδοσης της προσομοίωσης πραγματοποιήθηκε σύγκριση των αποτελεσμάτων με παρατηρησιακά δεδομένα (είτε επιτόπια, είτε από τηλεπισκόπιση), αλλά και με προϊόντα μετα-αναλύσεων. Πιο συγκεκριμένα, χρησιμοποιήθηκαν δεδομένα θαλάσσιας επιφανειακής θερμοκρασίας (**SST**) από το **CMEMS** για την Μεσόγειο και τον Εύξεινο Πόντο. Η σύγκριση της επιφανειακής στάθμης της θάλασσας, έγινε με δεδομένα αλτιμετρίας (**AVISO**) μετά από διγραμμική παρεμβολή του πλέγματος της προσομοίωσης **EMBS** στο δορυφορικό πλέγμα (regridding), και τον υπολογισμό μηνιαίων μέσων τιμών. Η επικύρωση της προσομοιωμένης ογκομετρικής ανταλλαγής νερού μέσω των στενών πραγματοποιείται με τη χρήση δύο συνόλων δεδομένων· μια χρονοσειρά από παρατηρησιακά δεδομένα της ροής για το στενό των Δαρδανελίων διάρκειας ενός έτους, και μια χρονοσειρά από το μοντέλο Maderich για την ροή στα στενά των Δαρδανελίων και του Βοσπόρου διάρκειας 25 ετών.

Για την επικύρωση των υδροδυναμικών δεδομένων, πρέπει να εξεταστεί ολόκληρη η τρισδιάστατη περιοχή μελέτης. Για αυτό τον σκοπό χρησιμοποιήθηκαν σύνολα δεδομένων από επιτόπιες ωκεανογραφικές αποστολές που περιγράφουν τη θερμοκρασία και την αλατότητα εντός της υδάτινης στάλης και παρέχονται μέσω των βάσεων δεδομένων MEDAR/MEDATLAS II και Sea-DataNet II, οι οποίες περιέχουν μια ολοκληρωμένη συλλογή όλων των διαθέσιμων σταθμών κατακόρυφων προφίλ, που έχουν κατά καιρούς πραγματοποιηθεί στην Μεσόγειο και τον Εύξεινο Πόντο.

Για την επικύρωση συμπεριλήφθηκε σύγκριση με γνωστά επιχειρησιακά συστήματα πρόγνωσης στη Μεσόγειο και τον Εύξεινο Πόντο (μοντέλα), τα οποία λόγω της χρήσης μεθόδων αφομοίωσης (assimilation) με κατά τα άλλα παρόμοια διαμόρφωση, χρησιμεύουν ως ένα μέτρο του ανώτατου ορίου απόδοσης για μια προσομοίωση όπως το **EMBS**. Για το σκοπό αυτό χρησιμοποιήθηκαν οι συνιστώσες της φυσικής ανάλυσης από το **MFS** για την Μεσόγειο και από το **BSMFC** για τον Εύξεινο Πόντο.

Επιπλέον, γίνεται ανάλυση των επιφανειακών ροών θερμότητας, αλλά και των ροών πλευστότητας δια της επιφάνειας και δια του στενού των

Δαρδανελίων (μεταφορά πλευστότητας) στο Αιγαίο Πέλαγος. Οι ροές θερμότητας υπολογίζονται από την προσομοίωση **EMBS**, ενώ οι ροές πλευστότητας υπολογίζονται έμμεσα από τις παραπάνω ροές, την αλατότητα, την εξάτμιση και τον ιετό.

Τα τελευταία 20-30 χρόνια, υπάρχει αυξανόμενο ενδιαφέρον για τη μελέτη των κυμάτων καύσωνα, ιδίως εκείνων που αφορούν εξαιρετικά ακραίες θερμοκρασιακές ανωμαλίες, κάτι που ενισχύθηκε μετά τον καταστροφικό καύσωνα του 2003 στην κεντρική Ευρώπη. Η κατανόηση των υποκείμενων μηχανισμών αυτών των ακραίων φαινομένων είναι υψίστης σημασίας για την πρόγνωση και τον μετριασμό των συνεπειών τους, κυρίως επειδή η συχνότητα και η έντασή τους προβάλλεται να αυξάνει στο μέλλον.

Οι καύσωνες από στατιστικής άποψης είναι γεγονότα που περιγράφουν τις ανώτερες ακραίες τιμές στην κατανομή της θερμοκρασίας εντός μιας συγκεκριμένης περιόδου, και έχουν έντονη επίδραση στο οικοσύστημα λόγω της πίεσης που μπορούν να ασκήσουν στη βιόσφαιρα. Ο ορισμός και η ανίχνευση αυτών των φαινομένων γίνεται συνήθως με τη χρήση στατιστικής προσέγγισης σε χρονοσειρές επιφανειακής θερμοκρασίας (και όχι μόνο). Οι μετεωρολογικοί οργανισμοί έχουν θεσπίσει τους δικούς τους ορισμούς, με τον Παγκόσμιο Μετεωρολογικό Οργανισμό να ορίζει ως καύσωνα πέντε ή περισσότερες διαδοχικές ημέρες παρατεταμένης ζέστης κατά τις οποίες η ημερήσια μέγιστη θερμοκρασία είναι υψηλότερη -κατά  $5^{\circ}\text{C}$  ή περισσότερο- από τον μέσο όρο των μέγιστων θερμοκρασιών της περιόδου 1961-1990. Τα τελευταία χρόνια, επιπλέον μελέτες και πρωτοβουλίες έχουν προσπαθήσει να εισάγουν έναν πιο οικουμενικό/καθολικό ορισμό του καύσωνα, που θα βασίζεται σε στατιστικά κριτήρια τα οποία θα ξεπερνάνε τις ιδιαιτερότητες του κάθε γεωγραφικού τόπου, και έτσι θα μπορεί να εφαρμόζεται σε παγκόσμια κλίμακα. Η παρούσα μελέτη χρησιμοποιεί τον ορισμό των Hobday et al., 2016 για την ανίχνευση τόσο των ατμοσφαιρικών όσο και των θαλασσιών κυμάτων καύσωνα, χρησιμοποιώντας διαφορετικές τιμές κατωφλίου και διάρκειας για θάλασσα και ατμόσφαιρα.

Η παρούσα μελέτη επικεντρώνεται στην ανίχνευση ατμοσφαιρικών και θαλασσιών καυσώνων, της συσχέτισης μεταξύ των δύο και της κοινής τους εμφάνισης, εξετάζοντας ταυτόχρονα την κατεύθυνση της αλληλεπίδρασης μεταξύ των δύο πεδίων (ατμόσφαιρας και θάλασσας) μέσω ανάλυσης των επιφανειακών ροών θερμότητας που προκύπτουν από την προσομοίωση **EMBS**. Η θερμοκρασία στο επιφανειακό στρώμα της θάλασσας μπορεί να μεταβληθεί σε τοπικό επίπεδο μέσω της πλευρικής μεταφοράς θερμότητας από τη γενική κυκλοφορία και την κατακόρυφη εισροή/εκροή θερμότητας δια της επιφάνειας της θάλασσας. Η ολική ροή θερμότητας στην επιφάνεια της θάλασσας είναι γενικά θετική κατά τους εαρινούς και θερινούς μήνες και αρνητική κατά τους φθινοπωρινούς και χειμερινούς μήνες. Στην παρούσα ανάλυση για την σύγκριση/συσχέτιση χρησιμοποιούνται δεδομένα ατμοσφαιρικής θερμοκρασίας από το ατμοσφαιρικό μοντέλο **CCLM**,

το οποίο διαμορφώθηκε με κοινές οριακές συνθήκες με την προσομοίωση **EMBS**, παρουσιάζονται τα αποτελέσματα τόσο της ανίχνευσης όσο και ανάλυση της συν-εμφάνισης των ατμοσφαιρικών και θαλασσίων καυσώνων, και περιγράφεται η προσοχή που πρέπει να δίνεται στον καθορισμό των σχέσεων αιτίου-αποτελέσματος στην παραπάνω διαδικασία.

## ΑΠΟΤΕΛΕΣΜΑΤΑ & ΣΥΖΗΤΗΣΗ

### *Επικύρωση της Προσομοίωσης*

Η απόδοση της προσομοίωσης **EMBS** επικυρώνεται σε επιμέρους στάδια που περιλαμβάνουν: (α) επικύρωση των επιφανειακών πεδίων έναντι δορυφορικών παρατηρήσεων, (β) συγκρίσεις χρονοσειρών ογκομετρικής ανταλλαγής νερού, (γ) την γενική κυκλοφορία, (δ) κατακόρυφα προφίλ της στήλης ύδατος, και (ε) την δυνατότητα αναπαραγωγής των ιδιοτήτων των βαθιών λεκανών (πυκνού νερού). Η προσομοίωση αναπαράγει τα περισσότερα γνωστά επιφανειακά ρεύματα, τους στροβίλους και τις χαρακτηριστικές δομές μέσης κλίμακας, με κάποιες αποκλίσεις στη Λεβαντίνη και στο νότιο Ιόνιο Πέλαγος. Τα στενά του Βοσπόρου και των Δαρδανελίων αποτελούν σημεία ελέγχου της ροής όπως προκύπτει από τον υπολογισμό των σύνθετων αριθμών Froude. Η εποχική μεταβλητότητα της ροής στα δύο στενά υποδηλώνει ότι η ύπαρξη υδραυλικού ελέγχου φαίνεται να εξαρτάται από τη ροή του ανώτερου στρώματος, είτε μέσω της αύξησης στην ταχύτητά του, είτε μέσω της μείωσης του πάχους του ανώτερου στρώματος.

Η προσομοίωση **EMBS** αναπαράγει τις ογκομετρικές ανταλλαγές νερού στα στενά του Βοσπόρου και των Δαρδανελίων, παρουσιάζοντας αντίστοιχη μεταβλητότητα με τις παρατηρήσεις. Το εύρος των τιμών ροής στο ανώτερο και κατώτερο στρώμα σε σχέση με την ολική ροή είναι μεγαλύτερο στα Δαρδανέλια από ότι στα στενά του Βοσπόρου. Η ανάλυση δείχνει επίσης ότι οι ροές του ανώτερου στρώματος είναι υψηλότερες στην προσομοίωση **EMBS** από ότι στο μοντέλο των Maderich et al. και οι ροές του κατώτερου στρώματος είναι συγκρίσιμες ή ελαφρώς χαμηλότερες στο **EMBS** (κάτι που συνιστά βελτίωση σε σύγκριση με τις παρατηρήσεις). Η προσομοιωμένη χρονική εξέλιξη των χαρακτηριστικών του νερού κατά μήκος του συστήματος Βοσπόρου - Δαρδανελίων και η εποχική διακύμανση αυτών συγκρίνεται ικανοποιητικά με δεδομένα επιτόπιων παρατηρήσεων. Η προσομοίωση αναπαράγει ρεαλιστικά την γενική κυκλοφορία και τη θερμοάλη κυκλοφορία του συστήματος της ανατολικής Μεσογείου και του Εύξεινου Πόντου και την διακύμανση αυτών, ενώ υπερεκτιμά συστηματικά τόσο την αλατότητα όσο και τη θερμοκρασία της στήλης σχεδόν σε ολόκληρη την περιοχή μελέτης, παρόλα αυτά το σφάλμα και η τετραγωνική απόκλιση σφάλματος παραμένουν αρκετά χαμηλά.

Η απόδοση της προσομοίωσης **EMBS** είναι συγκρίσιμη με το επιχειρησιακό σύστημα προγνώσεων **MFS**, ιδίως όσον αφορά την αναπαραγωγή των κατακόρυφων δομών της υδάτινης στήλης και της πυκνότητας. Η λε-

κάνη της Λεβαντίνης, το Ιόνιο Πέλαγος, η Αδριατική και ο Εύξεινος Πόντος παρουσιάζουν παρόμοια εικόνα στις δύο προσομοιώσεις, με υψηλότερες τιμές επιφανειακής αλατότητας λόγω της αυξημένης εξάτμισης. Η επιφανειακή αλατότητα του **EMBS** τόσο στην Αδριατική όσο και στον Εύξεινο Πόντο παρουσιάζει υπερεκτίμηση, πιθανώς λόγω της παράλειψης των μικρών ποταμών. Η προσομοίωση αναπαράγει τα γεγονότα σχηματισμού πυκνών υδάτων στο Αιγαίο Πέλαγος, πράγμα που επικυρώνει την απόδοσή της όσον αφορά τους μηχανισμούς που επηρεάζουν ολόκληρη τη στήλη νερού και την θερμόαλη κυκλοφορία. Η προσομοίωση αναπαράγει επίσης τη πολυετή μεταβλητότητα διαδικασιών όπως ο σχηματισμός πυκνού νερού στις βαθιές λεκάνες και η ανάμιξη κατά τη διάρκεια των περιόδων στασιμότητας (stagnation periods). Η σταθερά υψηλή πυκνότητα στα βαθιά νερά του Αιγαίου στην προσομοίωση **MFS** έρχεται σε αντίθεση με την εξέλιξη του αντίστοιχου πεδίου στην προσομοίωση **EMBS**, υποδηλώνοντας μια πιο ρεαλιστική παραμετροποίηση της κατακόρυφης ανάμιξης και μεταφοράς στην δεύτερη περίπτωση.

### *Εφαρμογές*

Μετά την επικύρωση της ποιότητας της προσομοίωσης, η ανάλυση επικεντρώνεται σε γνωστές φυσικές διεργασίες στην περιοχή μελέτης προκειμένου να διαπιστωθεί η ικανότητα αναπαραγωγής των μέσων τιμών αλλά και της κλιματικής μεταβλητότητας αυτών. Αρχικά εξετάζονται οι ροές θερμότητας, ύδατος και πλευστότητας στην διεπιφάνεια θάλασσας-ατμόσφαιρας για το Αιγαίο Πέλαγος και τις παρακείμενες λεκάνες της Ανατολικής Μεσογείου. Κατόπιν γίνεται ανίχνευση και μελέτη των θαλασσίων καυσώνων στην περιοχή, και για πρώτη φορά στην βιβλιογραφία ανάλυση της σύνδεσης ταυτόχρονων ατμοσφαιρικών και θαλασσίων καυσώνων στο Αιγαίο Πέλαγος.

Από τα δεδομένα φαίνεται ότι το Αιγαίο Πέλαγος και η Αδριατική Θάλασσα υφίστανται απώλεια θερμότητας καθ' όλη τη διάρκεια του έτους, συμβάλλοντας σε πιθανές διαδικασίες σχηματισμού πυκνού νερού. Το Αιγαίο Πέλαγος υφίσταται μεγαλύτερη μέση απώλεια θερμότητας από όλες τις άλλες υπολεκάνες, κυρίως λόγω του μεγάλου ποσοστού απώλειας λανθάνουσας και αισθητής θερμότητας, αλλά και μεγάλη μεταβλητότητα αυτών (τυπική απόκλιση). Ο εποχικός κύκλος των συνιστώσων της ροής θερμότητας δείχνει ότι οι απώλειες λόγω εξάτμισης συμβάλλουν περισσότερο στην απώλεια θερμότητας, με υψηλές τιμές κατά τα τέλη του καλοκαιριού και το φθινόπωρο. Οι ροές γλυκού νερού κυριαρχούνται από την εξάτμιση, με μικρότερη χωρική μεταβλητότητα στο νότιο τμήμα της λεκάνης. Η θερμική συνιστώσα της επιφανειακής ροής πλευστότητας καταδεικνύει μεγάλες απώλειες στο Αιγαίο Πέλαγος, οδηγώντας σε ολική απώλεια πλευστότητας το μεγαλύτερο μέρος της περιοχής. Οι εποχικές μέσες τιμές των ροών πλευστότητας παρουσιάζουν ισχυρή αύξηση το καλοκαίρι και ασθενή απώλεια το χειμώνα.

Στον κλιματολογικό ετήσιο μέσο όρο για τα 30 έτη της αλατικής συνιστώσας της ροής πλευστότητας πάνω από το Αιγαίο Πέλαγος, κυριαρχεί η απώλεια λόγω εξάτμισης. Η αλατική συνιστώσα είναι υπεύθυνη για την απώλεια πλευστότητας από την επιφάνεια της θάλασσας σε όλο το Αιγαίο, αλλά μετριάζεται από την παρουσία του επιφανειακού στρώματος τροποποιημένων υδάτων λόγω της εισόδου νερού από τον Εύξεινο Πόντο. Η μεγαλύτερη απώλεια πλευστότητας εμφανίζεται το φθινόπωρο λόγω της υψηλής εξάτμισης και των χαμηλών ατμοσφαιρικών θερμοκρασιών. Η θερμική συνιστώσα είναι περίπου δύο φορές μεγαλύτερη από την αλατική συνιστώσα σε ετήσια βάση, κατά συνέπεια η χωρική κατανομή της μέσης ετήσιας ροής πλευστότητας προσομοιάζει την θερμική της συνιστώσα. Είναι σαφές από την ανάλυση ότι όταν εξετάζεται ολόκληρο το Αιγαίο Πέλαγος, η πλευρική συμβολή των Δαρδανελίων μειώνει οριακά τη συνολική απώλεια πλευστότητας. Ωστόσο αν συμπεριληφθεί μόνο το Βόρειο Αιγαίο αυτή η μείωση σχεδόν διπλασιάζεται, αλλάζοντας δραστικά τον ωκεανογραφικό χαρακτήρα της υπολεκάνης.

Στην συνέχεια έγινε ανάλυση του πεδίου ροής πλευστότητας στις πρώτες έξι κύριες συνιστώσες του (Principal Component Analysis - EOF), οι οποίες αντιπροσωπεύουν περίπου το 98% της συνολικής μεταβλητότητας στο σύστημα Ανατολικής Μεσογείου-Εύξεινου Πόντου. Οι πρώτοι δύο τρόποι εμφανώς σχετίζονται με την εποχική μεταβλητότητα του συστήματος (λόγω της ταλάντωσης σε ετήσιο κύκλο), με τη μεγαλύτερη μεταβλητότητα να παρατηρείται στο κεντρικό και ανατολικό Αιγαίο και κατά μήκος της νότιας ακτής της Ανατολίας. Ο δεύτερος τρόπος χαρακτηρίζεται από την εποχική ροή θερμότητας, με τη μεγαλύτερη μεταβλητότητα να παρατηρείται σε περιοχές όπου συναντώνται δύο διαφορετικές υδάτινες μάζες. Ο τρίτος τρόπος λειτουργίας χαρακτηρίζεται από έναν σχηματισμό διπολικής ταλάντωσης, με τη μεγαλύτερη μεταβλητότητα (πόλους) στο κεντρικό Αιγαίο και τη βόρεια Αδριατική. Ο τέταρτος τρόπος παρουσιάζει και πάλι έναν σχηματισμό διπόλου μεταξύ του βορείου και του νοτίου τμήματος της περιοχής μελέτης, με την μεγαλύτερη μεταβλητότητα στο Αιγαίο και την ανατολική Λεβαντίνη. Ο πέμπτος τρόπος παρουσιάζει σχηματισμούς σε φάση, που συμπίπουν με περιοχές γνωστές για την κυκλωνική τους κυκλοφορία, με την κυρίαρχη συχνότητα να είναι δύο κύκλοι ανά έτος. Ο έκτος τρόπος είναι λιγότερο συνεκτικός, με τη μεγαλύτερη μεταβλητότητα να εντοπίζεται στο Αιγαίο Πέλαγος και στις αφρικανικές ακτές νότια της Κρήτης.

Τα θαλάσσια κύματα καύσωνα στο Αιγαίο Πέλαγος ανιχνεύονται χρησιμοποιώντας τις επιφανειακές θερμοκρασίες του **EMBS** κατά την περίοδο 1985-2015. Η μελέτη επικεντρώνεται στην κατεύθυνση της αλληλεπίδρασης κατά τη διάρκεια των συν-εμφανίζομενων θαλάσσιων-ατμοσφαιρικών γεγονότων και στον αριθμό, τη μέση διάρκεια, τη μέση ένταση και τον δείκτη σφραγίδης επίδρασης στο οικοσύστημα (HWesi), για τα γεγονότα που ανιχνεύονται στο Αιγαίο Πέλαγος. Ο μεγαλύτερος αριθμός συμβάντων εμφανίζεται πάνω από τις βόρειες, βορειοδυτικές και δυτικές παράκτιες

περιοχές του Αιγαίου Πελάγους. Οι νότιες και νοτιοανατολικές περιοχές φιλοξενούν γεγονότα μεγαλύτερης διάρκειας, ενώ η υψηλότερη μέση ένταση εντοπίζεται γύρω από την έξοδο των Δαρδανελίων, τον κόλπο του Σάρου και τμήματα του βόρειου και κεντρικού Αιγαίου. Η συνυπάρχουσα αύξηση της θερμοκρασίας λόγω κλιματικής αλλαγής που εμφανίζεται ως μια κλίση υποβάθρου στη χρονοσειρά, οδηγεί σε μεροληψία ως προς την εμφάνιση περισσοτέρων καυσώνων προς το τέλος της περιόδου μελέτης.

Υπολογίστηκαν οι ημερήσιες ανωμαλίες της μέγιστης ατμοσφαιρικής θερμοκρασίας και οι ημερήσιες ανωμαλίες της επιφανειακής θερμοκρασίας κατά τη διάρκεια των θαλάσσιων καυσώνων στο Αιγαίο Πέλαγος. Η ανάλυση δείχνει ότι παρόλο που η θάλασσα εμφανίζει καύσωνες μεγαλύτερης διάρκειας απ' ότι η ατμόσφαιρα, παρουσιάζει πολύ χαμηλές θερμοκρασιακές ανωμαλίες, πιθανώς και λόγω της μικρότερης μεταβλητότητας της θερμοκρασίας κατά τους χειμερινούς μήνες. Το βάθος του μεικτού στρώματος παρουσιάζει μέγιστο κατά την χειμερινή περίοδο, γεγονός που αυξάνει την θερμική αδράνεια του ωκεανού λόγω της μεγάλης θερμοχωρητικότητας του νερού. Αυτό καταδεικνύει ότι οι υψηλές ατμοσφαιρικές θερμοκρασίες πιθανότατα επιτείνονται από γεγονότα θαλασσίων καυσώνων διαρκείας.

Η παγκόσμια τάση θέρμανσης αφαιρέθηκε τόσο από τα δεδομένα ατμοσφαιρικής θερμοκρασίας του **CCLM** όσο και από τα δεδομένα επιφανειακής θερμοκρασίας του **EMBS**, αποκαλύπτοντας ένα ρυθμό θέρμανσης για το Αιγαίο Πέλαγος 1,7 έως 2,2 φορές μεγαλύτερο από αυτόν του παγκόσμιου μέσου όρου. Εξετάστηκε επίσης η πιθανή ανατροφοδότηση μέσω της ανταλλαγής ενέργειας αέρα-θάλασσας κατά τη διάρκεια γεγονότων καύσωνα, με τις ανωμαλίες της επιφανειακής ροής θερμότητας να είναι θετικές σε ολόκληρο το Αιγαίο Πέλαγος, υποδεικνύοντας μια συνολική εισροή θερμότητας από την ατμόσφαιρα στον ωκεανό κατά τη διάρκεια ταυτόχρονων εμφανίσεων τέτοιων γεγονότων.

Η μελέτη καταδεικνύει ότι οι ατμοσφαιρικοί καύσωνες μπορούν να ενισχύσουν τις ανωμαλίες της επιφανειακής θαλάσσιας θερμοκρασίας και ενδεχομένως να προκαλέσουν ή να βοηθήσουν στη δημιουργία ενός θαλάσσιου καύσωνα. Ωστόσο, δεν λαμβάνονται υπόψη οι εποχικές διαφοροποιήσεις στις συνθήκες καύσωνα και δεν διευκρινίζεται αν η κατευθυντικότητα που απεικονίζεται από την ανωμαλία της ροής θερμότητας αντιπροσωπεύει την ενίσχυση ενός υφιστάμενου καύσωνα ή την δημιουργία ενός μη υπάρχοντος. Για να διαφοροποιηθούν οι ανωμαλίες της επιφανειακής ροής θερμότητας, αυτές διαχωρίζονται ανάλογα με την εποχή και τον τύπο του συμβάντος. Οι διαφορές στις ανωμαλίες της ροής θερμότητας κατά τη διάρκεια των ταυτόχρονων γεγονότων σε σύγκριση με τα ατμοσφαιρικά γεγονότα, είναι ως επί το πλείστον αρνητικές σε όλες τις εποχές. Οι διαφορές στις ανωμαλίες ροής θερμότητας κατά τη διάρκεια ταυτόχρονων γεγονότων σε σύγκριση με θαλάσσια γεγονότα, είναι κυρίως θετικές σε όλες τις εποχές. Τέλος, οι διαφορές στις ανωμαλίες ροής θερμότητας κατά τη διάρκεια ταυτόχρονων συμβάντων σε σχέση με το μέσο

όρο των συμβάντων, δείχνοντας κατά πόσον ο μηχανισμός ενίσχυσης των ταυτόχρονων συμβάντων παρουσιάζει προτίμηση στην κατεύθυνση. Οι καλοκαιρινοί μήνες παρουσιάζουν γενικά τιμές πιο κοντά στο μηδέν, γεγονός που σημαίνει ότι οι ροές θερμότητας κατά τη διάρκεια των ταυτόχρονων γεγονότων του καλοκαιριού δεν διαφοροποιούνται τόσο πολύ σε σχέση με τα μεμονωμένα γεγονότα.

## ΣΥΜΠΕΡΑΣΜΑΤΑ

Η παρούσα διατριβή επικεντρώνεται στη μελέτη των φυσικών ιδιοτήτων των υδάτων της ανατολικής Μεσογείου, συμπεριλαμβανομένης της κυκλοφορίας, της θερμότητας λειτουργίας και των αλληλεπιδράσεων με άλλες λεκάνες. Γίνεται μια προσπάθεια κάλυψης ενός σημαντικού βιβλιογραφικού κενού στην παραγωγή αξιόπιστων κλιματικών προβλέψεων της θαλάσσιας κυκλοφορίας και των φυσικών χαρακτηριστικών του Αιγαίου Πελάγους σε χρονικές κλίμακες δεκαετιών, με μια προσέγγιση τόσο από τεχνικής όσο και από περιγραφικής/αναλυτικής πλευράς.

Η τεχνική προσέγγιση περιλαμβάνει τη δημιουργία μιας διάταξης ωκεάνιας αριθμητικής προσομοίωσης που αναπαράγει ρεαλιστικά τη φυσική ωκεανογραφία της Ανατολικής Μεσογείου και του Εύξεινου Πόντου, περιλαμβάνοντας την φυσική διασύνδεση του συστήματος. Το εργαλείο αυτό παράγει ένα σύνολο δεδομένων ημερησίων μέσων όρων που καλύπτει την περίοδο από την 1η Ιανουαρίου 1985 έως την 31η Δεκεμβρίου 2014. Η διαδικασία επικύρωσης οδήγησε σε θετική αξιολόγηση των επιδόσεων του μοντέλου, επεκτείνοντας τις δυνατότητες για μια πιο ολοκληρωμένη μελέτη της κλιματολογίας της περιοχής.

Η περιγραφική προσέγγιση περιλαμβάνει την ανάλυση του συνόλου δεδομένων που παράγεται από την αριθμητική προσομοίωση για τη μελέτη πραγματικών φυσικών διεργασιών που λαμβάνουν χώρα στο Αιγαίο Πέλαγος. Η μελέτη αποκαλύπτει τον ποικιλόμορφο ρόλο της εκροής των υδάτων του Εύξεινου Πόντου ως ρυθμιστή των απωλειών πλευστότητας της λεκάνης, καθώς και τη σημασία της συμπεριφοράς της λεκάνης ως μια εικ των πλέον σημαντικών πηγών μεταβλητότητας της επιφανειακής ροής πλευστότητας στην Ανατολική Μεσόγειο. Η ανάλυση που έγινε κατά την ανίχνευση κυμάτων καύσωνα, δείχνει ότι υπάρχει μια μετρήσιμη ενίσχυση μεταξύ ατμόσφαιρας και θάλασσας κατά τη διάρκεια ταυτόχρονων γεγονότων, αλλά απαιτείται περαιτέρω έρευνα για να ποσοτικοποιηθεί και να εξηγηθεί εις βάθος ο μηχανισμός αυτός.

Τα κύρια καινοτόμα στοιχεία αυτής της μελέτη μπορούν να συνοψιστούν στα εξής:

- α') Αναπτύχθηκε μια νέα μέθοδος μηχανικής μάθησης για την λεκάνη απορροής του Εύξεινου Πόντου, προκειμένου να εκτιμηθούν οι ποτάμιες απορροές σε παρελθοντικά και μελλοντικά κλίματα, χρησι-

μοποιώντας για είσοδο μόνο βροχόπτωση και τοπογραφικά δεδομένα, με πολύ ικανοποιητικά αποτελέσματα.

- β) Ένα ενιαίο συνεκτικό αριθμητικό πλέγμα μεταβλητής ανάλυσης που συνδέει την Ανατολική Μεσόγειο και τον Εύξεινο Πόντο, αναπτύχθηκε, δοκιμάστηκε και εφαρμόστηκε για πρώτη φορά στην περιοχή με τη χρήση του συστήματος προσομοίωσης **ROMS**. Προκειμένου να επιτευχθεί η απαιτούμενη χωρική ανάλυση για μια ρεαλιστική προσομοίωση της ανταλλαγής στα στενά των Δαρδανελίων και του Βοσπόρου, η ανάλυση του πλέγματος αυξήθηκε στις περιοχές αυτές, και μειώθηκε σε περιοχές χαμηλών υδροδυναμικών απαιτήσεων, για υψηλότερη υπολογιστική απόδοση.
- γ) Για την επικύρωση της τριακονταετούς προσομοίωσης χρησιμοποιήθηκε ένα ιδιαίτερα ευρύ και πλήρες σύνολο παρατηρήσεων του θαλάσσιου περιβάλλοντος, ενώ η αξιολόγηση δεν περιορίστηκε στην επιφάνεια της θάλασσας, αλλά περιλαμβάνει και το εσωτερικό της θαλάσσιας στήλης. Η διαδικασία αξιολόγησης κατέληξε στο συμπέρασμα ότι τα αποτελέσματα και η αναπαράσταση του συστήματος είναι άκρως ικανοποιητικά και ρεαλιστικά, για την 30ετή προσομοίωση (hindcast).
- δ) Επισημάνθηκε η επίδραση της εκροής των Δαρδανελίων στη διαμόρφωση των ανταλλαγών θερμότητας με την ατμόσφαιρα πάνω από το Αιγαίο Πέλαγος, και αποκαλύφθηκε ο ρόλος της εκροής των υδάτων του Εύξεινου Πόντου ως ρυθμιστή των απωλειών πλευστότητας στη λεκάνη.
- ε) Αποκαλύφθηκε για πρώτη φορά η συμπεριφορά του Αιγαίου Πελάγους ως περιοχής με την μεγαλύτερη μεταβλητότητα στις επιφανειακές ροές πλευστότητας σε ολόκληρο το σύστημα ανατολικής Μεσογείου - Ευξείνου Πόντου.
- ζ) Αποκαλύφθηκε μια σχετικά μεγάλη τάση θέρμανσης της θαλάσσιας επιφάνειας και της υπερκείμενης ατμόσφαιρας στο Αιγαίο Πέλαγος κατά την περίοδο των 30 ετών (περίπου διπλάσια από την τάση θέρμανσης του παγκόσμιου μέσου όρου, τόσο στον ωκεανό όσο και στην ατμόσφαιρα).
- η) Εντοπίστηκε και αναλύθηκε για πρώτη φορά στη Μεσόγειο, η συσχέτιση θαλασσίων κυμάτων καιύσωνα με την συν-εμφάνιση ατμοσφαιρικών καυσώνων, καθώς και οι πιθανές αλληλεπιδράσεις μεταξύ των δύο, καταλήγοντας στην διατύπωση μιας υπόθεσης για έναν μηχανισμό αλληλοενίσχυσης μέσω θερμικών ροών. Τα πρώτα αποτελέσματα υποστηρίζουν τον προτεινόμενο μηχανισμό ενίσχυσης, αλλά η ανάλυση δεν έχει ακόμη ολοκληρωθεί.

Η προσομοίωση του Συστήματος ανατολικής Μεσογείου-Εύξεινου Πόντου (EMBS) αποτελεί σημαντική πρόοδο στις κλιματολογικές μελέτες στην ανατολική Μεσόγειο, και ιδίως στο Αιγαίο Πέλαγος. Βελτιώνει την κατανόηση της κλιματικής μεταβλητότητας και των υδροδυναμικών διεργασιών με τη διασύνδεση του Εύξεινου Πόντου και της ανατολικής Μεσογείου. Η προσομοίωση περιγράφει με επιτυχία την πολύπλοκη διαδικασία ανταλλαγής νερού μεταξύ των δύο λεκανών, ένα χαρακτηριστικό που προηγουμένως περιγραφόταν με παραμετροποίησεις στις πολυετείς προσομοιώσεις, και κατά συνέπεια με περιορισμένο ρεαλισμό. Εισάγεται μια πρωτοποριακή μέθοδος κατασκευής πλέγματος για την περιοχή, και μια διαμόρφωση προσομοίωσης η οποία οδηγεί σε ελάχιστη παρέκκλιση των πεδίων σε βάθος χρόνου, παρά την έλλειψη αφομοίωσης παρατηρησιακών δεδομένων. Η προσομοίωση EMBS παρέχει μια πιο αξιόπιστη και λεπτομερή περιγραφή της κλιματολογίας και της φυσικής ωκεανογραφίας της περιοχής (σε σχέση με τις υπάρχουσες προσομοιώσεις αντίστοιχης διαμόρφωσης), αποτυπώνοντας ικανοποιητικά τις μέσες ροές, τη υπερ-ετήσια και εποχική μεταβλητότητα και τις κατανομές υδάτινων μαζών. Μελλοντικές εργασίες περιλαμβάνουν την επέκταση της ανάλυσης των ροών πλευστότητας, την δημιουργία καλύτερων διατυπώσεων για τον ορισμό και τις μεθόδους ανίχνευσης συν-εμφανιζόμενων καυσώνων, και τη διερεύνηση των μηχανισμών αλληλοενίσχυσης μεταξύ θαλάσσιων και ατμοσφαιρικών καυσώνων.

## BIBLIOGRAPHY

---

- Allen, J. S., Newberger, P. A., & Federiuk, J. (1995). Upwelling circulation on the oregon continental shelf. part i: Response to idealized forcing. *Journal of Physical Oceanography*, 25(8), 1843–1866. [https://doi.org/10.1175/1520-0485\(1995](https://doi.org/10.1175/1520-0485(1995))
- Andersen, O., & Scharroo, R. (2011). Range and geophysical corrections in coastal regions: And implications for mean sea surface determination. In S. Vignudelli, A. Kostianoy, P. Cipollini, & J. Benveniste (Eds.), *Coastal altimetry* (pp. 103–146). Springer.
- Androulidakis, Y. S., & Krestenitis, Y. N. (2022). Sea surface temperature variability and marine heat waves over the aegean, ionian, and cretan seas from 2008-2021. *Journal of Marine Science and Engineering*, 10(42). <https://doi.org/10.3390/jmse10010042>
- Androulidakis, Y. S., Krestenitis, Y. N., & Kourafalou, V. H. (2012). Connectivity of north aegean circulation to the black sea water budget. *Continental Shelf Research*, 48, 8–26. <https://doi.org/10.1016/j.csr.2012.08.019>
- Armi, L., & Farmer, D. M. (1986). Maximal two-layer exchange through a contraction with barotropic net flow. *Journal of Fluid Mechanics*, 164, 27–51. <https://doi.org/10.1017/S0022112086002458>
- Astraldi, M., Balopoulos, S., Candela, J., Font, J., Gacic, M., Gasparini, G., Manca, B., Theocharis, A., & Tintoré, J. (1999). The role of straits and channels in understanding the characteristics of mediterranean circulation. *Progress in Oceanography*, 44(1), 65–108. [https://doi.org/10.1016/S0079-6611\(99\)00021-X](https://doi.org/10.1016/S0079-6611(99)00021-X)
- Aydoğdu, A., Pinardi, N., Özsoy, E., Danabasoglu, G., Gürses, Ö., & Karspeck, A. (2018). Circulation of the turkish straits system under interannual atmospheric forcing. *Ocean Science*, 14(5), 999–1019. <https://doi.org/10.5194/os-14-999-2018>
- Baines, P. G. (1995). *Topographic effects in stratified flows*. Cambridge University Press.
- Beckmann, A., & Haidvogel, D. (1993). Numerical simulation of flow around a tall isolated seamount. part i: Problem formulation and model accuracy. *Journal of Physical Oceanography*, 23(8), 1736–1753. [https://doi.org/10.1175/1520-0485\(1993](https://doi.org/10.1175/1520-0485(1993))
- Bellafiore, D., Ferrarin, C., Maicu, F., Manfè, G., Lorenzetti, G., Umgieser, G., Zaggia, L., & Levinson, A. V. (2021). Saltwater intrusion in a mediterranean delta under a changing climate. *Journal of Geophysical Research: Oceans*, 126(2), e2020JC016437. <https://doi.org/10.1029/2020JC016437>

- Beşiktepe, S. T. (2003). Density currents in the two-layer flow: An example of dardanelles outflow (G.-v. Elsevier, Ed.). [https://doi.org/10.1016/S0399-1784\(03\)00015-X](https://doi.org/10.1016/S0399-1784(03)00015-X)
- Beşiktepe, S. T., Sur, H. I., Özsoy, E., Latif, M. A., Oğuz, T., & Ünlüata, Ü. (1994). The circulation and hydrography of the marmara sea. *Progress in Oceanography*, 34(4), 285–334. [https://doi.org/10.1016/0079-6611\(94\)90018-3](https://doi.org/10.1016/0079-6611(94)90018-3)
- Buongiorno Nardelli, B., Tronconi, C., Pisano, A., & Santoleri, R. (2013). High and ultra-high resolution processing of satellite sea surface temperature data over southern european seas in the framework of myocean project. *Remote Sensing of Environment*, 129, 1–16. <https://doi.org/10.1016/j.rse.2012.10.012>
- Buongiorno Nardelli, B., Colella, S., Santoleri, R., Guaracino, M., & Kholod, A. (2010). A re-analysis of black sea surface temperature. *Journal of Marine Systems*, 79(1), 50–64. <https://doi.org/10.1016/j.jmarsys.2009.07.001>
- Cavole, L. M., Demko, A. M., Diner, R. E., Giddings, A., Koester, I., Pagniello, C. M., Paulsen, M.-L., Ramirez-Valdez, A., Schwenck, S. M., Yen, N. K., Zill, M. E., & Franks, P. J. (2016). Biological impacts of the 2013–2015 warm-water anomaly in the northeast pacific: Winners, losers, and the future. *Oceanography*. <https://doi.org/10.5670/oceanog.2016.32>
- Chang, Y.-S., Zhang, S., Rosati, A., Delworth, T. L., & Stern, W. F. (2013). An assessment of oceanic variability for 1960–2010 from the gfdl ensemble coupled data assimilation. *Climate Dynamics*, 40(3), 775–803. <https://doi.org/10.1007/s00382-012-1412-2>
- Chapman, D. (1985). Numerical treatment of cross-shelf open boundaries in a barotropic coastal ocean model. *Journal of Physical Oceanography*, 15, 1060–1075.
- Ciliberti, S. A., Jansen, E., Coppini, G., Peneva, E., Azevedo, D., Causio, S., Stefanizzi, L., Creti', S., Lecci, R., Lima, L., Ilicak, M., Pinardi, N., & Palazov, A. (2022). The black sea physics analysis and forecasting system within the framework of the copernicus marine service. *Journal of Marine Science and Engineering*, 10(48). <https://doi.org/10.3390/jmse10010048>
- CMEMS. (n.d.). Copernicus marine service eu. altimeter satellite gridded sea level anomalies (sla) computed with respect to a twenty-year 2012 mean. product sealevel\_eur\_phy\_l4\_my\_008\_068 [Accessed: 2021-11-21]. <https://doi.org/10.48670/moi-00141>
- Collins, M., Sutherland, M., Bouwer, L., Cheong, S., Frölicher, T., Combes, H. J. D., Roxy, M. K., Losada, I., McInnes, K., Ratter, B., Rivera-Arriaga, E., Susanto, R., Swingedouw, D., & Tibig, L. (2019). *Extremes, abrupt changes and managing risk*. In: IPCC Special Report on the Ocean; Cryosphere in a Changing Climate. H.-O. Pörtner, D.C. Roberts, V. Masson-Delmotte, P.

- Zhai, M., Tignor, E., Poloczanska, K., Mintenbeck, A., Alegria, M., Nicolai, A., Okem, J., Petzold, B., Rama, N.M., Weyer (eds.). Cambridge University Press, Cambridge, UK; New York, NY, USA. <https://doi.org/10.1017/9781009157964.008>
- Darmaraki, S., Somot, S., Sevault, F., Nabat, P., Cabos Narvaez, W. D., Cavicchia, L., Djurdjevic, L., Vladimirand Li, Sannino, G., & Sein, D. V. (2019). Future evolution of marine heatwaves in the mediterranean sea. *Climate Dynamics*, 53(3), 1371–1392. <https://doi.org/10.1007/s00382-019-04661-z>
- Dee, D. P., Uppala, S. M., Simmons, A. J., Berrisford, P., Poli, P., Kobayashi, S., Andrae, U., Balmaseda, M. A., Balsamo, G., Bauer, P., Bechtold, P., Beljaars, A. C. M., van de Berg, L., Bidlot, J., Bormann, N., Delsol, C., Dragani, R., Fuentes, M., Geer, A. J., ... Vitart, F. (2011). The era-interim reanalysis: Configuration and performance of the data assimilation system. *Quarterly Journal of the Royal Meteorological Society*, 137(656), 553–597. <https://doi.org/10.1002/qj.828>
- Dietrich, D. E., Tseng, Y.-H., Medina, R., Piacsek, S. A., Liste, M., Olabarrieta, M., Bowman, M. J., & Mehra, A. (2008). Mediterranean overflow water (mow) simulation using a coupled multiple-grid mediterranean sea/north atlantic ocean model. *Journal of Geophysical Research: Oceans*, 113(C7). <https://doi.org/10.1029/2006JC003914>
- Fairall, C. W., Bradley, E. F., Rogers, D. P., Edson, J. B., & Young, G. S. (1996). Bulk parameterization of air-sea fluxes for tropical ocean-global atmosphere coupled-ocean atmosphere response experiment. *Journal of Geophysical Research: Oceans*, 101(C2), 3747–3764. <https://doi.org/10.1029/95JC03205>
- Ferrarin, C., Bellafiore, D., Sannino, G., Bajo, M., & Umgiesser, G. (2018). Tidal dynamics in the inter-connected mediterranean, marmara, black and azov seas. *Progress in Oceanography*, 161, 102–115. <https://doi.org/10.1016/j.pocean.2018.02.006>
- Feudale, L., & Shukla, J. (2011). Influence of sea surface temperature on the european heat wave of 2003 summer. part i: An observational study. *Climate Dynamics*, 36(9), 1691–1703. <https://doi.org/10.1007/s00382-010-0788-0>
- Flather, R. (1976). A tidal model of the northwest european continental shelf. *Mem. Soc. R. Sci. Liege*, 6(10), 141–164.
- Founda, D., & Giannakopoulos, C. (2009). The exceptionally hot summer of 2007 in athens, greece – a typical summer in the future climate? *Global and Planetary Change*, 67(3), 227–236. <https://doi.org/10.1016/j.gloplacha.2009.03.013>
- Frölicher, T. L., & Laufkötter, C. (2018). Emerging risks from marine heat waves. *Nature Communications*, 9(1), 650. <https://doi.org/10.1038/s41467-018-03163-6>

- Galperin, B., Kantha, L. H., Hassid, S., & Rosati, A. (1988). A quasi-equilibrium turbulent energy model for geophysical flows. *Journal of Atmospheric Sciences*, 45(1), 55–62. [https://doi.org/10.1175/1520-0469\(1988\)45<55:AQETMF>2.0.CO;2](https://doi.org/10.1175/1520-0469(1988)45<55:AQETMF>2.0.CO;2)
- García-Herrera, R., Díaz, J., Trigo, R. M., Luterbacher, J., & Fischer, E. M. (2010). A review of the european summer heat wave of 2003. *Critical Reviews in Environmental Science and Technology*, 40(4), 267–306. <https://doi.org/10.1080/10643380802238137>
- Garrabou, J., Coma, R., Bensoussan, N., Bally, M., Chevaldonné, P., Cigliano, M., Diaz, D., Harmelin, J. G., Gambi, M. C., Kersting, D. K., Ledoux, J. B., Lejeusne, C., Linares, C., Marschal, C., Pérez, T., Ribes, M., Romano, J. C., Serrano, E., Teixido, N., ... Cerrano, C. (2009). Mass mortality in northwestern mediterranean rocky benthic communities: Effects of the 2003 heat wave. *Global Change Biology*, 15(5), 1090–1103. <https://doi.org/10.1111/j.1365-2486.2008.01823.x>
- Gertman, I., Pinardi, N., Popov, Y., & Hecht, A. (2006). Aegean sea water masses during the early stages of the eastern mediterranean climatic transient (1988–90). *Journal of Physical Oceanography*, 36(9), 1841–1859. <https://doi.org/10.1175/JPO2940.1>
- Haney, R. L. (1991). On the pressure gradient force over steep topography in sigma coordinate ocean models. *Journal of Physical Oceanography*, 21(4), 610–619. [https://doi.org/10.1175/1520-0485\(1991\)021<0610:OTPGRF>2.0.CO;2](https://doi.org/10.1175/1520-0485(1991)021<0610:OTPGRF>2.0.CO;2)
- Hartmann, E., Schulz, J.-P., Seibert, R., Schmidt, M., Zhang, M., Luterbacher, J., & Tölle, M. H. (2020). Impact of environmental conditions on grass phenology in the regional climate model cosmo-clm. *Atmosphere*, 11(12). <https://doi.org/10.3390/atmos11121364>
- Hartmann, E., Zhang, M., Adakudlu, M., Wagner, S., & Xoplaki, E. (In preparation). Implementing external climate forcings into the cosmo-clm - a samalas sensitivity study.
- Hoag, H. (2014). Russian summer tops 'universal' heatwave index. *Nature*. <https://doi.org/10.1038/nature.2014.16250>
- Hobday, A. J., Alexander, L. V., Perkins, S. E., Smale, D. A., Straub, S. C., Oliver, E. C., Benthuysen, J. A., Burrows, M. T., Donat, M. G., Feng, M., Holbrook, N. J., Moore, P. J., Scannell, H. A., Sen Gupta, A., & Wernberg, T. (2016). A hierarchical approach to defining marine heatwaves. *Progress in Oceanography*, 141, 227–238. <https://doi.org/10.1016/j.pocean.2015.12.014>
- Hobday, A. J., Oliver, E. C., Gupta, A. S., Benthuysen, J. A., Burrows, M. T., Donat, M. G., Holbrook, N. J., Moore, P. J., Thomsen, M. S., Wernberg, T., & Smale, D. A. (2018). Categorizing and naming marine heatwaves. *Oceanography*. <https://doi.org/10.5670/oceanog.2018.205>

- Hogg, A. M., Ivey, G. N., & Winters, K. B. (2001). Hydraulics and mixing in controlled exchange flows. *Journal of Geophysical Research: Oceans*, 106(C1), 959–972. <https://doi.org/10.1029/2000JC000266>
- Holbrook, N. J., Scannell, H. A., Sen Gupta, A., Benthuysen, J. A., Feng, M., Oliver, E. C. J., Alexander, L. V., Burrows, M. T., Donat, M. G., Hobday, A. J., Moore, P. J., Perkins-Kirkpatrick, S. E., Smale, D. A., Straub, S. C., & Wernberg, T. (2019). A global assessment of marine heatwaves and their drivers. *Nature Communications*, 10(1), 2624. <https://doi.org/10.1038/s41467-019-10206-z>
- Ilicak, M., Federico, I., Barletta, I., Mutlu, S., Karan, H., Ciliberti, S. A., Clementi, E., Coppini, G., & Pinardi, N. (2021). Modeling of the turkish strait system using a high resolution unstructured grid ocean circulation model. *Journal of Marine Science and Engineering*, 9(7). <https://doi.org/10.3390/jmse9070769>
- IPCC. (2007). *Climate change 2007: Impacts, adaptation and vulnerability*. Contribution of Working Group II to the Fourth Assessment Report of the Intergovernmental Panel on Climate Change, M.L. Parry, O.F. Canziani, J.P. Palutikof, P.J. van der Linden; C.E.Hanson (eds.). Cambridge University Press, Cambridge, United Kingdom; New York, NY, USA.
- Jarosz, E., Teague, W. J., Book, J. W., & Beşiktepe, S. T. (2013). Observed volume fluxes and mixing in the dardanelles strait. *Journal of Geophysical Research: Oceans*, 118(10), 5007–5021. <https://doi.org/10.1002/jgrc.20396>
- Kanarska, Y., & Maderich, V. (2008). Modelling of seasonal exchange flows through the dardanelles strait. *Estuarine, Coastal and Shelf Science*, 79(3), 449–458. <https://doi.org/10.1016/j.ecss.2008.04.019>
- Kantha, L., & Clayson, C. (1994). Numerical models of oceans and oceanic processes. in: International geophysics series. 66, 940.
- Kassis, D., & Korres, G. (2021). Recent hydrological status of the aegean sea derived from free drifting profilers. *Mediterranean Marine Science*, 22(2), 347–361. <https://doi.org/10.12681/mms.24833>
- Kataoka, T., Tozuka, T., & Yamagata, T. (2017). Generation and decay mechanisms of ningaloo niño/niña. *Journal of Geophysical Research: Oceans*, 122(11), 8913–8932. <https://doi.org/10.1002/2017JC012966>
- Kourafalou, V., & Barbopoulos, K. (2003). High resolution simulations on the north aegean sea seasonal circulation. *Annales Geophysicae*, 21(1), 251–265. <https://doi.org/10.5194/angeo-21-251-2003>
- Kourafalou, V., & Tsiaras, K. (2007). A nested circulation model for the north aegean sea. *Ocean Science*, 3(1), 1–16. <https://doi.org/10.5194/os-3-1-2007>

- Kuglitsch, F. G., Toreti, A., Xoplaki, E., Della-Marta, P. M., Zerefos, C. S., Türkeş, M., & Luterbacher, J. (2010). Heat wave changes in the eastern mediterranean since 1960. *Geophysical Research Letters*, 37(4). <https://doi.org/https://doi.org/10.1029/2009GL041841>
- Lhotka, O., & Kysely, J. (2015). Characterizing joint effects of spatial extent, temperature magnitude and duration of heat waves and cold spells over central europe. *International Journal of Climatology*, 35(7), 1232–1244. <https://doi.org/https://doi.org/10.1002/joc.4050>
- Lima, L., Masina, S., Ciliberti, S. A., Peneva, E. L., Cretí, S., Stefanizzi, L., Lecci, R., Palermo, F., Coppini, G., Pinardi, N., & Palazov, A. (2020). Black sea physical reanalysis (cmems bs-currents). [https://doi.org/10.25423/CMCC/BLKSEA\\_REANALYSIS\\_PHYS\\_007\\_004](https://doi.org/10.25423/CMCC/BLKSEA_REANALYSIS_PHYS_007_004)
- Lindström, G., Pers, C., Rosberg, J., Strömqvist, J., & Arheimer, B. (2010). Development and testing of the hype (hydrological predictions for the environment) water quality model for different spatial scales. *Hydrology Research*, 41(3-4), 295–319. <https://doi.org/10.2166/nh.2010.007>
- Maderich, V., Ilyin, Y., & Lemeshko, E. (2015). Seasonal and interannual variability of the water exchange in the Turkish Straits System estimated by modelling. *Mediterranean Marine Science*, 16(2), 444–459. <https://doi.org/10.12681/mms.1103>
- Maderich, V., Konstantinov, S., Kulik, A., & Oleksiuk, V. (1998). Laboratory modelling of the water exchange through the sea straits. *OKEANOLOGIYA*, 38(5), 665–672.
- Maillard, C., & Balopoulos, E. (2002). ; the medar group. recent advances in oceanographic data management of the mediterranean and black seas: The medar/medatlas 2002 data base. the colour of ocean data. <http://www.ifremer.fr/medar>
- Malanotte-Rizzoli, P., Manca, B. B., D'Alcala, M. R., Theocharis, A., Brenner, S., Budillon, G., & Ozsoy, E. (1999). The Eastern Mediterranean in the 80s and in the 90s: The big transition in the intermediate and deep circulations. *Dynamics of Atmospheres and Oceans*, 29(2-4), 365–395. [https://doi.org/10.1016/S0377-0265\(99\)00011-1](https://doi.org/10.1016/S0377-0265(99)00011-1)
- Mamoutos, I. G., Potiris, E., Tragou, E., Zervakis, V., & Petalas, S. (2021). A high-resolution numerical model of the North Aegean Sea aimed at climatological studies. *Journal of Marine Science and Engineering*, 9(12). <https://doi.org/10.3390/jmse9121463>
- Mamoutos, I. G., Zervakis, V., Tragou, E., Karydis, M., Frangoulis, C., Kolovoyiannis, V., Georgopoulos, D., & Psarra, S. (2017). The role of wind-forced coastal upwelling on the thermohaline

- functioning of the north aegean sea. *Continental Shelf Research*, 149, 52–68. <https://doi.org/10.1016/j.csr.2017.05.009>
- Marchesiello, P., McWilliams, J. C., & Shchepetkin, A. (2001). Open boundary conditions for long-term integration of regional oceanic models. *Ocean Modelling*, 3(1), 1–20. [https://doi.org/10.1016/S1463-5003\(00\)00013-5](https://doi.org/10.1016/S1463-5003(00)00013-5)
- Martinho, A. S., & Battieen, M. L. (2006). On reducing the slope parameter in terrain-following numerical ocean models. *Ocean Modelling*, 13(2), 166–175. <https://doi.org/10.1016/j.ocemod.2006.01.003>
- Mason, E., Molemaker, J., Shchepetkin, A. F., Colas, F., McWilliams, J. C., & Sangrà, P. (2010). Procedures for offline grid nesting in regional ocean models. *Ocean Modelling*, 35(1), 1–15. <https://doi.org/10.1016/j.ocemod.2010.05.007>
- Mavropoulou, A.-M., Vervatis, V., & Sofianos, S. (2022). The mediterranean sea overturning circulation: A hindcast simulation (1958 – 2015) with an eddy-resolving (1/36) model. *Deep Sea Research Part I: Oceanographic Research Papers*, 187, 103846. <https://doi.org/10.1016/j.dsr.2022.103846>
- Mecking, J. V., Drijfhout, S. S., Hirschi, J. J.-M., & Blaker, A. T. (2019). Ocean and atmosphere influence on the 2015 european heatwave. *Environmental Research Letters*, 14(11), 114035. <https://doi.org/10.1088/1748-9326/ab4d33>
- Meehl, G. A., & Tebaldi, C. (2004). More intense, more frequent, and longer lasting heat waves in the 21st century. *Science*, 305(5686), 994–997. <https://doi.org/10.1126/science.1098704>
- Mellor, G. L., & Yamada, T. (1982). Development of a turbulence closure model for geophysical fluid problems. *Reviews of Geophysics*, 20(4), 851–875. <https://doi.org/10.1029/RG020i004p00851>
- Mircheva, B., Tsekov, M., Meyer, U., & Guerova, G. (2017). Anomalies of hydrological cycle components during the 2007 heat wave in bulgaria. *Journal of Atmospheric and Solar-Terrestrial Physics*, 165–166, 1–9. <https://doi.org/10.1016/j.jastp.2017.10.005>
- Napolitano, E., Iacono, R., Palma, M., Sannino, G., Carillo, A., Lombardi, E., Pisacane, G., & Struglia, M. V. (2022). MITO: A new operational model for the forecasting of the mediterranean sea circulation. *Frontiers in Energy Research*, 10. <https://doi.org/10.3389/fenrg.2022.941606>
- Pathmeswaran, C., Sen Gupta, A., Perkins-Kirkpatrick, S. E., & Hart, M. A. (2022). Exploring potential links between co-occurring coastal terrestrial and marine heatwaves in australia. *Frontiers in Climate*, 4. <https://doi.org/10.3389/fclim.2022.792730>
- Paulson, C. A., & Simpson, J. J. (1977). Irradiance measurements in the upper ocean. *Journal of Physical Oceanography*, 7(6), 952–956. [https://doi.org/10.1175/1520-0485\(1977\)007<952>2.0.CO;2](https://doi.org/10.1175/1520-0485(1977)007<952>2.0.CO;2)

- Perkins, S. E., & Alexander, L. V. (2013). On the measurement of heat waves. *Journal of Climate*, 26(13), 4500–4517. <https://doi.org/10.1175/JCLI-D-12-00383.1>
- Perkins-Kirkpatrick, S. E., & Lewis, S. C. (2020). Increasing trends in regional heatwaves. *Nature Communications*, 11(1), 3357. <https://doi.org/10.1038/s41467-020-16970-7>
- Pinardi, N., Özsoy, E., Latif, M. A., Moroni, F., Grandi, A., Manzella, G., Strobel, F. D., & Lyubartsev, V. (2018). Measuring the sea: Marsili's oceanographic cruise (1679–80) and the roots of oceanography. *Journal of Physical Oceanography*, 48(4), 845–860. <https://doi.org/10.1175/JPO-D-17-0168.1>
- Pinardi, N., Zavatarelli, M., Adani, M., Coppini, G., Fratianni, C., Oddo, P., Simoncelli, S., Tonani, M., Lyubartsev, V., Dobricic, S., & Bonaduce, A. (2015). Mediterranean sea large-scale low-frequency ocean variability and water mass formation rates from 1987 to 2007: A retrospective analysis. *Progress in Oceanography*, 132(0), 318–332. <https://doi.org/10.1016/j.pocean.2013.11.003>
- Pisano, A., Buongiorno Nardelli, B., Tronconi, C., & Santoleri, R. (2016). The new mediterranean optimally interpolated pathfinder avhrr sst dataset (1982–2012). *Remote Sensing of Environment*, 176, 107–116. <https://doi.org/10.1016/j.rse.2016.01.019>
- Ponte, R. M., & Ray, R. D. (2002). Atmospheric pressure corrections in geodesy and oceanography: A strategy for handling air tides. *Geophysical Research Letters*, 29(24), 6-1–6–4. <https://doi.org/10.1029/2002GL016340>
- Pratt, L. J. (2008). Critical conditions and composite froude numbers for layered flow with transverse variations in velocity. *Journal of Fluid Mechanics*, 605, 281–291. <https://doi.org/10.1017/S002211200800150X>
- Robine, J.-M., Cheung, S. L. K., Le Roy, S., Van Oyen, H., Griffiths, C., Michel, J.-P., & Herrmann, F. R. (2008). Death toll exceeded 70,000 in europe during the summer of 2003. *Comptes Rendus Biologies*, 331(2), 171–178. <https://doi.org/10.1016/j.crvi.2007.12.001>
- Robinson, P. J. (2001). On the definition of a heat wave. *Journal of Applied Meteorology*, 40(4), 762–775. [https://doi.org/10.1175/1520-0450\(2001\)040<0762:OTDOAH>2.0.CO;2](https://doi.org/10.1175/1520-0450(2001)040<0762:OTDOAH>2.0.CO;2)
- Rockel, B., & Geyer, B. (2008). The performance of the regional climate model clm in different climate regions, based on the example of precipitation. *Meteorologische Zeitschrift*, 17(4), 487–498. <https://doi.org/10.1127/0941-2948/2008/0297>
- Roether, W., Klein, B., Manca, B. B., Theocharis, A., & Kioroglou, S. (2007). Transient Eastern Mediterranean deep waters in response to the massive dense-water output of the Aegean Sea

- in the 1990s. *Progress in Oceanography*, 74(4), 540–571. <https://doi.org/10.1016/j.pocean.2007.03.001>
- Russo, S., Sillmann, J., & Fischer, E. M. (2015). Top ten european heatwaves since 1950 and their occurrence in the coming decades. *Environmental Research Letters*, 10(12), 124003. <https://doi.org/10.1088/1748-9326/10/12/124003>
- Salinger, M. J., Renwick, J., Behrens, E., Mullan, A. B., Diamond, H. J., Sirguey, P., Smith, R. O., Trought, M. C. T., Alexander, L., Cullen, N. J., Fitzharris, B. B., Hepburn, C. D., Parker, A. K., & Sutton, P. J. (2019). The unprecedented coupled ocean-atmosphere summer heatwave in the new zealand region 2017/18: Drivers, mechanisms and impacts. *Environmental Research Letters*, 14(4), 044023. <https://doi.org/10.1088/1748-9326/ab012a>
- Sannino, G., Carillo, A., & Artale, V. (2007). Three - layer view of transports and hydraulics in the strait of gibraltar: A three - dimensional model study. *Journal of Geophysical Research: Oceans*, 112(C3). <https://doi.org/10.1029/2006JC003717>
- Sannino, G., Herrmann, M., Carillo, A., Rupolo, V., Ruggiero, V., Artale, V., & Heimbach, P. (2009). An eddy-permitting model of the Mediterranean Sea with a two-way grid refinement at the Strait of Gibraltar. *Ocean Modelling*, 30(1), 56–72. <https://doi.org/10.1016/j.ocemod.2009.06.002>
- Sannino, G., Carillo, A., Iacono, R., Napolitano, E., Palma, M., Pisacane, G., & Struglia, M. (2022). Modelling present and future climate in the mediterranean sea: A focus on sea-level change. *Climate Dynamics*. <https://doi.org/10.1007/s00382-021-06132-w>
- Sannino, G., Sözer, A., & Özsoy, E. (2017). A high-resolution modelling study of the turkish straits system. *Ocean Dynamics*, 67(3), 397–432. <https://doi.org/10.1007/s10236-017-1039-2>
- Sein, D. V., Mikolajewicz, U., Gröger, M., Fast, I., Cabos, W., Pinto, J. G., Hagemann, S., Semmler, T., Izquierdo, A., & Jacob, D. (2015). Regionally coupled atmosphere-ocean-sea ice-marine biogeochemistry model rom: 1. description and validation. *Journal of Advances in Modeling Earth Systems*, 7(1), 268–304. <https://doi.org/10.1002/2014MS000357>
- Sevault, F., Somot, S., Alias, A., Dubois, C., Lebeaupin-Brossier, C., Nabat, P., Adloff, F., Déqué, M., & Decharme, B. (2014). A fully coupled mediterranean regional climate system model: Design and evaluation of the ocean component for the 1980–2012 period. *Tellus A: Dynamic Meteorology and Oceanography*, 66.
- Shchepetkin, A. F., & McWilliams, J. C. (2003). A method for computing horizontal pressure-gradient force in an oceanic model with a nonaligned vertical coordinate. *Journal of Geophysical Research: Oceans*, 108(C3). <https://doi.org/10.1029/2001JC001047>

- Shchepetkin, A. F., & McWilliams, J. C. (2005). The regional oceanic modeling system (roms): A split-explicit, free-surface, topography-following-coordinate oceanic model. *Ocean Modelling*, 9(4), 347–404. <https://doi.org/10.1016/j.ocemod.2004.08.002>
- Simoncelli, S., Fratianni, C., Pinardi, N., Grandi, A., Drudi, M., Oddo, P., & Dobricic, S. (2019). Mediterranean sea physical reanalysis (cmems med-physics). [https://doi.org/10.25423/MEDSEA\\_REANALYSIS\\_PHYS\\_006\\_004](https://doi.org/10.25423/MEDSEA_REANALYSIS_PHYS_006_004)
- Simoncelli, S., Schaap, D., & Schlitzer, R. (2015). Seadatanet - mediterranean sea - temperature and salinity observation collection v2. <https://doi.org/10.12770/8c3bd19b-9687-429c-a232-48b10478581c>
- Smolarkiewicz, P. K., & Margolin, L. G. (1998). Mpdata: A finite-difference solver for geophysical flows. *Journal of Computational Physics*, 140(2), 459–480. <https://doi.org/10.1006/jcph.1998.5901>
- Somot, S., Sevault, F., Déqué, M., & Crépon, M. (2008). 21st century climate change scenario for the mediterranean using a coupled atmosphere-ocean regional climate model [Mediterranean climate: trends, variability and change]. *Global and Planetary Change*, 63(2), 112–126. <https://doi.org/10.1016/j.gloplacha.2007.10.003>
- Soto-Navarro, J., Jordá, G., Amores, A., Cabos, W., Somot, S., Sevault, F., Macías, D., Djurdjevic, V., Sannino, G., Li, L., & Sein, D. (2020). Evolution of Mediterranean Sea water properties under climate change scenarios in the Med-CORDEX ensemble. *Climate Dynamics*, 54(3), 2135–2165. <https://doi.org/10.1007/s00382-019-05105-4>
- Sözer, A., & Özsoy, E. (2017). Modeling of the bosphorus exchange flow dynamics. *Ocean Dynamics*, 67(3), 321–343. <https://doi.org/10.1007/s10236-016-1026-z>
- Sverdrup, H., Johnson, M. W., & Fleming, R. H. (1942). *The oceans their physics, chemistry, and general biology* [<https://publishing.cdlib.org/ucpressebooks/view?docId=kt167nb66r>]. Prentice-Hall.
- Tragou, E., Petalas, S., & Mamoutos, I. (2022). Air-sea interaction: Heat and fresh-water fluxes in the aegean sea. Springer Berlin Heidelberg. [https://doi.org/10.1007/698\\_2021\\_841](https://doi.org/10.1007/698_2021_841)
- Urban, A., Hanzlikova, H., Kysely, J., & Plavcova, E. (2017). Impacts of the 2015 heat waves on mortality in the czech republic—a comparison with previous heat waves. *International Journal of Environmental Research and Public Health*, 14(12). <https://doi.org/10.3390/ijerph14121562>
- Venice system, symposium on the classification of brackish waters, venice, april 8-14. (1958). 11, 1–248.

- Vervatis, V., Skliris, N., & Sofianos, S. S. (2014). Inter-annual/decadal variability of the north aegean sea hydrodynamics over 1960–2000. *Mediterranean Marine Science*, 15(4), 696–705. <https://doi.org/10.12681/mms.852>
- Vervatis, V., Sofianos, S., Skliris, N., Somot, S., Lascaratos, A., & Rixen, M. (2013). Mechanisms controlling the thermohaline circulation pattern variability in the aegean–levantine region. a hindcast simulation (1960–2000) with an eddy resolving model. *Deep Sea Research Part I: Oceanographic Research Papers*, 74, 82–97. <https://doi.org/10.1016/j.dsr.2012.12.011>
- Weatherall, P., Marks, K. M., Jakobsson, M., Schmitt, T., Tani, S., Arndt, J. E., Rovere, M., Chayes, D., Ferrini, V., & Wigley, R. (2015). A new digital bathymetric model of the world's oceans. *Earth and Space Science*, 2(8), 331–345. <https://doi.org/10.1002/2015EA000107>
- Weedon, G. P., Balsamo, G., Bellouin, N., Gomes, S., Best, M. J., & Viterbo, P. (2014). The wfdei meteorological forcing data set: Watch forcing data methodology applied to era-interim reanalysis data. *Water Resources Research*, 50(9), 7505–7514. <https://doi.org/10.1002/2014WR015638>
- Zervakis, V., Georgopoulos, D., & Drakopoulos, P. G. (2000). The role of the North Aegean in triggering the recent Eastern Mediterranean climatic changes. *Journal of Geophysical Research: Oceans*, 105(C11), 26103–26116. <https://doi.org/10.1029/2000JC900131>
- Zhang, M., Hartmann, E., Adakudlu, M., Wagner, S., & Xoplaki, E. (In preparation). The climate of the eastern mediterranean and the nile basin 2500 years before present: A fully forced cosmo-clm experiment.
- Zhang, M., Tölle, M. H., Hartmann, E., Xoplaki, E., & Luterbacher, J. (2021). A sensitivity assessment of cosmo-clm to different land cover schemes in convection-permitting climate simulations over europe. *Atmosphere*, 12(12). <https://doi.org/10.3390/atmos12121595>



credit: Maria Papadopoulou

An artist's impression of the talk during the doctoral defense in Mytilene. The drawing was a sweet surprise by my friend *Maria* as a gift after the process.

## COLOPHON

The numerical simulations were configured and performed using the Regional Ocean Modeling System (**ROMS**) code (revision 848) developed in Fortran 95 and supported by researchers at the Rutgers University, University of California Los Angeles and contributors worldwide:

<https://www.myroms.org/>

Pre-processing of model input data was performed using personally developed code in Python, bash, Matlab, the NetCDF Operators (NCO), Climate Data Operators (CDO), as well as John Wilkin's Matlab toolkit:

[https://github.com/johnwilkin/roms\\_wilkin/](https://github.com/johnwilkin/roms_wilkin/)

The computational integration was executed through time granted from the Greek Research and Technology Network (**GRNET**) in the National HPC facility—ARIS—, under project ID *petalas-EMBS2*:

<https://hpc.grnet.gr/en/>

The system employed for the computational integration was an *IBM NeXtScale nx360 M4* and the simulation was run using 20 thin compute nodes (out of the available 426 of the system), with 2 *Ivy Bridge - Intel Xeon E5-2680v2* processors of 10 cores for each node, leading to a total of 400 cores for this simulation (with no hyperthreading). The average wall-time with this scaling was about 1 hour for 11 simulation-days, or 41 days for the 30 simulation-years (if executed uninterrupted). Because of the inevitable occasional interruptions, either due to queuing or other reasons, the total real time added up to a total of 141 days for the 30-year simulation period.

Post-processing of output data, formal analysis and plotting of figures, was carried out and coded in , bash, the NetCDF Operators (NCO), Climate Data Operators (CDO), and Python using numpy, scipy, math, Basemap, matplotlib and netCDF4 among other packages, and constitutes of more than 20,000 lines of original code written throughout the course of this research.

As a basis for the typographical look – and – feel of this thesis, the `classicthesis` style package was used, developed by André Miede and Ivo Pletikosić. The style was inspired by Robert Bringhurst's seminal book on typography "*The Elements of Typographic Style*", and is available for both L<sup>A</sup>T<sub>E</sub>X and L<sub>Y</sub>X:

<https://bitbucket.org/amiede/classicthesis/>

The dissertation was defended in public, in front of the Examination Committee, on February the 8<sup>th</sup> 2023, at the University of the Aegean, Mytilene, Greece, and was unanimously approved with honors (cum laude). [certificate protocol nr.: 124/28-02-2023].

*Final Version as of April 2, 2024 (CT v4.6).*



**Summary** Inter-basin water exchanges can be quite important in climatic-scale numerical studies simulating the circulation and hydrographic characteristics of neighboring oceanic basins connected through narrow straits. The crucial role of the interaction between the Mediterranean and the Black Seas is often overseen in simulations of the Aegean Sea, which rely mostly on parameterizations to describe the exchange, essentially decoupling the two basins. In this study, the fully interconnected Eastern Mediterranean-Black Sea system is simulated for the historical period (1985-2015), with an emphasis on the Aegean Sea, using realistic boundary conditions (lateral, atmospheric and hydrological), and a hydrodynamic fully three-dimensional ocean modeling system. The setup of such a configuration is thoroughly described and the performance of the 30-year hindcast product is validated exhaustively against observations and model results, by evaluating the representation of surface fields, circulation, three-dimensional hydrographic characteristics, volumetric water exchanges, and the spatio-temporal variability of the above. The comparison shows a substantial improvement compared to modeling studies that do not include the interaction, and a reliable reproduction of the system's variability in temporal scales ranging from days to inter-annual and decadal-long, and a fairly accurate reproduction of the mean linear trends of change of the basin's characteristics, for this 30-year period. Moreover, due to the free-run configuration of the simulation (i.e., absence of data assimilation schemes) no additional input is required other than the respective boundary conditions, making it possible to reliably extend the same setup for scenarios where observational data are not available, such as in future projections. Simulation results are further examined with respect to physical processes. Analysis of water, heat and buoyancy fluxes over the Aegean Sea, demonstrates the large influence of the Dardanelles inflow to the basin's thermohaline functioning, and the particular behaviour of the basin as the region of highest buoyancy flux variability in the Eastern Mediterranean. Finally, the appearance of marine and atmospheric heatwaves over the region is examined in an effort to deduce a possible reinforcing mechanism between the two domains during co-occurring events, with the first results supporting such a mechanism.



## About the Author

Stamatis Petalas was born in Alexandroupolis, Greece. He holds a BSc degree in Physics from Aristotle University of Thessaloniki, and a MSc degree in Meteorology, Physical Oceanography & Climate from Utrecht University. He conducted his PhD research at the University of the Aegean, studying the physical oceanography of the eastern Mediterranean with a special focus on Greek Seas and their interaction with the Black Sea, as well as the ocean influence on local climate through air-sea interactions.

During the course of his PhD, he participated in 4 publications in scientific journals, 1 publication in a book chapter, 13 publications in conferences and worked on 7 EU-funded projects. Additionally, he provided teaching assistance on several undergraduate and graduate courses at the Department of Marine Sciences.

His research interests fall within the intersection between Geophysical Fluid Dynamics, Climate Dynamics and Numerical Modelling, and include Ocean Circulation, Air-Sea Interactions, Ocean Waves, Climate Change and Variability and Extreme Events.

Scan this  
to access a digital  
copy from the  
national archive



DOI: 10.12681/eadd/54808